UNIVERSITÀ DEGLI STUDI DI PADOVA

Dipartimento di Tecnica e Gestione dei Sistemi Industriali

Corso di Laurea Magistrale in

Ingegneria dell’Innovazione del Prodotto

FATIGUE COMPRESSION OF UNIDIRECTIONAL CFRP $[(\pm45)]_{24}$ AND INFLUENCE OF THE UNIFORMITY OF THE STRESS FIELD

SUPERVISORS: Prof. Dr. ing. Marino Quaresimin (Padova University)

Prof. Dr. ir. Wim Van Paepegem (Gent University)

Dr. ir. Ruben D. B. Sevenois (Gent University)

STUDENT: Edoardo Zanguio

Student number: 1153981

Academic year: 2018 - 2019

Index

1 INTRODUCTION 1

2 LITERATURE STUDY 5

2.1 FAILURE OF UNIDIRECTIONAL COMPOSITES 5

2.1.1 STATIC BEHAVIOUR 5

2.1.1.1 Microscopical mechanisms behind static failure of unidirectional composites 6

2.1.1.2 Macroscopical properties of static behaviour of unidirectional composites 11

2.1.2 FATIGUE BEHAVIOUR 15

2.1.2.1 Microscopical mechanisms behind static failure of unidirectional composites 15

2.1.2.2 Macroscopical properties of static behaviour of unidirectional composites 17

2.2 FATIGUE TESTING ON COMPOSITE MATERIAL 21

2.2.1 INTRODUCTION 21

2.2.2 STRESS – LIFE CURVES (S – N) 23

2.2.3 COMPRESSION TEST METHODS 25

2.2.3.1 Shear Loaded Compression Test Method - ASTM D 3410 27

2.2.3.2 End Loaded Specimen - ASTM D 695 MODIFIED 33

2.2.3.3 Sandwich-Beam Specimen Test Methods – ASTM D 5467 36

2.2.3.4 Combined loading compression test method – ASTM D 6641 39

2.2.3.5 Summary of the test methods 42

3 PREVIOUS WORKS 45

3.1 “C-C and T-C fatigue of woven carbon epoxy composites” S. Walraet [29].... 45

3.1.1 Objectives 45

3.1.2 Set-up configuration 46

3.1.2.1 DIC cameras 48

3.1.2.2 Measurement system evaluation 50

3.1.3 Material and specimen design 51

3.1.3.1 Material 51

3.1.3.2 Specimen geometry 52

3.1.3.3 Dimensions 53

3.1.3.4 End tabs 54

3.1.3.5 Final design 55

3.1.4 Test results 56

3.1.4.1 Quasi-static tests 56

3.1.4.2 Fatigue tests 57

3.1.5 Issues encountered 60

3.1.6 Improvements to apply to further works 61

3.2 “The effect of partially debonded tabs on the compressive stress-strain curve of angle-ply laminates” Pablo H. Jimenez [30] 62

3.2.1 Objectives 62

3.2.2 Set-up configuration 62

3.2.2.1 DIC cameras 62

3.2.2.2 Measurement system evaluation 63

3.2.2.3 Post-processing and calculations software 63

3.2.3 Material and specimen design 63

3.2.3.1 Material 63

3.2.3.2 Specimen geometry 64
3.2.3.3 Dimensions 64
3.2.3.4 End tabs 65
3.2.3.5 Final design 65
3.2.4 Test results 66
3.2.5 Issues encountered 70
3.2.6 Improvements to apply to further works 71
4 EXPERIMENTAL SET-UP 74
4.1 Measurement System set-up 74
4.1.1 Machine 74
4.1.2 DIC cameras 75
4.1.3 Temperature 77
4.1.4 Microscope 78
4.1.5 Measurement system 79
4.1.5.1 Static test mode 80
4.1.5.2 Fatigue test mode 81
4.2 Material and specimen design 83
4.2.1 Material 83
4.2.2 Specimen geometry and dimensions 83
4.2.3 End tabs 84
4.2.4 Specimen manufacturing 85
4.3 Digital Image Correlation 89
4.3.1 How it works 90
4.3.1 Specimen preparation 91

4.3.2 Cameras and lights positioning - calibration 92

4.3.3 Images sorting and post-processing 93

4.3.4 Rigid body motion 95

4.3.4.1 Static 96

4.3.4.2 Sinewave 98

5 TEST RESULTS 100

5.1 Static Tests 100

5.1.1 Stress-Strain curves 100

5.1.2 Maximum compressive stress 103

5.1.3 Strain field comparison 104

5.1.4 Stiffness 106

5.2 Fatigue Tests 110

5.2.1 Test program 110

5.2.2 Temperature evolution 112

5.2.3 S-N curve – Wöhler curve 113

5.2.4 Strain evolution 114

5.2.5 Permanent strain evolution 117

5.2.6 Stiffness evolution 119

5.2.6.1 Load conditions: 60% of the maximum stress and 3 Hz of frequency 121

5.2.6.2 Load conditions: 65% of the maximum stress and 3 Hz of frequency 122

5.2.6.3 Load conditions: 70% of the maximum stress and 1 Hz of frequency 123

5.2.6.4 Load conditions: 80% of the maximum stress and 1 Hz of frequency 124
5.2.6.5 Stiffness comparison 125
5.3 Damage analysis........ 127
5.3.1 Number of cracks........ 127
5.3.1.1 B type crack density evolution 129
5.3.1.2 D type crack density evolution........ 134
5.3.2 Free length........ 137
5.3.2.1 B type free length evolution 137
5.3.2.2 D type free length evolution 140
6 CONCLUSIONS 143
6.1 Conclusions 143
6.2 Recommendations for further work........ 146
7 APPENDIX........ 149
7.1 Macros 149
7.1.1 Strain Evolution, Stress-Strain curves, Permanent strain 149
7.1.2 Stiffness evolution 150
8 BIBLIOGRAPHY........ 153

LIST OF FIGURES:

Figure 1.1: Global demand for CFRP in tonnes 2008-2020 [28] 2

Figure 2.1: Tensile load on a cross-ply layup [22] 6

Figure 2.2: Compression failure modes [1] – (a) Elastic microbuckling – (b) Plastic microbuckling – (c) Fiber crushing – (d) Splitting of the matrix – (e) Buckle delaminations – (f) Shear band formation 8

Figure 2.3: Elastic microbuckling [3] 9

Figure 2.4: Orthotropic FRP lamina 11

Figure 2.5: Carbon-epoxy properties function of load angle [48] 12

Figure 2.6: Static behaviour of FRP composite laminate 13

Figure 2.7: Damage measurement, permanent strain and stiffness loss [35] 14

Figure 2.8: Sketched fatigue damage accumulation [32] 16

Figure 2.9: Damage modes during fatigue life 17

Figure 2.10: Degradation of composite strength and stiffness during constant amplitude fatigue loading [35] 18

Figure 2.11: Representative hysteresis behaviour for laminate $[\#(+45/-45)]_{24}$ with stress ratio R = 10 at two stress levels [36] 19

Figure 2.12: Representative hysteresis behaviour for laminate $[\#(+45/-45)]_{24}$ with stress ratio R = −1 at two stress levels [36] 20

Figure 2.13: Example sinusoidal constant amplitude load waveforms showing definition of terms and illustration of R-values [41] 23

Figure 2.14: S-N curve for the case of $[\#(\pm 45)]_{24}$ with R =10 [29] 24

Figure 2.15: Load introduction methods for compression tests [38] 27

Figure 2.16: Compression test specimen drawing on ASTM D3410 [45] 28

Figure 2.17: Failure identification codes and overall specimen failure schematics [45] 30

Figure 2.18: Celanese compression test fixture 31

Figure 2.19 Schema of IITRI test method [39] [44] 32

Figure 2.20: Diagrammatic comparison of Celanese (a) and IITRI (b) clamps [38] 33

Figure 2.21: Specimen configurations for ASTM D 695 (left) and modified ASTM D 695 (right) [38] 34

Figure 2.22: Disassembled compression jigs with specimens mounted for ASTM D 695 modified 35

Figure 2.23: ASTM D 5467 Test Fixture 36

Figure 2.24: ASTM D 5467 – Longitudinal compression sandwich beam test specimen 37

Figure 2.25: ASTM D 5467 – Sandwich beam test specimen failure identification codes and overall specimen failure schematics [49] 38

Figure 2.26: Dimensioned sketch of a CLC test fixture [50] 40

Figure 2.27: A photograph of a typical CLC test fixture [50] 40

Figure 2.28: Typical ASTM D 6641 Test specimen configuration [50] 41

Figure 3.1: LabView triggered system [29] 48

Figure 3.2: Camera set-up for 3D DIC [29] 49

Figure 3.3: Camera concept capturing two 2D images of a specimen rather than a single frontal 3D image [29] 50

Figure 3.4: Rigid body motion of 1mm at 1Hz shots at different fps shows delay between signals 51

Figure 3.5: Material data sheet from manufacturer [29] 52

Figure 3.6: Final specimen dimensions [29] 55

Figure 3.7: Stress-strain behaviour for static tests [29] 56

Figure 3.8: S-N curves for $[\#(0/90)]_{24}$ with R=10 above left, $[\#(0/90)]_{24}$ with R=-1 above right, $[\#(+-45)]_{24}$ with R=10 below left, $[\#(+-45)]_{24}$ with R=-1 below right [29] 57

Figure 3.9: $[\#(0/90)]_{24}$ R = 10, Stiffness evolution on the left and stress-strain behaviour on the right [29]... 58

Figure 3.10: $[\#(0/90)]_{24}$ R = -1, Stiffness evolution on the left and stress-strain behaviour on the right [29]... 58

Figure 3.11: Stiffness evolution $[\#(\pm45)]_{24}$ R = 10 on the left and stress-strain behaviour on the right [29]... 59

Figure 3.12: Stiffness evolution $[\#(\pm45)]_{24}$ R = -1 on the left and stress-strain behaviour on the right [29]... 60

Figure 3.13: data points in case of $[\#(\pm45)]_{24}$ loaded under C-C (R = 10). Frequencies of 2 and 3 Hz for this configuration will be avoided due to specimen overheating [29]...... 61

Figure 3.14: Final design and dimensions of B and D type specimens. Dimensions of tabs and coupon are not drawn to scale [30] 66

Figure 3.15: ε_{xx} Strain field comparison between B (below) and D (above) type specimen analysed on Abaqus [30] 66

Figure 3.16: $\boldsymbol{\varepsilon_{XX}}$ Strain field comparison between D (left) and B (right) type specimen obtained at 30 MPa with Vic3D software [30] 67

Figure 3.17: Stress-Strain curves comparison for B and D type specimens [30] 68

Figure 3.18: Maximum compressive stress comparison between B and D type [30] ... 68

Figure 3.19: Stiffness comparison evaluated from static tests [30] 69

Figure 3.20: Manufacturing issues with waterjet cutting [30]...................................... 70

Figure 3.21: Paint detachment issue [30] 71

Figure 3.22: Overview of the new coupon’s manufacturing technique [30]................. 72

Figure 3.23: Paint comparison between three specimens [30] 73

Figure 3.24: Different speckle pattern between the old painting and the new airbrush base paint (left and right) [30] 73

Figure 4.1: an Instron 8801 (100kN) servohydraulic fatigue testing system 75

Figure 4.2: Point Grey Grasshopper USB 3.0 cameras (GS3-U3-51S5M-C) 76

Figure 4.3: Thermocouple positioning 77

Figure 4.4: Keyence VHX-2000 digital microscope 78

Figure 4.5: Labview triggered system [30] 79

Figure 4.6: Real system set-up configuration 80

Figure 4.7: LabView static mode interface 81

Figure 4.8: LabView fatigue mode interface 82

Figure 4.9: Fully bonded (B) and partially debonded (D) design comparison [30] 84

Figure 4.10: Nesting drawing of the plate 85

Figure 4.11: Drawing of tabs pattern (Solidworks©) 86

Figure 4.12: Printed tabs pattern 86

Figure 4.13: Plate preparation after the curing time 87

Figure 4.14: Final result of the manufacturing process 88

Figure 4.15: Extensometry with DIC [53] 91

Figure 4.16: Speckle pattern painted on the sample 92

Figure 4.17: Schematisation of the calibration parameters to be determined 93

Figure 4.18: Vic-3D© analysing the Region of Interest defined by the user 94

Figure 4.19: Display of results on Vic-3D© 95

Figure 4.20: Displacement comparison from a static rigid body motion with an error of 1,58% 96

Figure 4.21: Calibration speckle measurement under the microscope 97

Figure 4.22: Displacement comparison from a static rigid body motion with an error of 0,11% 97

Figure 4.23: Displacement comparison from a sinewave rigid body motion with a delay between the signals 98

Figure 4.24: Displacement comparison from a sinewave rigid body motion without delay between the signals 99

Figure 5.1: Region of interest correlated and virtually DIC extensometers location: vertical extensometer represents longitudinal strain, horizontal extensometer represents transversal strain 101

Figure 5.2: Stress-Strain curves from static tests 102

Figure 5.3: Stress-Strain curves from P. H. Jimenez [30] 102

Figure 5.4: Maximum compressive stress calculation 103

Figure 5.5: Maximum compressive stress calculated from static tests 104

Figure 5.6: Longitudinal strain field (ε_{xx}) comparison during a static test, at the same scale (ε absolute value) 105

Figure 5.7: Stiffness evaluated from static tests according to ASTM D 3410 107

Figure 5.8: Normal clamps distance (35mm) on the right and error distance between the clamps on the “B12” on the left 108

Figure 5.9: Temperature behaviour comparison between the two types of samples under the same load conditions (65% of the maximum load and 3 Hz) 113

Figure 5.10: Wöhler curve for unidirectional carbon-epoxy $[+45/-45]_{6S}$ R=10, the results obtained from B and D type samples are plotted, logarithmic trendlines are plotted 114

Figure 5.11: Stress-Strain behaviour for B type, load condition: 65% of the maximum load and 3Hz frequency 115

Figure 5.12: Stress-Strain behaviour for D type, load condition: 65% of the maximum load and 3Hz frequency 116

Figure 5.13: Definition of permanent stress 118

Figure 5.14: Permanent strain evolution for all the stress levels 118

Figure 5.15: Definition of stiffness from Stress-Strain curves.................................... 120

Figure 5.16: Stiffness evolution comparison: load conditions: 60% of the maximum stress and 3 Hz of frequency 121

Figure 5.17: Stiffness evolution comparison: load conditions: 65% of the maximum stress and 3 Hz of frequency.. 122

Figure 5.18: Stiffness evolution comparison: load conditions: 70% of the maximum stress and 1 Hz of frequency 123

Figure 5.19: Stiffness evolution comparison: load conditions: 80% of the maximum stress and 1 Hz of frequency.. 124

Figure 5.20: Stiffness evolution comparison for B type and different load conditions125

Figure 5.21: Stiffness evolution comparison for D type and different load conditions126

Figure 5.22: Division of the side zones of the sample.. 128

Figure 5.23: Outer layer fails at 5000 cycles for B23 sample 129

Figure 5.24: Cracks at 7000 cycles for “B23” sample 130

Figure 5.25: Cracks at 10000 cycles for “B23” sample 131

Figure 5.26: Cracks at 10000 cycles for “B23” sample at a lower magnification......... 131

Figure 5.27: Microscope image at the failure of “B23” sample (11207 cycles)........... 132

Figure 5.28: Stiffness evolution and number of cracks for “B23”............................... 133

Figure 5.29: Cracks at 13000 cycles for “D16” sample... 135

Figure 5.30: Cracks at 13000 cycles for “D16” sample at a lower magnification 135

Figure 5.31: Stiffness evolution and number of cracks for “D16” 136

Figure 5.32: Tabs debonding at 1000 cycles for “B23” 138

Figure 5.33: Tabs debonding at 3000 cycles for “B23” 138

Figure 5.34: Tabs debonding surface after failure of “B23” specimen 139

Figure 5.35: Stiffness evolution and free length for “B23” 140

Figure 5.36: Tabs debonding surface after failure of “D16” specimen 141

LIST OF TABLES:

Table 1: Compression tests methods comparison 43

Table 2: Fatigue test program for B type 111

Table 3: Fatigue test program of D type 111

Table 4: Damage analysis measurements intervals 128

Table 5: Cracks and delaminations measurements for B23 (load conditions: 70% of the maximum stress and 1Hz) 129

Table 6: Cracks and delaminations measurements for D16 (load conditions: 70% of the maximum stress and 1Hz) 134

Table 7: Cracks, delaminations and free length measurements for B23 (load conditions: 70% of the maximum stress and 1Hz) 137

Table 8: Cracks, delaminations and free length measurements for D16 (load conditions: 70% of the maximum stress and 1Hz) 140

1 INTRODUCTION

Many materials, also in nature, are effectively composites. This is particularly true for natural biological materials, which are often made of at least two constituents. Examples are: wood, made from long cellulose fibres held together by a much weaker substance called lignin, and human bones, made from a hard but brittle material called hydroxyapatite and a soft and flexible material called collagen. In many cases, a strong and stiff component is present, often in elongated form, embedded in a softer constituent forming the matrix. Commonly, such composite materials show anisotropic behaviour. This usually arises because the stiffer constituent has a fibrous form, which is very stiff in the primary direction but not in the transverse fibre direction. Learning from nature, in making artificial composite materials, this potential for controlled anisotropy offers considerable scope for integration between the processes of material specification and component design.

"The essence of composite materials technology is the ability to put strong stiff fibres in right place, in the right orientation with the right volume fraction. "D. Hull T. W. Clyne *An introduction to composite materials*, Cambridge University Press, 1996

There are several different types of composites. Fiber-reinforced polymer matrix composites are the most widely used fiber composites. The large usage [28] of polymer composites can be attributed to the following outstanding properties:

- Mechanical properties (high strength and stiffness)
- Light weight
- Corrosion resistance
- Flexibility in design
- High fatigue resistance
- Properties can be tailored

Very high specific stiffness of carbon-fiber-reinforced polymers (CFRP) has been an important consideration in the use of CFRPs in aerospace application, automotive, construction and transportation in general. Global demand (and estimated demand) of CFRPs is shown in **Figure 1.1**.

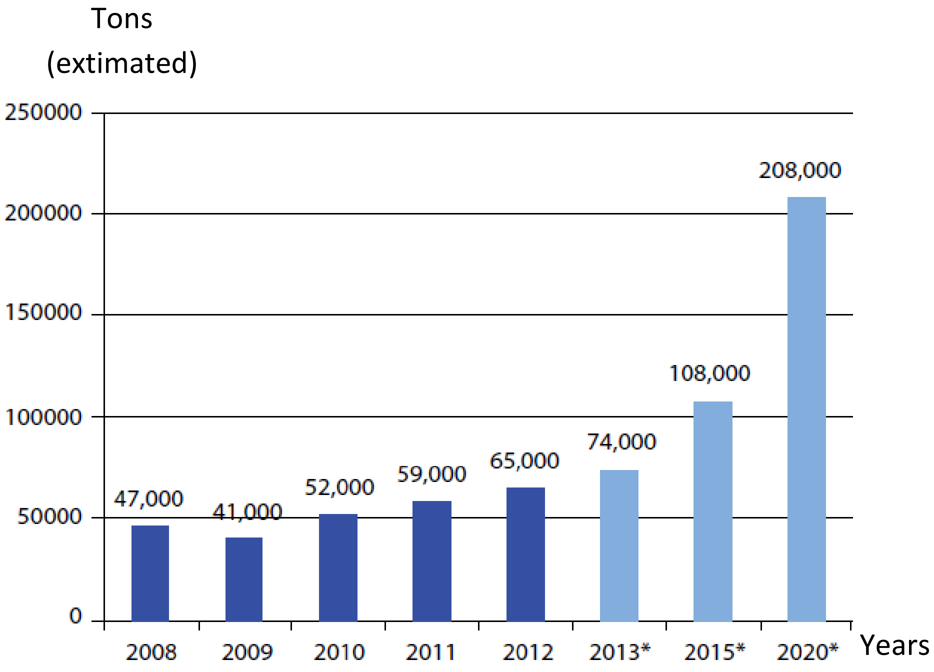

Figure 1.1*: Global demand for CFRP in tonnes 2008-2020 [28]*

In general, fatigue of fibre-reinforced composite materials is a quite complex phenomenon, and a large research effort is being spent on it today. Fibre-reinforced composites have a rather good rating with regards to life time in fatigue. This, however, does not apply to the number of cycles to initial damage nor to the evolution of damage. Composite materials are inhomogeneous and anisotropic, and their behaviour is more complicated than that of homogeneous and isotropic materials such as metals.

The CFRPs data related to fatigue are largely involved in S-N curves, other variables like stiffness evolution, cracks initiation and propagation, delaminations behaviour and permanent strain evolution are not commonly investigated. Additionally, most literature focuses on tension-tension (T-T) fatigue cyclic loading. The behaviour of CFRPs with respect to tension-compression (T-C) and compression-compression (C-C) cyclic loading is not frequently investigated due to the experimental difficulties associated with it.

A large part of the literature on compressive failure of composites is devoted to the problem of determining what type of test configuration is best. In order to test the strength of the material, the test fixture should result in a uniaxial state of stress, and the specimen should be sized to prevent global buckling of the structure. For long specimens, the bending stress caused by column buckling translates into a decrease in the applied load necessary for failure, while very short specimens suffer more from interaction between the stress concentrations at the grips. It is also important that specimens fail in a consistent manner in the region away from stress concentrations caused by the grips. In order to avoid buckling and achieve a uniform stress field, some of the questions addressed are specimen size and shape, loading arrangement, compressive end loading versus shear loading, lateral constraints to prevent buckling, stress concentrations from holes or grips, nonuniform stress distributions, and effects of end tabs.

Several testing methods have been standardized, by the American Society for Testing and Materials (ASTM) but there is still considerable research aimed at improving test methodology, and it is still common for nonstandard methods to be employed for reasons of cost or for special geometries or environments. [23]

This work is a prolongation of the previous works of S. Walraet [30] and P. H. Jimenez [31]. Walraet studied the fatigue behaviour of angle-ply woven CFRP under T-C and C-C cyclic loads with unsupported short gauge length samples. Numerous problems such as buckling, temperature of the specimens and tab debonding were found. A particular issue is that the sample size, in order to avoid buckling in compression, needed to be thus short that, for the angle-ply laminates, a non-uniform stress state existed in the gauge length. At the same time tab debonding occurred during cycling which altered the boundary conditions on the gauge length and resulted in an apparent stiffness increase of the samples. P. H. Jimenez's work continued to resolve the issue of a non-uniform stress field by introducing partly debonded tabs. In this way a partly supported short gauge length compression sample with a uniform stress state was created. For static compression tests, this proved to be successful.

The purpose of this master thesis work is to investigate whether the static compression sample design by P.H. Jimenez, with partly debonded tabs, can be used for C-C fatigue loading as well. To this end, this specimen design will assure a uniform stress field on the center of the gauge section while buckling is prevented. In order to prove this new specimen design, the stiffness evolution has to be observed, and it has to decrease during the fatigue test. Results obtained by debonded specimens will be compared with the results from the non-debonded samples. The main objective is to analyse the different fatigue behaviour and compare with the results from S. Walraet obtained on angle ply woven carbon epoxy. Thanks to this, two different material's architecture such as woven and unidirectional angle ply CFRPs can be compared to better understand the different fatigue behaviour.

It has to be mentioned that during a fatigue test, heating of the specimen can occur, due to the hysteresis induced on the material. The friction between the partially debonded tabs and the composite needs to be taken into account as a probable problem during a fatigue test.

In the following section, first literature will be investigated for experimental setups for compression testing of composite materials. Then, in section 3 the previous work by S. Walraet and P.H. Jimenez will briefly be introduced, analysing the problems encountered. From section 2 and 3 the objectives of this thesis are defined together with a detailed plan of action. Section 4 contains the experimental setup, section 5 the results of the static and fatigue tests, section 6 analysis of the results and section 7 the conclusions.

2 LITERATURE STUDY

The purpose of this literature study is to identify, examine and evaluate the literature for the experimental tests of unidirectional CFRPs loaded in C-C fatigue.

The chapter is divided into two main sections. In section 2.1, "Failure of UD composites", the various mechanisms responsible for composite failure under static and fatigue loading are discussed. In section 2.2, "Fatigue testing of composite", the existing methods for static and fatigue compression testing of composite materials are explained.

2.1 FAILURE OF UNIDIRECTIONAL COMPOSITES

This section presents results from a literature study of the failure modes and the mechanical properties of unidirectional composites materials under static and cyclic loads.

2.1.1 STATIC BEHAVIOUR

The resistance of composites materials to static loading depends on the properties of the constituents. As an effect of the anisotropy of the composites, the strength varies in function of the load direction. While metal static failure is usually controlled by a single propagating crack, the microscopic structure of composite results in a more general damage accumulation, generated by several different processes.

2.1.1.1 Microscopical mechanisms behind static failure of unidirectional composites

On the microscale, the occurrence, propagation, and accumulation of microscopical failure mechanisms lead to different failure modes. Which type of mechanisms occur depends on the direction of the load applied to the structure:

Tensile

When composites are loaded in tension, the principal failure modes are fibre breakage, matrix cracking, fiber-matrix interphase failure and delaminations. Matrix cracks occur in plies perpendicular to the applied load and usually occur at the beginning of the loading. As the load and the stress increases, the fibre starts to be damaged and the interphase between fibers and matrix start to debond. Continuing to increase the load, the fibers cannot sustain the load applied and result in complete failure. In **Figure 2.1** below is shown a representation of the damage in a cross-ply FRP under tensile load.

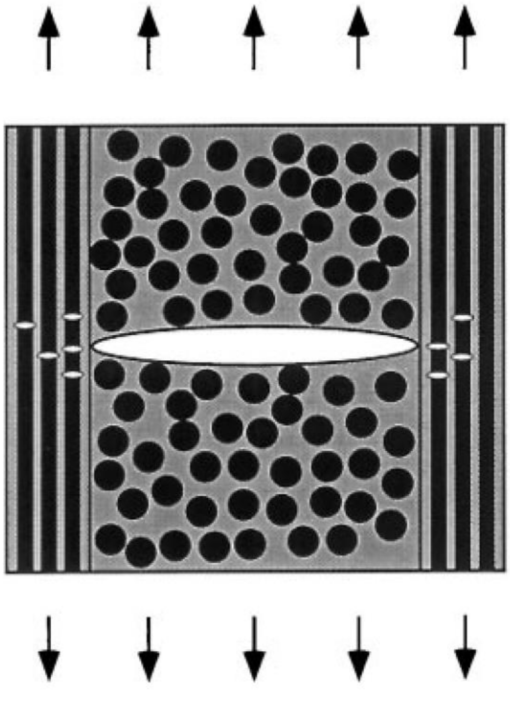

Figure 2.1: *Tensile load on a cross-ply layup [22]*

Compressive

Compression failure is a design limiting feature of aligned, continuous fibre composite materials. For example, the compressive strengths of unidirectional carbon fibre epoxy laminates are often less than 60% of their tensile strengths.

To better understand the compressive static behaviour, it’s necessary to investigate, looking at the microscale, on how fibers, matrix and interphase fails.

Fibers fail differently, depending on their internal structure. Both shear failure and kinking are characteristic fiber failure modes for well-aligned fibrillar structures. The basic mechanisms for the two failure modes seem to be the same, however strongly depend upon the lateral support provided the fiber during loading. In the absence of a strong lateral support, all fibers would fail by buckling. As the support stiffness increases, buckling is suppressed and the fiber starts to fail in shear.

Compression tests on bulk **resins** reveal two types of failure. For ductile resins, plastic flow is frequently observed in a broad band oriented -45 degrees to the loading axis. For brittle resins, however, shear banding, i.e., narrow zones of shear yielding, can precede ultimate failure.

Because of the weakness of the matrix and the **fiber/matrix interface** compared with the strength of the fibers, unidirectional composites can fracture along the fibers even when loaded in compression.

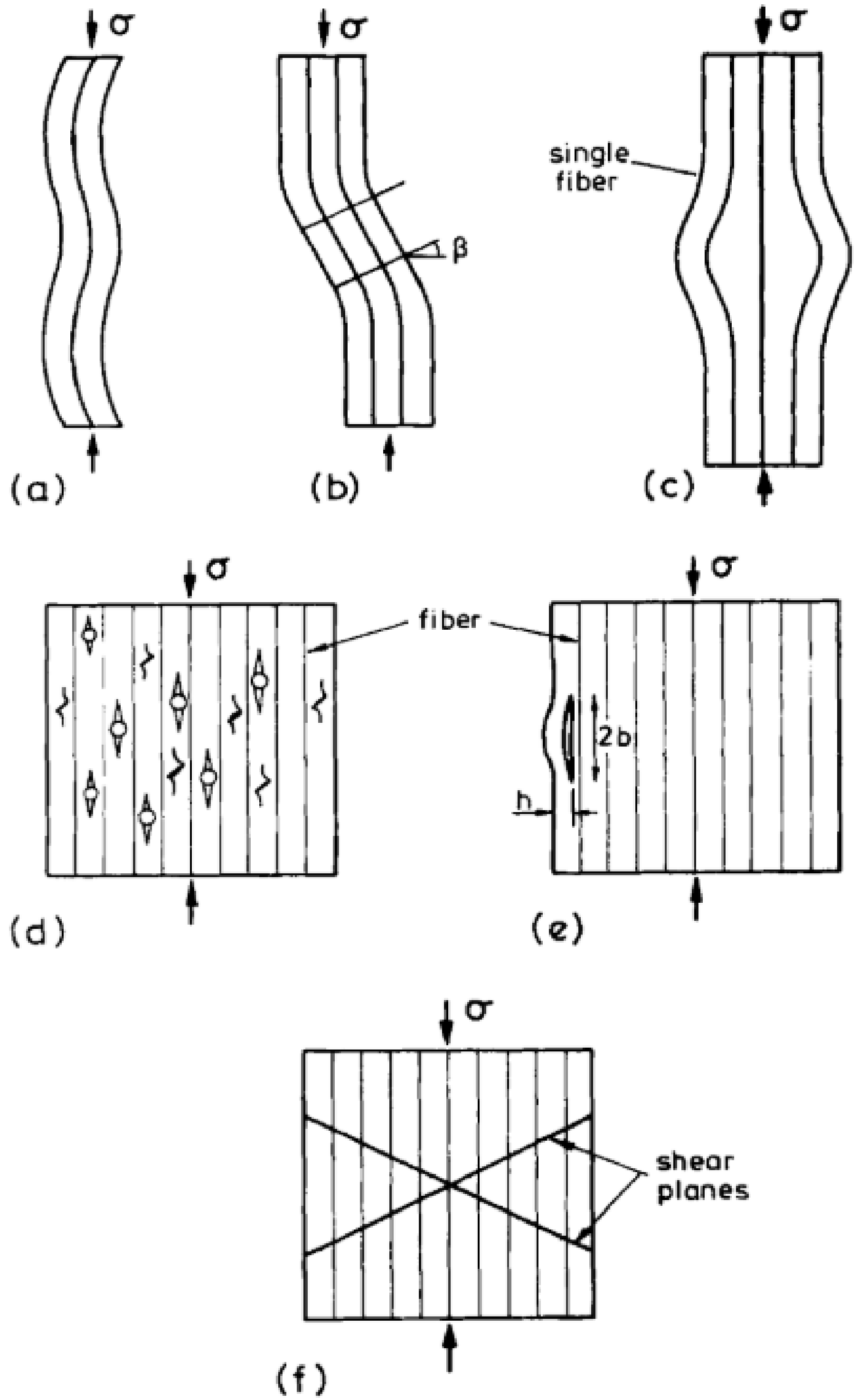

***Figure 2.2**: Compression failure modes [1] – (a) Elastic microbuckling – (b) Plastic microbuckling – (c) Fiber crushing – (d) Splitting of the matrix – (e) Buckle delaminations – (f) Shear band formation*

Failure modes are a combination of different mechanism behind the failure of matrix, fibers and interphase. As reported by Fleck [1] in **Figure 2.2**, six failure modes for compression loading can be identified:

- **Elastic microbuckling** has been the most widely studied failure mode for composites made of strong fibers and matrices. For high volume fraction composites, microbuckling is expected to be controlled by the matrix stiffness in shear, and thus strongly affected by time, history, strain rate and environment. In addition, like other buckling problems, microbuckling depends on the initial imperfections of the composite which result from manufacturing process associated defects, such as fiber misalignment or waviness, residual stresses and porosity.

- **Kinking** or **plastic microbuckling** in polymer composites**,** shown in **Figure 2.3**, is a direct consequence of localized plastic microbuckling coupled with the low failure strain of the reinforcing material. When these deformations are large enough, the surrounding matrix will undergo plastic deformation and kinking occurs. Kinking failure involves significant plastic deformation of the matrix, as

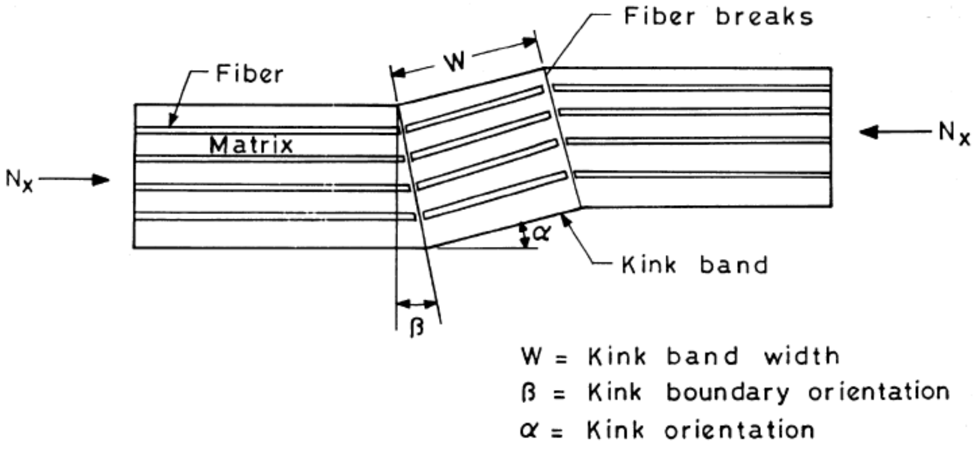

***Figure 2.3**: Elastic microbuckling [3]*

well as highly loaded fibers on the outside of the kink bands, often resulting in fiber breakage.

- **Matrix splitting** appears as longitudinal matrix cracks parallel to the fibers (and load).

- **Fiber crushing** failure occurs at the fiber level due to a shear instability such as buckling within the fiber. It is often associated with the fact that the fibers themselves are microcomposites comprising wavy fibers embedded in a soft matrix. For strong fibers, like glass or carbon fibers, this failure mode rarely manifests itself.

- **Buckle delamination**: splitting in a direction parallel to the main load direction is encouraged when a surface layer is debonded over a finite length.

- **Shear band formation:** can occur in composites with low fiber volume fraction. Matrix yield and fracture reveal in a band, oriented at about 45° with respect to the loading axis**.**

2.1.1.2 Macroscopical properties of static behaviour of unidirectional composites

The problem of determining the macroscopic or effective physical properties of composite media is a classical one in science and engineering, attracting the attention of such luminaries as Maxwell (1873) and Einstein (1906). In the most general sense, a heterogeneous material consists of domains of different materials (phases) or the same material in different states. [26]

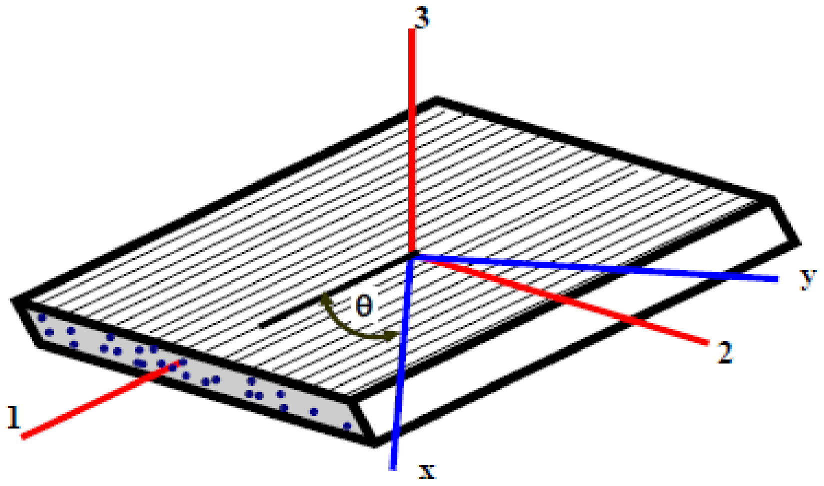

***Figure 2.4**: Orthotropic FRP lamina*

Fiber reinforced composites are usually manufactured to a laminate with long fibers placed parallel to one-another, kept together by the matrix, as shown in **Figure 2.4** above.

In case of a single unidirectional fiber reinforced composite ply, it is possible to identify two orthogonal symmetric planes. This implicates symmetry with the third plane and the ply can be defined transversely orthotropic.

The stiffness matrix obtainable from Hooke generalized law has nine independent constants and it is shown in **Equation 2.1**.

$$\begin{Bmatrix} \sigma_1 \\ \sigma_2 \\ \sigma_3 \\ \sigma_4 \\ \sigma_5 \\ \sigma_6 \end{Bmatrix} = \begin{bmatrix} C_{11} & C_{12} & C_{13} & 0 & 0 & 0 \\ . & C_{22} & C_{23} & 0 & 0 & 0 \\ . & . & C_{33} & 0 & 0 & 0 \\ . & . & . & C_{44} & 0 & 0 \\ . & SYM & . & . & C_{55} & 0 \\ . & . & . & . & . & C_{66} \end{bmatrix} \begin{Bmatrix} \varepsilon_1 \\ \varepsilon_2 \\ \varepsilon_3 \\ \varepsilon_4 \\ \varepsilon_5 \\ \varepsilon_6 \end{Bmatrix}$$

Equation 2.1

It is possible to estimate these constants using analytical methods like the rule of mixture or Halpin-Tsai or by experimental tests.

Each ply with fiber aligned in a preferred direction, have different properties as a function of the load inclination. The highest stiffness of the ply is reached when the load is aligned with the fiber direction. An example of a Carbon-Epoxy ply’s static behaviour along different load angle is shown in **Figure 2.5** below.

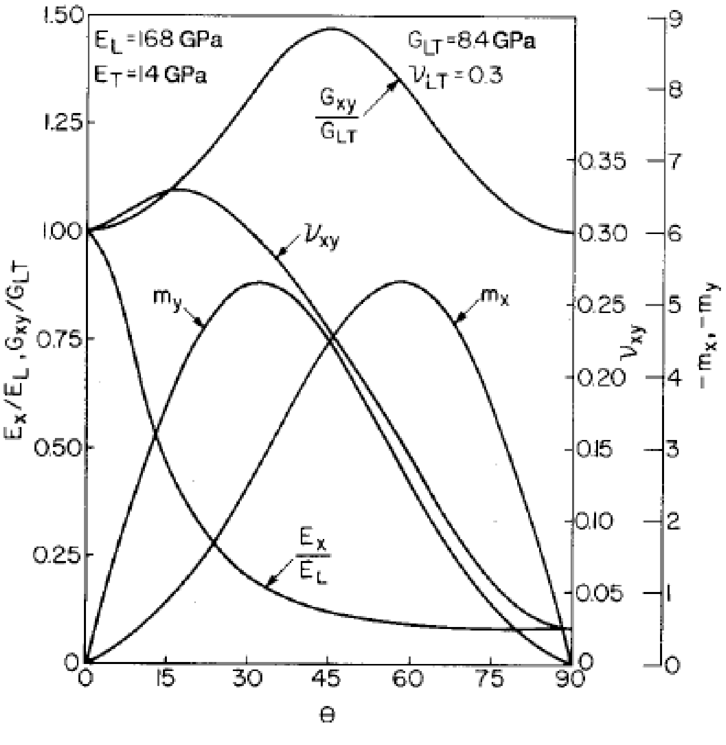

***Figure 2.5**: Carbon-epoxy properties function of load angle [48]*

A composite structure generally constitutes of several unidirectional orthotropic laminas with different fiber orientation, perfectly bonded between each other, that interact like a singular structural element.

Once the properties of a single lamina are estimated, the macroscopical properties of a laminate can be evaluated based on the orientation of the plies and the stacking sequence. The structural response of a laminate to the external loads is usually calculated using Classical Laminate Theory (CLT) (see [29]).

Once a model to predict laminate resistance is settled, it is possible to predict what will be the first ply to reach the failure. How the ply reaches the failure has to be investigated in microscale and it is described in the previous paragraph. The failure of a single ply does not necessarily lead to the failure of the laminate. The laminate overall strength will be reduced by the portion of the single ply that reaches the failure. It means that a composite laminate does not have a linear static behaviour like metals, but it is gradual in function of the ply that reaches the failure. A theoretical stress-strain curve can be schematized in **Figure 2.6** below.

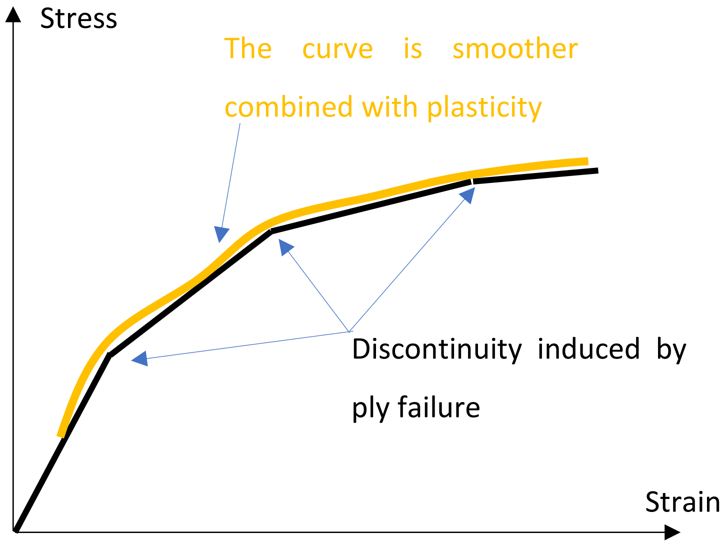

***Figure 2.6**: Static behaviour of FRP composite laminate*

The damage on FRP ply has non-linear behaviour, because it involves a lot of phenomena (explained before). It is possible to understand the evolution of the damage, analyzing some macroscopic mechanical properties like the permanent strain.

It has to be mentioned that during real experiments discontinuity are usually smoother due to the plasticity of the material. As shown in **Figure 2.6**, the real behaviour of the material is represented by the orange smoother curve.

The stiffness loss is revealed by elastic modulus variations on the experimental curves. Plasticity is revealed by the emergence of permanent strains, such that the instantaneous measured total strain is expressed by **Equation 2.2**:

$$\varepsilon_t{}^T = \varepsilon_t{}^e + \varepsilon_t{}^p$$

Equation 2.2

Where, $\varepsilon_t{}^T$ is the total strain, $\varepsilon_t{}^e$ is the elastic strain and $\varepsilon_t{}^p$ the permanent strain. It is necessary during the test to load and unload in order to measure $\varepsilon_t{}^e$ and $\varepsilon_t{}^p$. The number of cycles must not exceed five or six in order to stay in a domain where low-cycle fatigue phenomena are negligible.

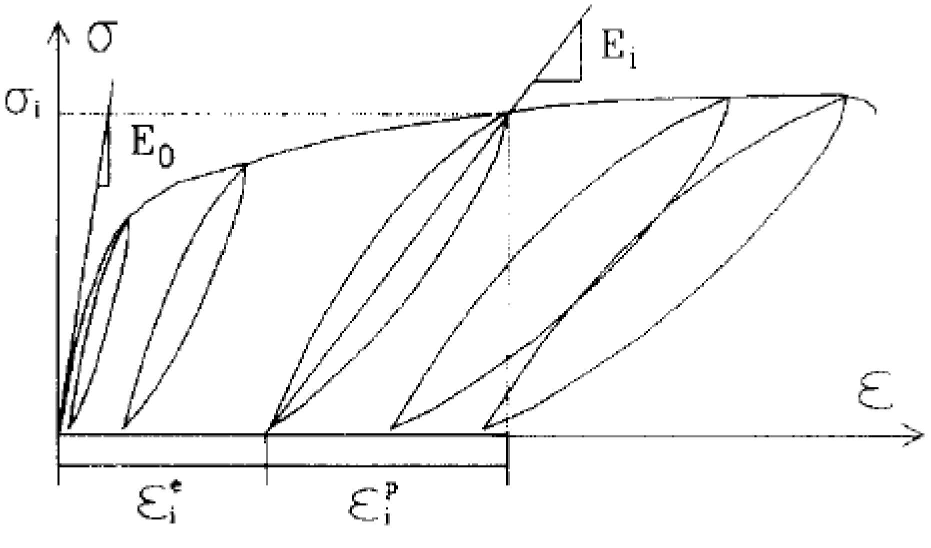

***Figure 2.7**: Damage measurement, permanent strain and stiffness loss [35]*

As shown in **Figure 2.7**, the permanent strain increases as the number of tests increases, meanwhile the stiffness decreases. The stiffness reduction is correlated with the damage of the material and it is not linear for FRPs.

2.1.2 FATIGUE BEHAVIOUR

Fatigue is the main failure mechanism for structures under cyclic loading. Considerable research has been carried out for monolithic materials such as metals and progress has been made in devising fatigue-resistant materials as well as in developing methodologies for life prediction. For composite materials, fatigue analysis and consequent life prediction become difficult because the material properties of the constituents of the composite are quite different. The fatigue behaviour of one constituent may be significantly affected by the presence of other constituents and the interfacial regions between the fibers and matrix. Fatigue properties of composites may vary significantly due to the large difference in the properties between the fibers and matrix of the composite and the composition of constituents [32].

To better understand the mechanisms involved during a fatigue load on a composite material, analysing the microscale gives an explanation about the fatigue behaviour.

2.1.2.1 Microscopical mechanisms behind static failure of unidirectional composites

Under cyclic loading, the damage will accumulate in composite materials and cause the fracture or functional failure of structures. For homogeneous, or monolithic materials with isotropic material properties, the damage is accumulated at a low growth rate in the beginning, as shown in **Figure 2.8**, and a single crack propagates in a direction perpendicular to the cyclic loading axis. On the other hand, in composite materials, especially for those structures with multiple plies and laminates, the fracture behaviour is characterized by multiple damage modes, such as crazing and cracking of the matrix, fiber/matrix decohesion, fiber fracture, ply cracking, delamination, void growth, and multidirectional cracking [32].

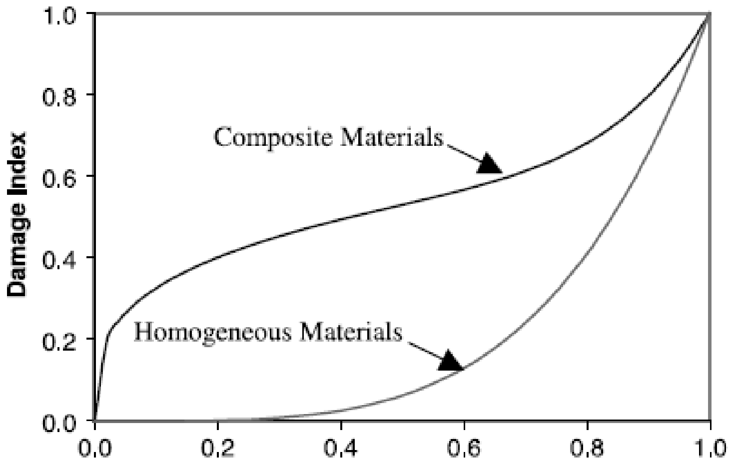

Figure 2.8: *Sketched fatigue damage accumulation [32]*

However, in a laminated composite, there are three principal failure modes: intra-ply cracking, interlaminar matrix delamination and fiber failure which play a role in affecting their mechanical properties. Amongst the three principal damage modes mentioned above, the interlaminar matrix delamination is of major importance. The delamination in a structure subjected to in-plane loads is a subcritical failure mode whose effect may be stiffness loss, local stress concentration, and a local instability causing its further growth leading to compressive failure. Delamination indirectly affects the final failure of the structure thus affecting its life. Therefore, delamination is known as the most prevalent life-limiting damage growth mode [33].

The mechanisms of crack initiation and crack growth are quite complex for composite materials. Even for unidirectional reinforced composites under a simple loading case such as tension along the direction of fibers, cracks can initiate at different locations and in different directions. Cracks can initiate in the matrix, perpendicular to the direction of loading. Cracks can also initiate in the interface along the directions of fibers between the fibers and matrix due to debonding [32].

During the initial period of fatigue life, many non-interactive cracks occur in the matrix. When the matrix crack density reaches saturation, the fiber failure, interfacial debonding and delamination occur in the composites. Damage will rapidly develop and the material causes ‘‘sudden death” in the end period of fatigue life, as shown in **Figure 2.9.** [34]

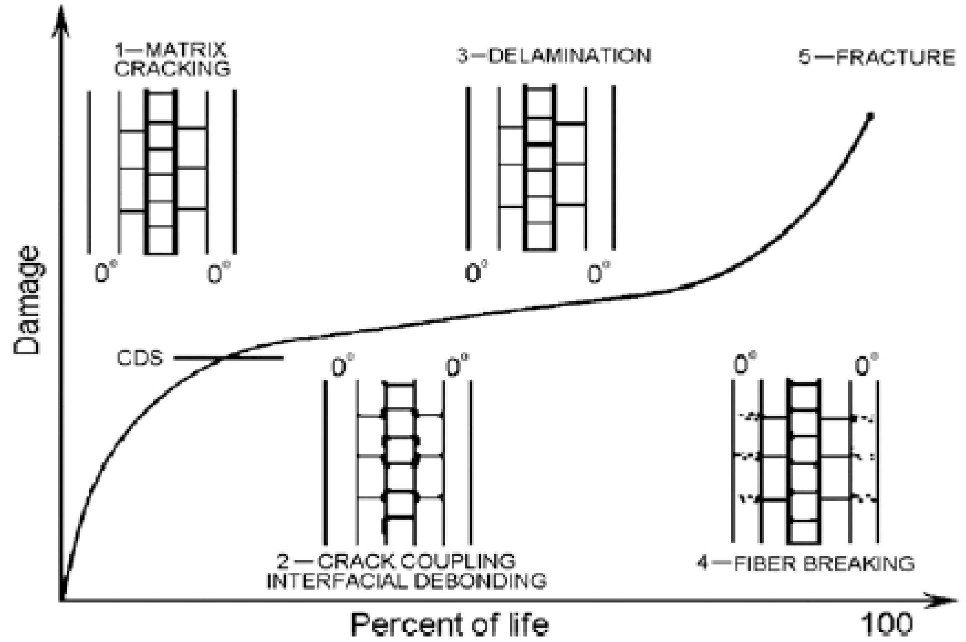

***Figure 2.9**: Damage modes during fatigue life*

2.1.2.2 Macroscopical properties of static behaviour of unidirectional composites

FRPs have a rather good rating with regard to lifetime in fatigue. The same does not apply to the number of cycles to initial damage nor to the evolution of damage. The main reasons for this are the different types of damage that can occur, their interactions and their different grows rates. As a consequence, the microstructural mechanisms of damage accumulation, of which there are several, occur sometimes independently. The predominance of one or another is strongly affected by both material variables and testing conditions.

In FRPs, damage starts very early and the extent of damage zones grows steadily, while the damage type in these zones can change. The gradual deterioration of FRP leads to a continuous redistribution of stress and a reduction of stress concentrations inside a structural component. As a consequence, an appraisal of the actual state or a prediction of the final state requires the simulation of the complete path of successive damage states. [16].

The degree of damage in a polymer matrix composite material can be followed by measuring the decrease of a relevant damage metric, usually the residual strength or residual stiffness. A theory based on the residual strength degradation assumes that damage is accumulated in the composite and failure occurs when the residual strength decreases to the maximum applied cyclic stress level, see **Figure 2.10**.

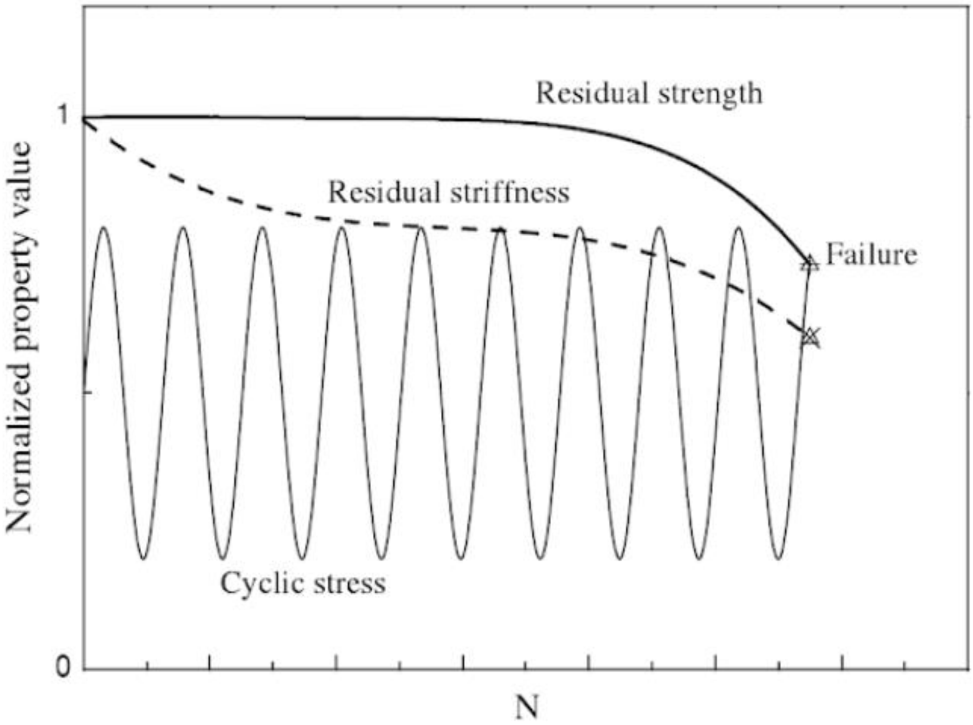

Figure 2.10*: Degradation of composite strength and stiffness during constant amplitude fatigue loading [35]*

Another phenomenon to keep into consideration during fatigue life is the permanent strain behaviour and the stiffness loss.

As reported in [36], with carbon epoxy woven angle ply $[\#(+45/-45)]_{24}$ during compressive load, a small amount of hysteresis is seen for the low load level accompanied by a 2% to 3% permanent shear strain deformation, **Figure 2.11** (a). For the high load level, the energy dissipated in the hysteresis loop is significant, **Figure 2.11** (b).

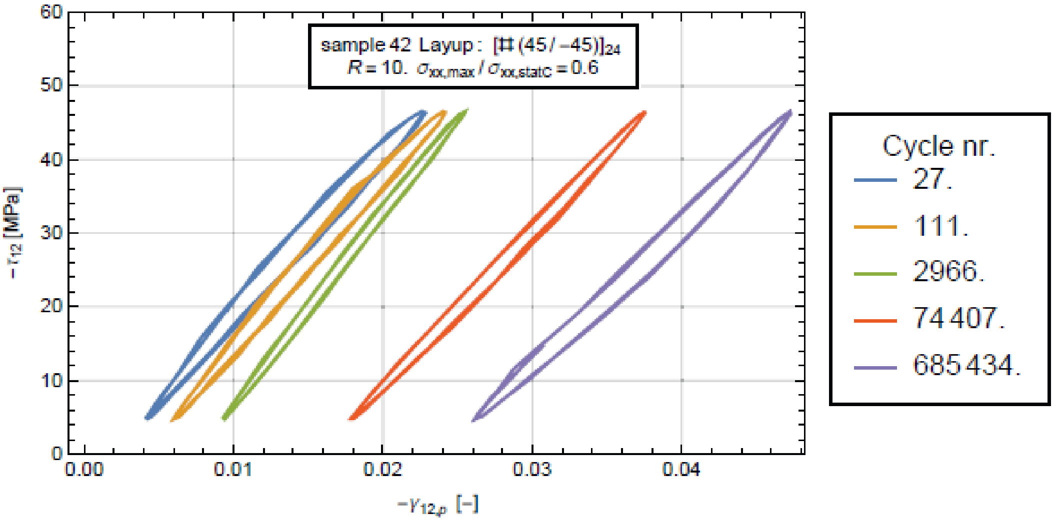

a. *Stress level 60%*

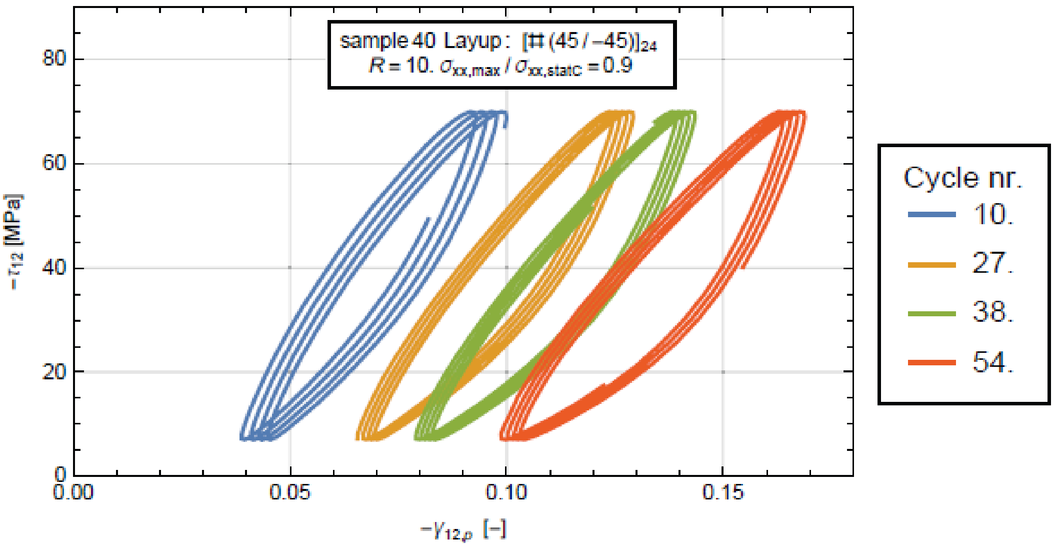

b. *Stress level 90%*

Figure 2.11*: Representative hysteresis behaviour for laminate $[\#(+45/-45)]_{24}$ with stress ratio R = 10 at two stress levels [36]*

Figure 2.12 shows the hysteresis behaviour for R = −1 for the laminate [#(+45/ − 45)]$_{24}$. As with the laminate for R = 10, clear hysteresis behaviour accompanied with significant energy dissipation is observed.

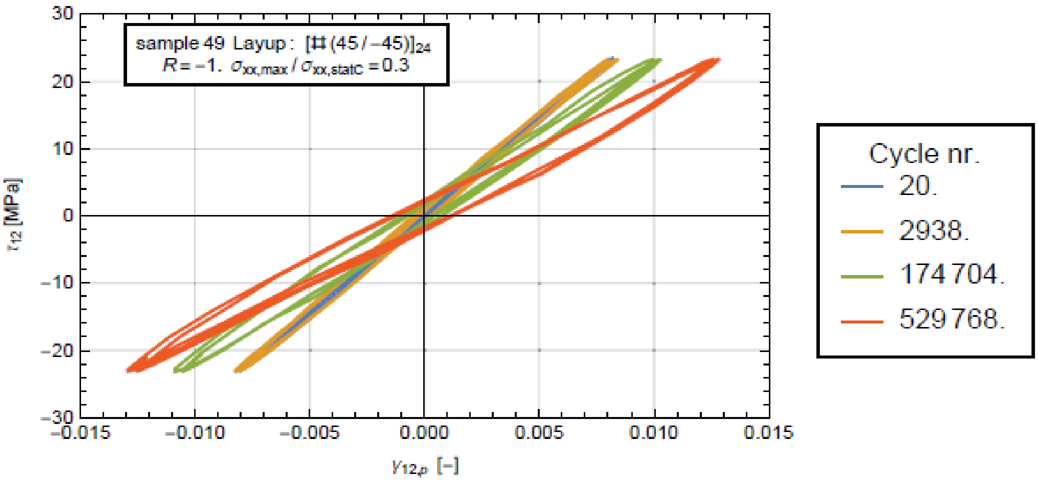

a. Stress level 30%

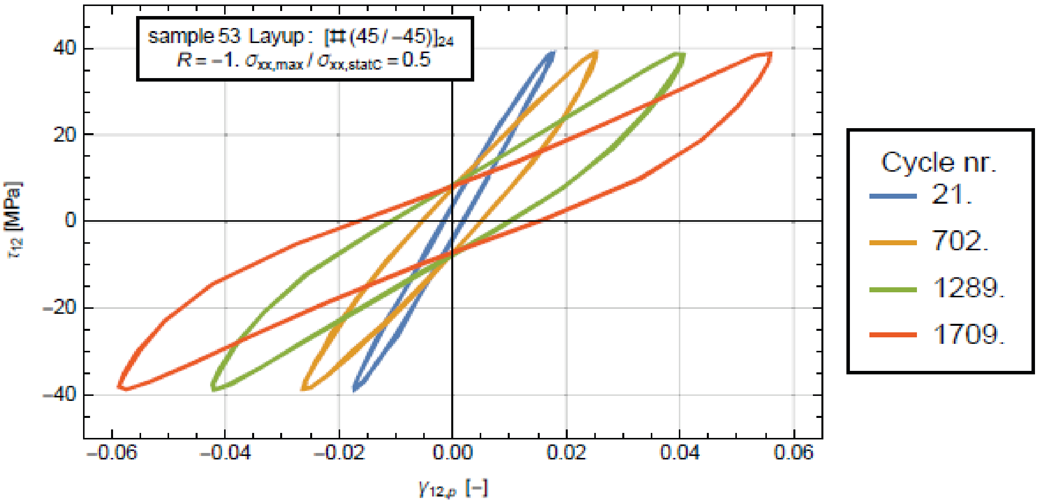

b. Stress level 50%

***Figure 2.12**: Representative hysteresis behaviour for laminate [#(+45/ − 45)]$_{24}$ with stress ratio R = −1 at two stress levels [36]*

2.2 FATIGUE TESTING ON COMPOSITE MATERIAL

2.2.1 INTRODUCTION

“Mechanical property data are essential in the design process if structures are to perform as intended – reliably and cost-effectively for their full life. However, there are no data without testing at some stage. But what tests should be carried out to give the required data? With which precision should the tests be conducted, and who says so? What does the data actually mean? How reliable are the data produced? Are data obtained from small test specimens meaningful when large structures are being designed? What effect will the operating environment have? Fortunately most, if not all of these questions have been answered in the case of isotropic solids, giving a starting point for the development of mechanical test methods for more complex materials such as advanced fibre composites.” [38]

“An extensive infrastructure of test methods and procedures has had to be developed to support the composites business, but the great variety of composite structures, the complexities of the properties, the diversity of service applications and the immediacy of particular commercial pressures have resulted in the developments often being arbitrary and narrowly specific rather than interconnected elements of a coherent evaluation system.” [38]

FRP’s manufacturers are usually mainly interested in the mechanical properties manifest in fiber-dominated situations. The data needed to characterize a composite material are usually: [39]

- Tensile modulus
- Compressive modulus (uniaxial)
- Flexural modulus
- Shear modulus (in plane)

- Poisson’s ratios
- Tensile strength
- Compressive strength (uniaxial)
- Flexural strength
- Apparent interlaminar shear strength
- Fracture toughness (various modes)

Many of this properties are usually provided by the manufacturers or can be obtained by static tests.

Focusing on fatigue behaviour of FRP, are regarded as having good fatigue resistance. For that reason, many studies have been done on them. As known composites are, by nature, inhomogeneous and frequently anisotropic. For that reason, performing tests in the major loading regimes could be difficult to execute. In some cases, there are no formal standards for fatigue testing of these materials. This is partly because of the difficulty in performing fatigue tests on polymer composites but also because it is only recently that standards have been developed for static testing [38].

2.2.2 STRESS – LIFE CURVES (S – N)

Essentially any test method used for static testing has the potential to be used in fatigue. However, the fatigue environment is usually more demanding on both material and test technique. Problems which do not occur in static testing will almost certainly do so in fatigue loading [38].

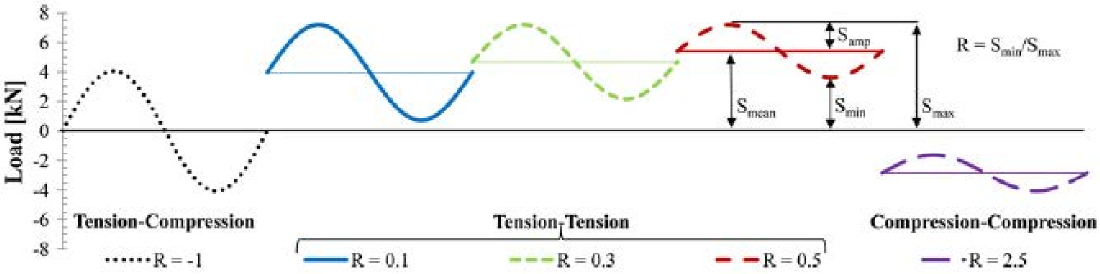

***Figure 2.13**: Example sinusoidal constant amplitude load waveforms showing definition of terms and illustration of R-values [41]*

Figure 2.13 shows a typical applied load waveform diagram in a fatigue test. The cyclic load is applied between a maximum and minimum limit, the ratio, which is the stress ratio R, is shown in **Equation 2.3**. The cyclic stress mode can be sinusoidal, triangular, square or whatever the user needs to focus on.

$$R = \frac{\sigma_{min}}{\sigma_{max}}$$

Equation 2.3

Originating from metals materials fatigue behaviour investigation, stress – life diagrams are often utilized for composite materials to understand the life cycle. A complete S-N diagram can be obtained using power-law regression equations [41]. In **Figure 2.14**, an S-N curve for a FRP, carbon-epoxy $[\#(\pm45)]_{24}$ with R =10 is shown.

Because of the complex nature of composite fatigue, the most important point regarding S-N curves is the large experimental scatter which is found in the literature. Even when the loading pattern, materials used, lay-up, thickness, test method,... are the same, imperfections and manufacturing defects are unavoidable and result in a large amount of scattering compared to metal S-N curves [42] [29].

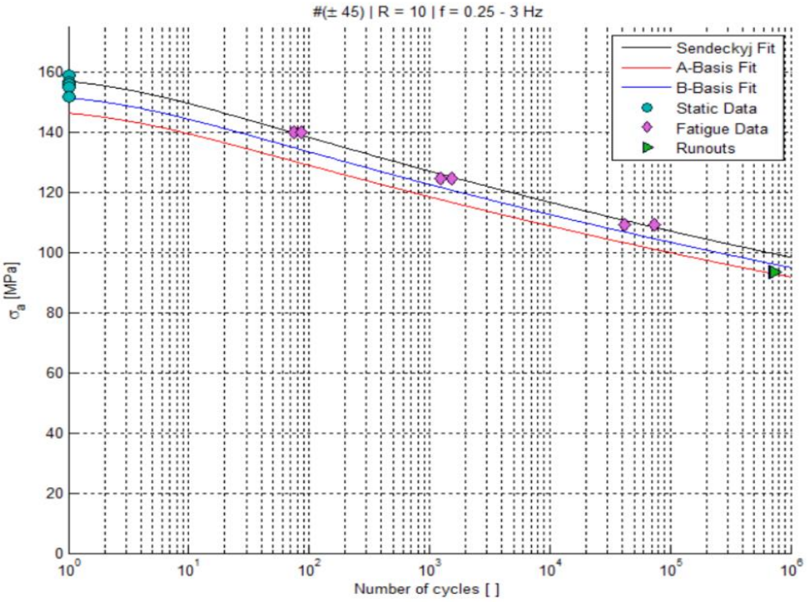

Figure 2.14: *S-N curve for the case of [#(±45)]$_{24}$ with R =10 [29]*

2.2.3 COMPRESSION TEST METHODS

Most of the literature about fatigue testing on FRP are involved in uniaxial tension-tension cyclic test. Tension-compression and compression-compression cyclic tests are not commonly used since many problems could occur [39]:

- Problems related to the load application that must be perfect parallel to the fiber direction
- Uniform stress field on the gauge length
- Acceptability of the failure modes (the breaking must occur in a specific region of the specimen, under specific load conditions)
- Easy data acquisition
- Geometrical specs of the specimen required (dimensional tolerances, tabs at the specimen ends…)
- Equipment requirements (dimensional tolerances, dimensions, weight, cost, reliability…)
- Representativeness of results
- Specimen buckling

This requires that either short and, therefore, self-stable coupons, or antibuckling guides are necessary to support the coupon. Short stable coupons, which may be parallel-sided or waisted, suffer from the disadvantage that the stress distribution in the free length may be affected by the restraint at the grips. Long coupons are to be preferred, but when a compressive excursion is to be included in the fatigue cycle, it is necessary to provide support to prevent buckling. No standard antibuckling guide exists, each test laboratory having developed its own devices [38].

Starting from the 1970s special tools have been developed to prevent Euler buckling of the specimens during the tests. Often, the limits applied to the sample cannot represent the real loading conditions during the life cycle of the material.

Some of the main compression methods are listed below (see **Figure 2.15**):

- **Shear Loaded Specimen Test Methods**: the typical problem of that method is that when the clamps grip the specimen, a non-uniform stress field could appear on the gauge length:
    - Celanese (ASTM D 3410)
    - IITRI (ASTM D 3410)
- **End Loaded Specimen Test Methods:** The critical issue of that method is the possibility of crushing of the specimen end:
    - ASTM D 695 Modified
- **Sandwich-Beam Specimen Test Methods:** With this method the facesheet under compression load is very thin compared to the sample dimensions. It ensures a uniform stress field on the material. At the end, with that method the final values are usually higher than in reality:
    - ASTM D 5467
- **Combined Loading Compression (CLC) Test Fixture:** This test method determines the compressive strength and stiffness properties of polymer matrix composite materials using a combined loading compression (CLC) test fixture:
    - ASTM D 6641

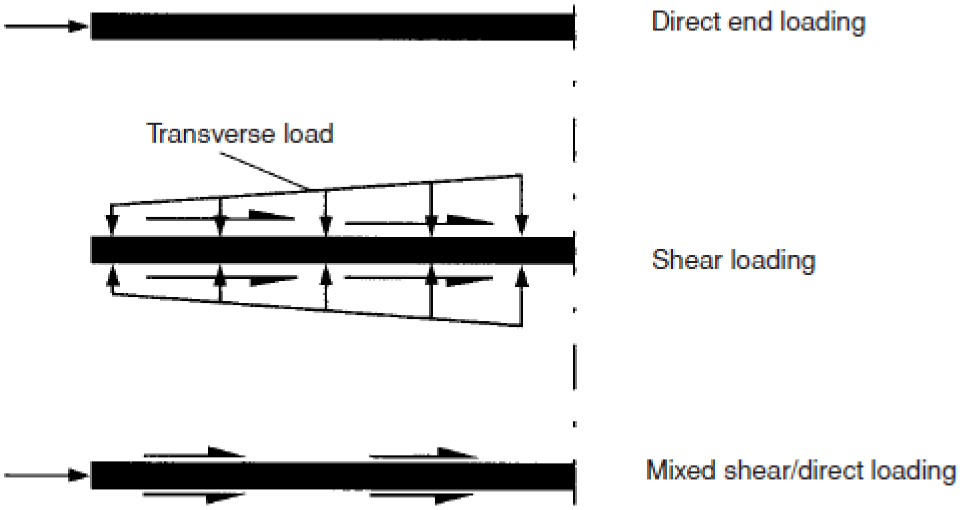

***Figure 2.15**: Load introduction methods for compression tests [38]*

2.2.3.1 Shear Loaded Compression Test Method - ASTM D 3410

“This test method determines the in-plane compressive properties of polymer matrix composite materials reinforced by high-modulus fibers. The composite material forms are limited to continuous-fiber or discontinuous-fiber reinforced composites for which the elastic properties are especially orthotropic with respect to the test direction. This test procedure introduces the compressive force into the specimen through shear at wedge grip interfaces” [45].

A flat strip of material having a constant rectangular cross section, as shown in the specimen drawings of **Figure 2.16**, is loaded in compression by a shear force acting along the grips. The normative also indicates other alternative geometries for the samples, i.e. quotes in inches and sample without tabs. The shear force is applied via wedge grips in a specially-designed fixture.

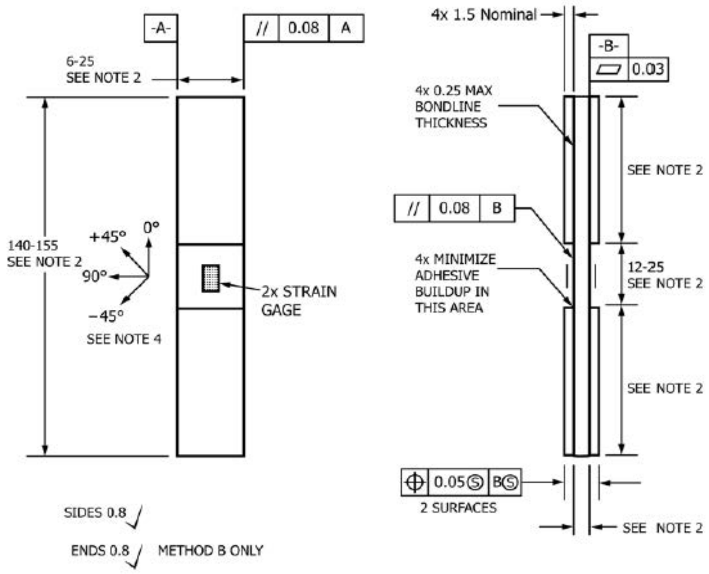

Notes:
1. Drawing interpretation per ANSI Y14.5M-1982 and ANSI/ASME B46.1-1985.
2. See Section 8 and Table 2 and Table 3 of the test standard for values of required or recommended width, thickness, gage length, tab length and overall length.
3. See test standard for values of material, ply orientation, use of tabs, tab material, tab angle, and tab adhesive.
4. Ply orientation tolerance relative to -A- ±0.5°.

Figure 2.16*: Compression test specimen drawing on ASTM D3410 [45]*

"The gage section for this test method is unsupported, resulting in a tradeoff in the selection of specimen gage length and the specimen thickness. The gage length must be short enough to be free from Euler (column) buckling, yet long enough to allow stress decay to uniaxial compression and to minimize Poisson restraint effects as a result of the grips." [45] Minimum thickness requirements are also provided by the normative.

Buckling must be avoided, the norm gives an equation to calculate the minimum thickness necessary to prevent Euler (column) buckling (see Equation 2.4)

"Specimen thickness, gage length, and width are related by the following equation. The lower the expected modulus and the higher the expected ultimate compressive stress, the greater the specimen thickness must be in order to prevent Euler (column) buckling in the test section."

$$h \le \frac{l_g}{0.9069\sqrt{\left(1-\frac{1.2F^{cu}}{G_{xz}}\right)\left(\frac{E^c}{F^{cu}}\right)}}$$

Equation 2.4

Where:

- h = thickness of the sample
- E^c = longitudinal modulus of elasticity, MPa
- F^{cu} = ultimate compressive stress, Mpa
- G_{xz} = through-thickness shear modulus, MPa
- l_g = length of gage section, mm

Properties, in the test direction, that may be obtained from this test method include:

- Ultimate compressive strength
- Ultimate compressive strain
- Compressive modulus of elasticity
- Poisson's ratio in compression
- Transition strain

The normative also gives information about the failure modes and areas that can be accepted and introduce a failure identification code as follows: "Failure Identification Codes: Record the mode, area, and location of failure for each specimen. Choose a standard failure identification code based on the three-part code shown in **Figure 2.17**. A multimode failure can be described by including each of the appropriate failure-mode codes between the parentheses of the M failure mode." [45]

The normative gives also the formulation to calculate the compressive stress/strain, the modulus of elasticity and the Poisson ratio

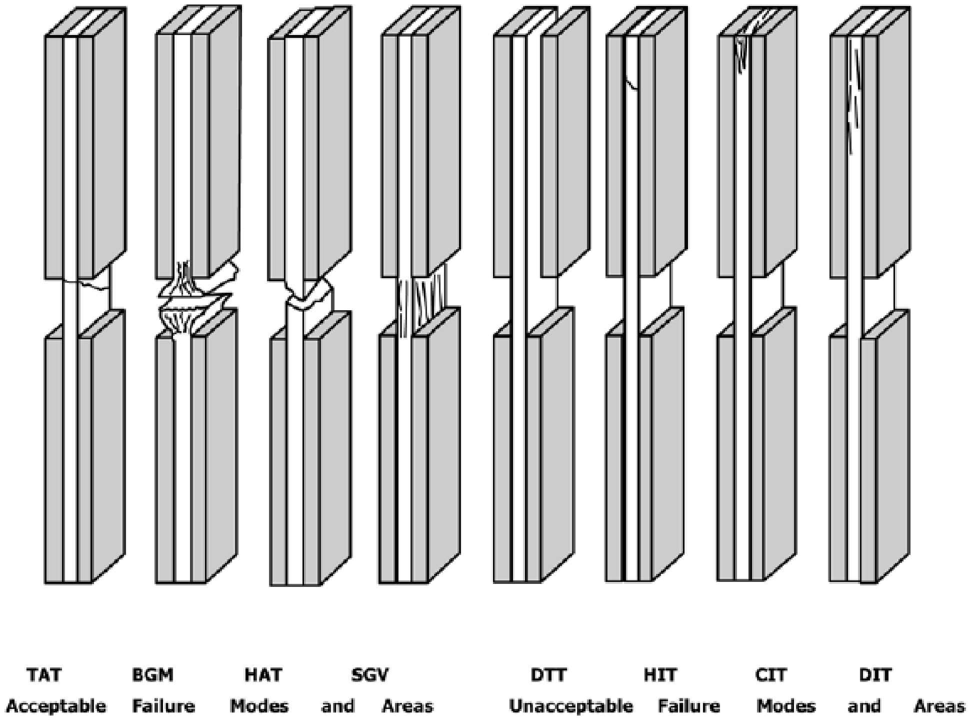

First Character

Failure Mode	Code
Angled	A
Brooming	B
end-Crushing	C
Delamination	D
Euler buckling	E
tHrough-thickness	H
Kink bands	K
Lateral	L
Multi-mode	M(xyz)
long.-Splitting	S
Transverse shear	T
eXplosive	X
Other	O

Second Character

Failure Area	Code
Inside grip/tab	I
At grip/tab	A
Gage	G
Multiple Areas	M
Tab adhesive	T
Various	V
Unknown	U

Third Character

Failure Location	Code
Bottom	B
Top	T
Left	L
Right	R
Middle	M
Various	V
Unknown	U

Figure 2.17: *Failure identification codes and overall specimen failure schematics [45]*

- CELANESE TEST METHOD:

This test method was introduced by Celanese Corp in 1970s and it was the first method to be standardized by ASTM in 1975.

One of the first fixtures to be developed using this principle is known as the Celanese fixture. The specimen is held in conical wedge grips which are accommodated in tapered sleeves. An outer cylinder maintains the alignment of the parts. When the load is applied to the sleeves it is transmitted to the specimen by shear, through friction between the specimen and the grips [38] [39] [44].

This fixture needs careful adjustment to the thickness of the specimen if non-uniform load distribution on the cones is not to lead to distortion of the sleeves and friction with the outer cylinder. If precise overall specimen thickness dimensions are not adhered to, the conical wedges form a line contact with the outer sleeves, resulting in specimen instability and, consequently, lower bound strength values [38].

It is also possible, due to shear loading, to induce a non-uniform stress field in the areas near the tabs. This obviously can reduce the strength of the specimen, misrepresenting the final result of the test. [39]. **Figure 2.18** shows a schema of the Celanese test method.

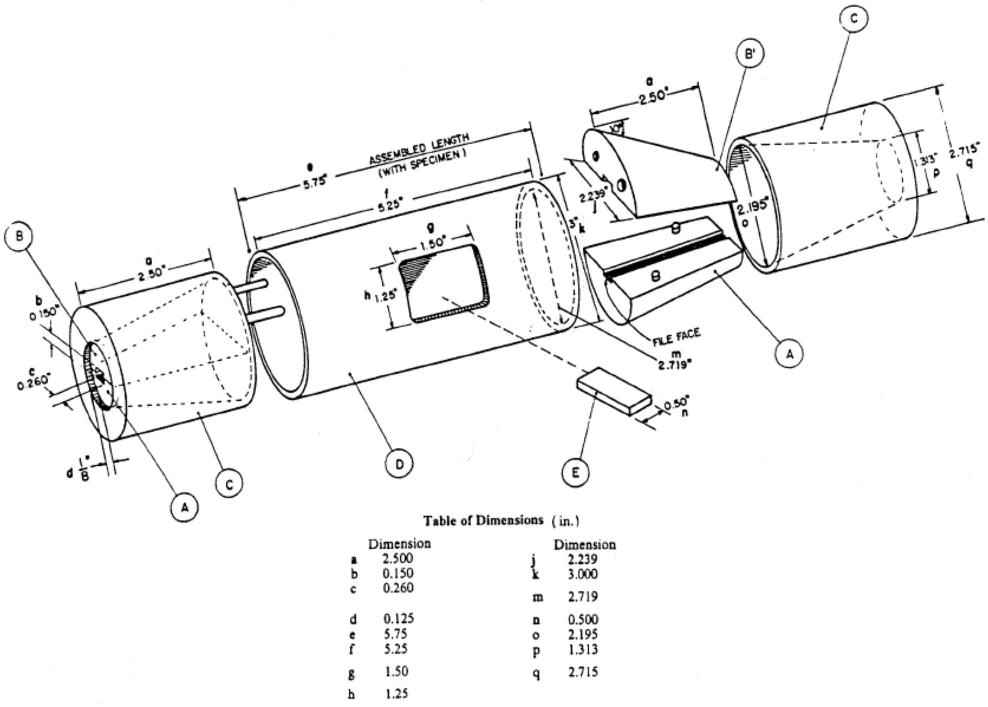

Table of Dimensions (in.)

	Dimension		Dimension
a	2.500	j	2.239
b	0.150	k	3.000
c	0.260	m	2.719
d	0.125	n	0.500
e	5.75	o	2.195
f	5.25	p	1.313
g	1.50	q	2.715
h	1.25		

***Figure 2.18**: Celanese compression test fixture*

ASTM D 3410 was the first normative containing a standardized method for compression testing. It was created ad hoc for Celanese method in 1975. In 2003 this method was deleted from the normative, to be replaced by IITRI method, explained below.

- IITRI TEST METHOD (Illinois Institute of Technology Research Institute)

A fundamental modification of the Celanese fixture was developed by the Illinois Institute of Technology Research Institute (IITRI).

Here, flat-sided tapered grips, which fit into matching pockets in massive steel blocks, are used rather than conical ones, so that specimens of different thicknesses can be easily accommodated. The steel blocks are aligned by pillar guides and linear bearings. [38] A schematic diagram of the IITRI clamps, compared with the Celanese clamps is shown in **Figure 2.20** and the assembled and disassembled jigs are shown in **Figure 2.19**.

Buckling with IITRI test method buckling can occur, it is due to the trapezoidal wedges that avoid lateral deformation of the tabs but does not prevent the lateral deformation of the gauge length.

The only limits of that method are the weight and the dimensions of the equipment, other than the price. Also, this fixture cannot be used for fatigue because the clamps are not suitable for this option, due to the high weight.

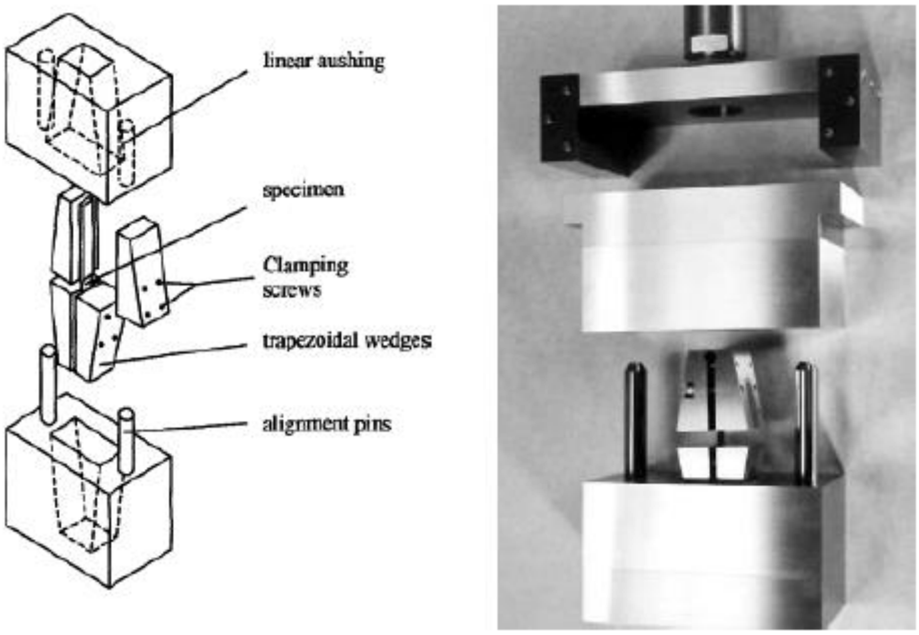

***Figure 2.19** Schema of IITRI test method [39] [44]*

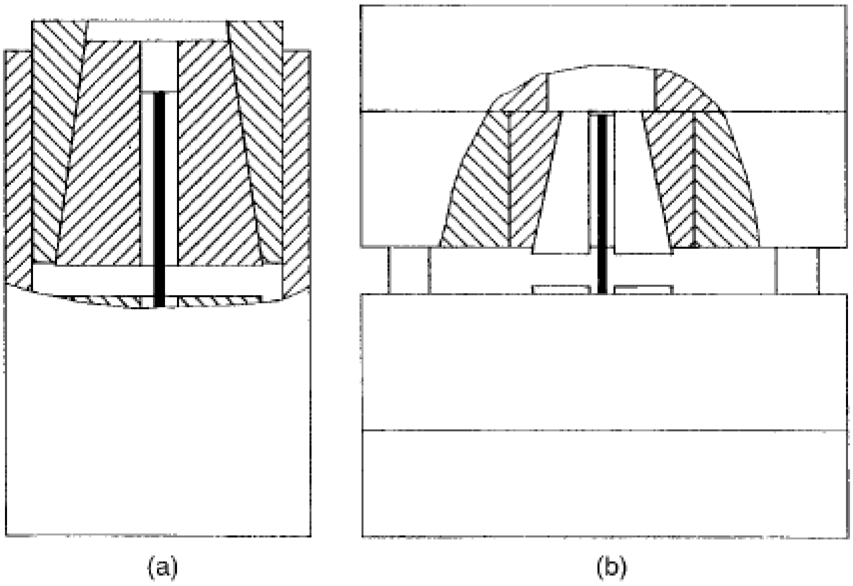

Figure 2.20: Diagrammatic comparison of Celanese (a) and IITRI (b) clamps [38]

2.2.3.2 End Loaded Specimen - ASTM D 695 MODIFIED

During the first 1980s, Boeing Co. and the Hercules Inc. developed a new compression test for composites material, starting from the ASTM D 695 method, initially used for rigid plastics materials.

The main modification was to change the bone specimen shape to a rectangular section sample with tabs at the end of it. The tabs were introduced to avoid the end crushing of the specimen, typical of the end loaded specimen test methods [39]. The differences between the original ASTM D 695 specimen geometry and the modified are shown in **Figure 2.21**.

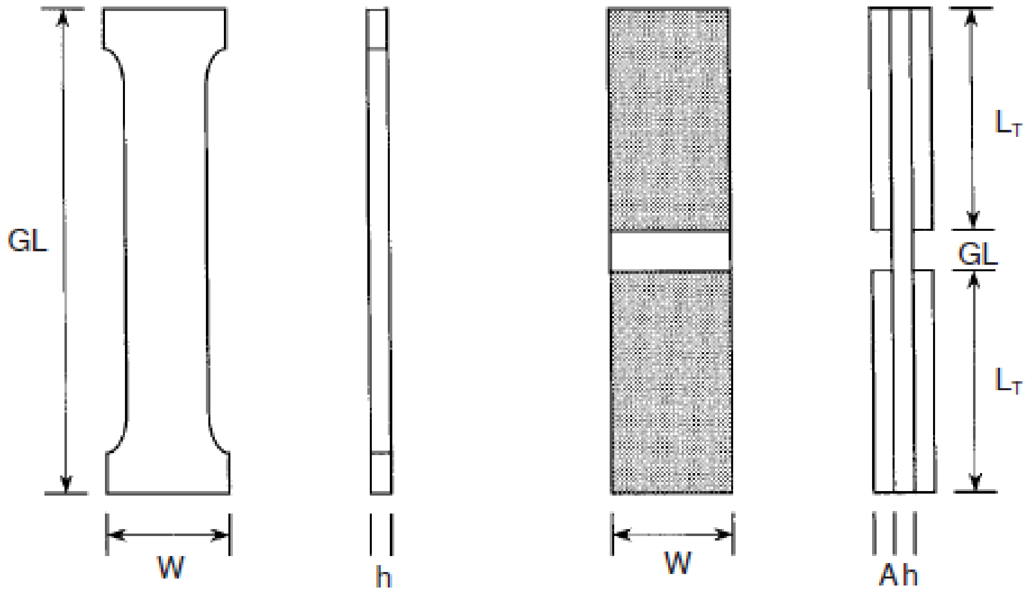

Figure 2.21: Specimen configurations for ASTM D 695 (left) and modified ASTM D 695 (right) [38]

With that method, a small part of the load is introduced to the specimen by shear through the end-tabs, depending on the stiffness of the tabs and bond layer. This is due to the clamps that have to keep the specimen perfectly aligned to avoid buckling. An additional alignment device is recommended. Although the specimen requires careful preparation, the parallelism of the specimen ends is particularly important, and the test jig is of remarkable simplicity, cheap to manufacture and easy to use. Owing to the transverse constraint of Poisson's deformation, the specimen may experience some transverse loading which, in turn, leads to friction between the support faces and the specimen [38].

A schematic representation of the compression jigs with the specimen mounted is shown in **Figure 2.22**.

As with any of the direct end-loaded specimen test methods discussed in later sections, end crushing of strong materials is a problem. The bigger limit for this method is the impossibility to mount any kind of extensometer on the specimen because the gauge length is small and not visible due to the anti-buckling guides covering it [39] [38].

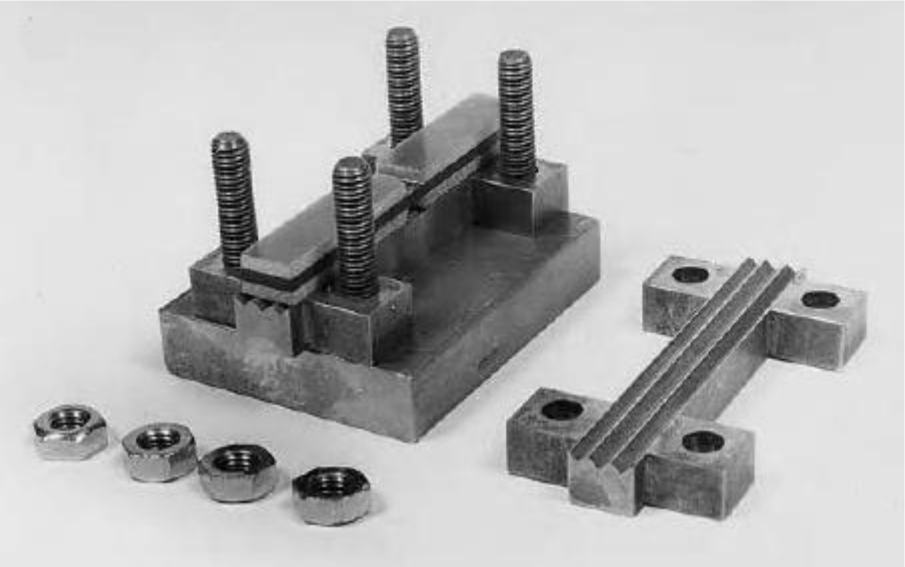

Figure 2.22: *Disassembled compression jigs with specimens mounted for ASTM D 695 modified*

2.2.3.3 Sandwich-Beam Specimen Test Methods – ASTM D 5467

This method entered officially in ASTM D 3410 with the others IITRI and Celanese in 1987. In 1993 was deleted from ASTM D 3410 and entered in ASTM D 5467 [39] [38] [45] [49].

In **Figure 2.23** the ASTM D 5467 test fixture is shown.

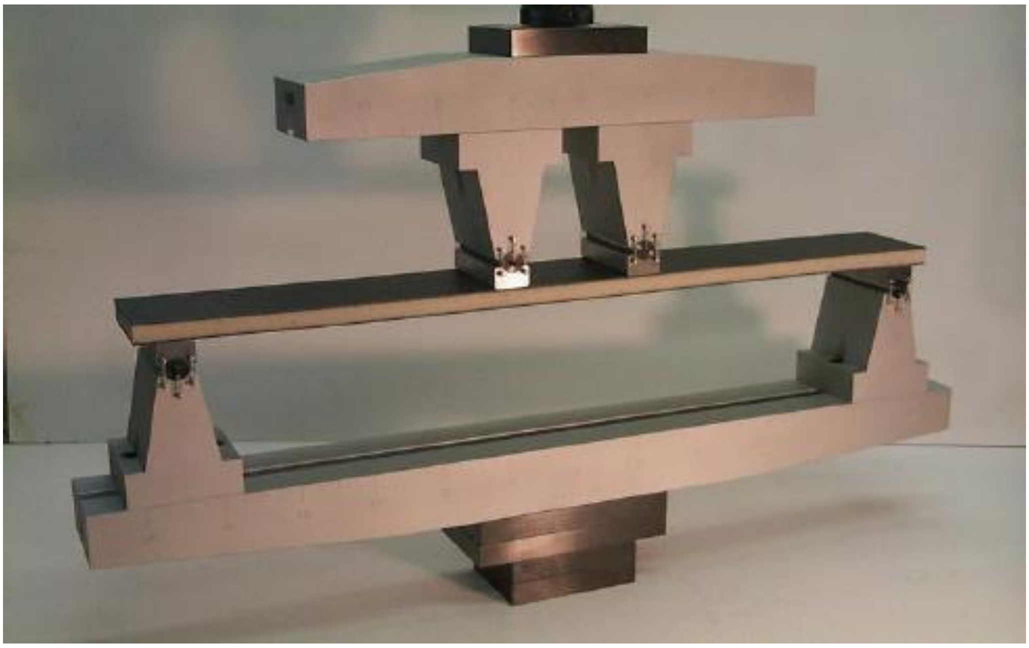

Figure 2.23*: ASTM D 5467 Test Fixture*

A sandwich beam composed of two facesheets separated by a relatively thick honeycomb core, as shown in **Figure 2.24**, is loaded in four-point bending. The main component of the compression test specimen is the face sheet that is loaded in compression during flexure, with the material direction of interest oriented along the length of the beam. The other facesheet is of a material and size carefully selected to preclude its influence on the test results. The ultimate compressive strength of the material is determined from the load at which the test facesheet of the sandwich beam fails in an acceptable compression failure mode [49].

The facesheet under compression load is very thin compared with the sample dimensions. It ensures a uniform stress field on the material [39].

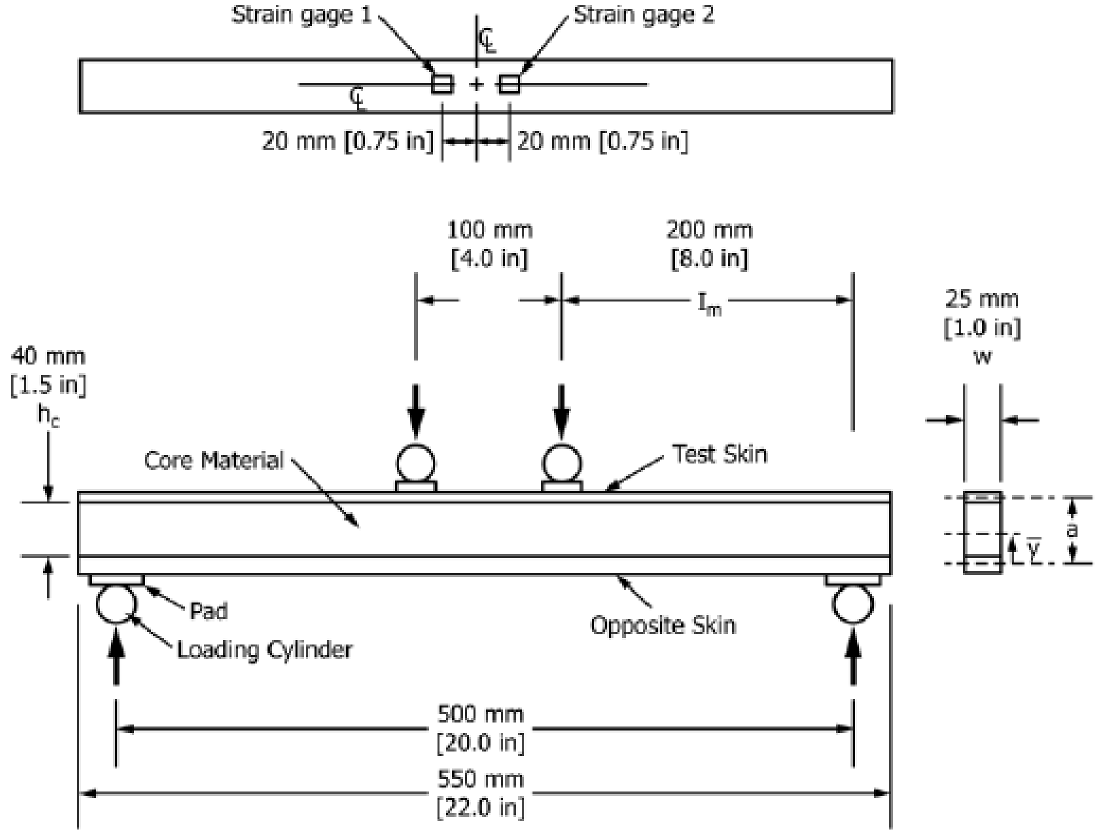

Figure 2.24: *ASTM D 5467 – Longitudinal compression sandwich beam test specimen*

The normative also record the mode, the area, and location of failure for each specimen. It gives a standard failure identification code based on the three-part code described in Test Method D 3410 and shown in **Figure 2.25**.

The objective of this test method is to load the sandwich beam in four point flexure and fail the upper (compressively loaded) facesheet in compression. Therefore, the acceptable failure modes for this test method are those that occur in the compressively loaded face and include one of the acceptable compression failure modes of Test Method D3410. Unacceptable failure modes include core shear, core crushing, local wrinkling, or separation of the core from the facesheet. The acceptable failure area is within the central 50 mm of the gage section of the test facesheet [49].

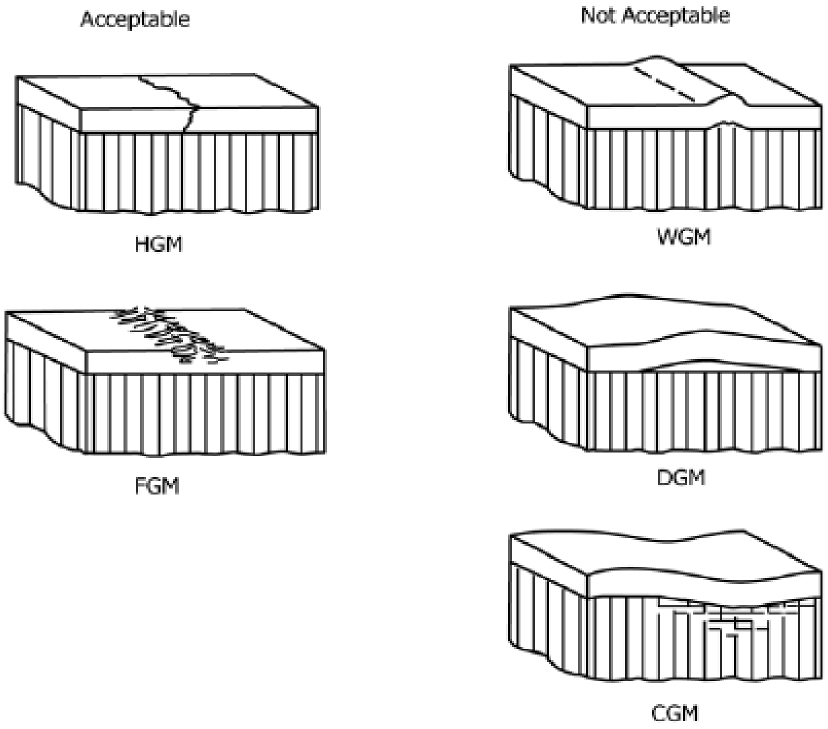

First Character

Failure Mode	Code
skin to core Delamination	D
Filament fracture	F
tHrough-thickness	H
Layer instability	L
local Wrinkling	W
Multi-mode	M(xyz)
core Crushing	C
long.-Splitting	S
Transverse shear	T
eXplosive	X
Other	O

Second Character

Failure Area	Code
At load cylinder	A
Gage	G
Multiple Areas	M
Outside gage	O
Various	V
Unknown	U

Third Character

Failure Location	Code
Left	L
Right	R
Middle	M
Various	V
Unknown	U

Figure 2.25*: ASTM D 5467 – Sandwich beam test specimen failure identification codes and overall specimen failure schematics [49]*

The results obtainable with this method are very sensitive at every premature failure of the core of the sandwich and of the adhesive between the skins and the core. These results are not representative of the real material because the honeycomb core avoid microbuckling, that can appear in real laminates [39].

2.2.3.4 Combined loading compression test method – ASTM D 6641

It is been explained that methods which induce shear load to the specimen can generate stress concentration in the gauge length. The methods that carry load to the specimen through the ends of it are subjected to critical manufacturing processes due to the tabs cutting and bonding. (it is also possible to have a non-uniform stress field on the specimen gauge length) [39]. This reasoning led to thinking a way to combine the end-load and the shear load test specimen method. During 1990s Wyoming's University developed a new test method based on that concept. This method, called "Combined Loading Compression (CLC) Test Fixture", was introduced on ASTM D 6641 normative in 2001 [39] [50].

ASTM D 6641 normative says: "This test method determines the compressive strength and stiffness properties of polymer matrix composite materials using a combined loading compression (CLC) test fixture. This test method is applicable to general composites that are balanced and symmetric. The specimen may be untabbed (Procedure A) or tabbed (Procedure B), as required. One requirement for a successful test is that the specimen ends do not crush during the test. Untabbed specimens are usually suitable for use with materials of low orthotropy, for example, fabrics, chopped fiber composites, and laminates with a maximum of 50% 0° plies, or equivalent. Materials of higher orthotropy, including unidirectional composites, typically require tabs."

The fixture, shown in **Figure 2.26** and **Figure 2.27**, which subjects the specimen to combined end and shear loading, is itself loaded in compression between flat plates in a universal testing machine.

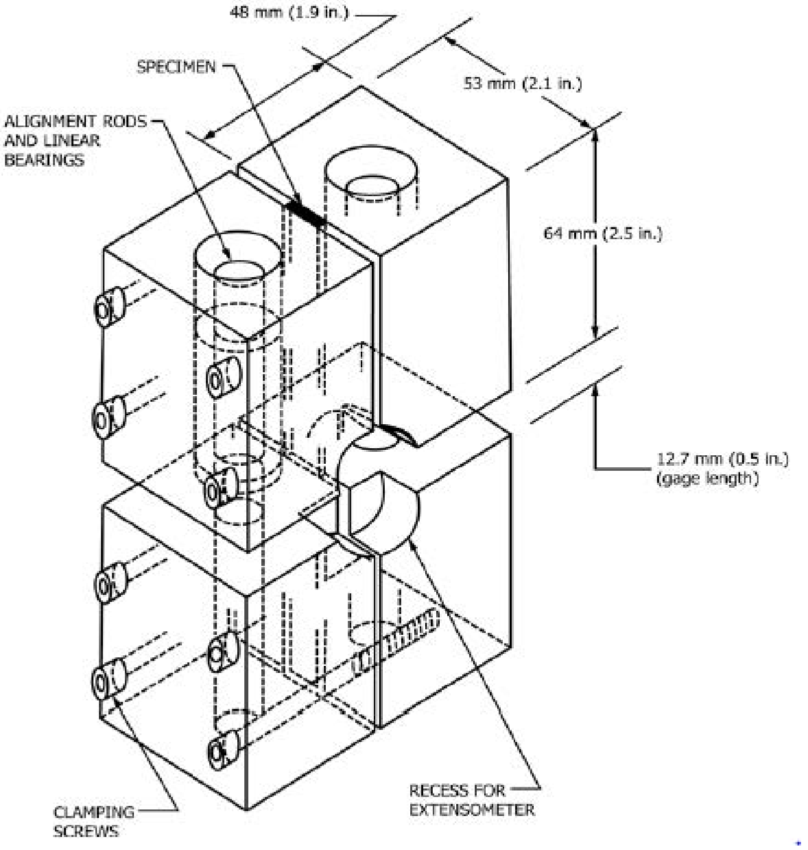

Figure 2.26: *Dimensioned sketch of a CLC test fixture [50]*

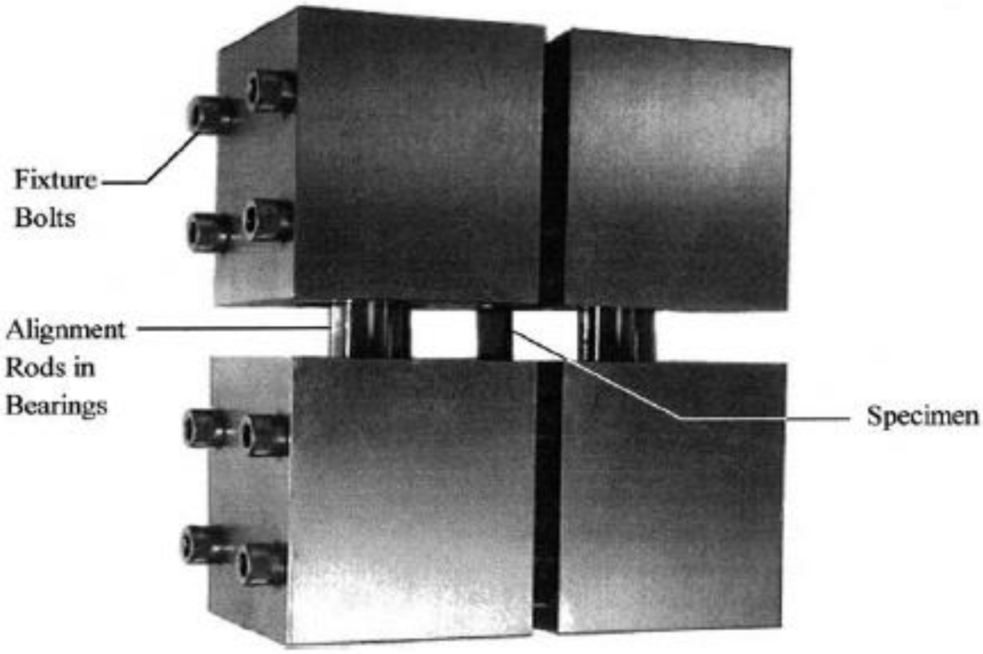

Figure 2.27: *A photograph of a typical CLC test fixture [50]*

The normative gives also indication about geometry of the specimens: “Because of partial end loading of the specimen in this test method, it is important that the ends of the specimen be machined flat, parallel to each other, and perpendicular to the long axis of the coupon (see **Figure 2.28**), just as for Test Method D695. Improper preparation may result in premature end crushing of the specimen during loading, excessive induced bending, or buckling, potentially invalidating the test. For a valid test, final failure of the specimen must occur within the gage section.”

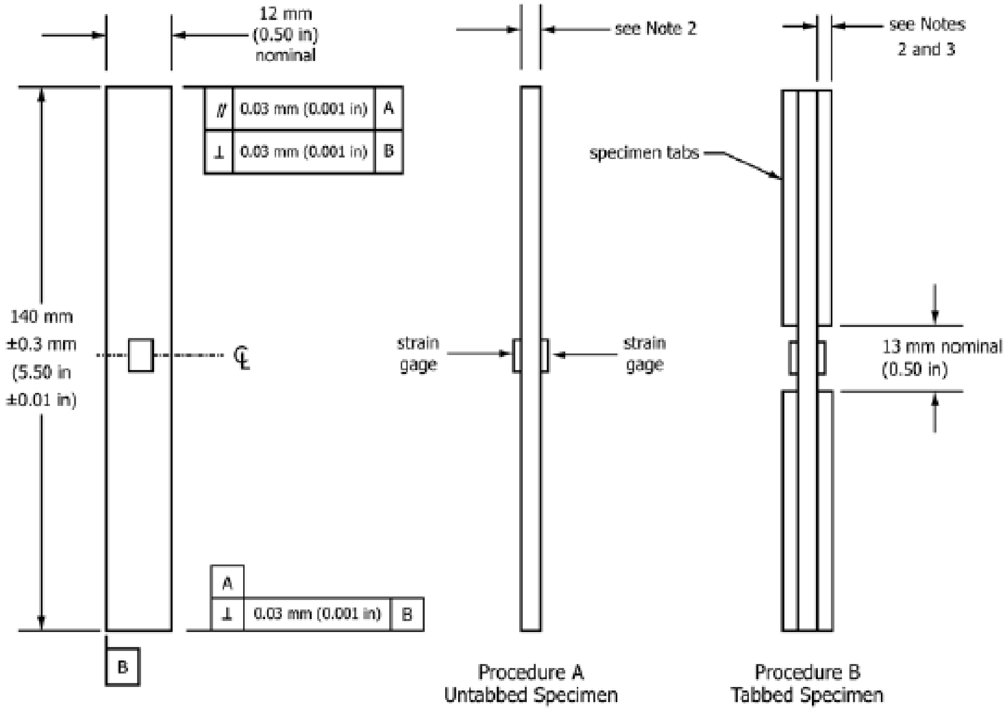

Figure 2.28: *Typical ASTM D 6641 Test specimen configuration [50]*

For valid tests, final failure of the specimen will occur within the gage section. The failure mode may be brooming, transverse or through-thickness shear, longitudinal splitting, or delamination, among possibly other forms. Which failure modes are deemed acceptable will be governed by the particular material, laminate configuration, and application. Acceptable failure modes are illustrated in Test Method D 3410. The occurrence of Euler buckling invalidates the test [50].

An important analysis of this method was done by Adams and Welsh [51]. After a lot of tests done with $[(90/0)_n]_s$ without tabs, they confirm the test as the most easy and reliable test method for compression of composites materials. The tabs absence allows easier specimen manufacturing. The use of cross-ply laminates allows to obtain very reliable results of the ultimate strength of the laminate. [51]

As well as for others for the other compression test methods, buckling must be avoided. The short gauge length characteristic of this technique is absolving this purpose. Otherwise it is also a limit for the application of extensomers and eventually for the use of DIC cameras.

2.2.3.5 Summary of the test methods

A bullet list is presented below, to explain the advantages and the disadvantages of each test method presented in this chapter:

- **Celanese (ASTM D 3410)**

  The main limit of this test method are the non-visibility of the gauge length during the test and the difficult positioning of the clamps. Has also to be mentioned that problems associated with load introduction and free edges can occur if the alignment of the clamps or the geometry of the sample are not good.

- **IITRI (ASTM D 3410)**

  No special problems associated with load introduction and free edges can occur. This fixture is unique in that it is the only commonly used shear-loaded compression fixture capable of testing a wide specimen. The gauge length is visible during the test.

- **ASTM D 695 Modified**

  As with any of the direct end-loaded specimen test methods discussed in later sections, end crushing of strong materials is a problem. Thus, the straight-sided compressive strength specimen is tabbed, to increase the bearing area. Flatness and parallelism of the specimen ends is important so that the loading can be introduced uniformly. Tabs are required. The gauge length is not visible during the test because of the anti-buckling guides placed in front of the sample.

- **Sandwich-Beam (ASTM D 5467)**

  The compressive face sheet is thin relative to the overall beam depth. Thus, it is, to a good approximation, in uniform compression. The test method is very sensitive to any premature failures in the core material or its adhesive bond to the face sheets. The specimen preparation is difficult and require a lot of material.

- **Combined loading (ASTM D 6641)**

  Because of partial end loading of the specimen in this test method, it is important that the ends of the specimen be machined flat, parallel to each other, and perpendicular to the long axis of the coupon. Improper preparation may result in premature end crushing of the specimen during loading, excessive induced bending, or buckling, potentially invalidating the test. Samples can be tabbed or untabbed. The gauge length is short but it is always visible during the test.

A table with the major peculiarity of each test method is presented in **Table 1** below.

Loading	Test method name	Buckling	Short gauge lenght	Non uniform stress field	Gauge length not visible	End crushing	Tabs required
Shear load	Celanese - ASTM D 3410	X	X	X	X		X
	IITRI - ASTM D 3410	X	X	X			X
End loaded	ASTM D 695 Modified	X	X	X	X	X	X
Sandwich-Beam	ASTM D 5467						
Combined loading	ASTM D 6641	X	X	X			

***Table 1**: Compression tests methods comparison*

3 PREVIOUS WORKS

In this chapter, the previous works done by Stef Walraet and Pablo H. Jimenez will be explained chronologically. The objective of this chapter is to analyse and solve the issues encountered in the past works. All the improving of the past works will be used for the continuation of the project.

3.1 “C-C and T-C fatigue of woven carbon epoxy composites” S. Walraet [29]

3.1.1 Objectives

The objective of this research was to generate reliable fatigue test data for woven CFRPs loaded in compression-compression and tension-compression. The aim is to keep track of the evolution of parameters like:

- Stiffness
- Poisson’s ratio
- Permanent (shear) strain
- Occurrence of micro cracks

3.1.2 Set-up configuration

The first part of this master thesis consists of the design of a test set-up to perform fatigue experiments and capture relevant parameters in the process with a reliable reference figure. The system should be capable of the following:

- Perform fatigue experiments reliably so that they can be representative for a material's fatigue behaviour under repetitive loads
- Capture relevant data reliably at intervals sufficient to characterize the fatigue behaviour
- The system should be relatively simple in use

Both quasi-static and fatigue tests have been performed for this work. The available used infrastructure and measurement equipment is shortly discussed here:

- All experiments have been carried out on an **Instron 8801 (100kN) servohydraulic fatigue testing system**, suitable for both high and low cycle fatigue. This system is capable of handling loads up to 100 kN both in compression and in tension.
- The most important source of data acquisition for this thesis has been **DIC**. Two sets of cameras have been utilized. Both camera types allow for external (hardware) triggering. Most measurements were performed using a set of two **Point Grey** Grasshopper USB 3.0 cameras.
- Static strain measurements have also been confirmed using **strain gages**. These are manufactured by Vishay (micro-measurements).
- Specimen heating during cyclic tests should be avoided. Heating can become so severe that material properties are altered, and test results become difficult to interpret. Particularly when off-axis fibers are included, heating can become severe. In order to keep track of this, samples were fitted with a **thermocouple** during measurements.

- In the set-up developed throughout this master thesis, **signal processing** to obtain inputs and send outputs from different sources or to different receivers has been an important concern. Data acquisition and output signaling were performed using National Instruments X- and C-series hardware.
- **Optical microscopes** have been used for damage assessment for this thesis. Two types have been used, a Carl Zeiss Jenavert metallurgical microscope with possible magnifications up to 100x and a Keyence VHX-2000 digital microscope, with possible magnifications up to 2500x, possibilities for image stitching and depth-up 3D imaging.

Two possible system lay-out have been designed and tested, to be used based on in-house availability of measurement equipment, data acquisition hardware and software dongles. While the backbone of both systems is the same LabView program, they are differentiated in the way cameras are controlled and analog data is retrieved. The first system triggers cameras through an X-series card hardware using drivers of the manufacturer, the second works solely through National Instruments' drivers and software triggers using a C-series card. A schema of the LabView triggered system is shown in **Figure 3.1**.

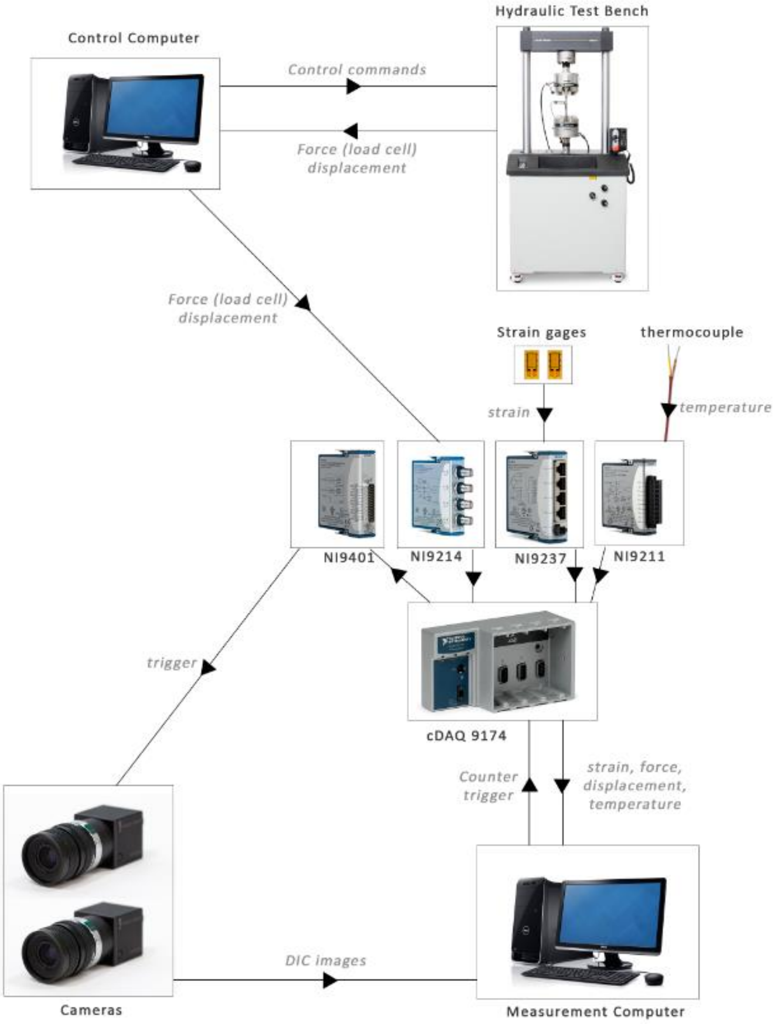

***Figure 3.1**: LabView triggered system [29]*

3.1.2.1 DIC cameras

As mentioned before, the use of DIC has been an important asset for this thesis. It allows for entire displacement field quantifications for quasi-static and fatigue tests, which results in a much larger pool of information compared to the conventional strain measuring methods (extensometer, strain gage,..).

Two DIC measurement setups were used to obtain a 3D displacement field. The eyesight principle is imitated, where two cameras are used to obtain a 3D image, capable of detecting out of plane motion. This is done by placing the cameras at an angle compared to each other (see **Figure 3.2**).

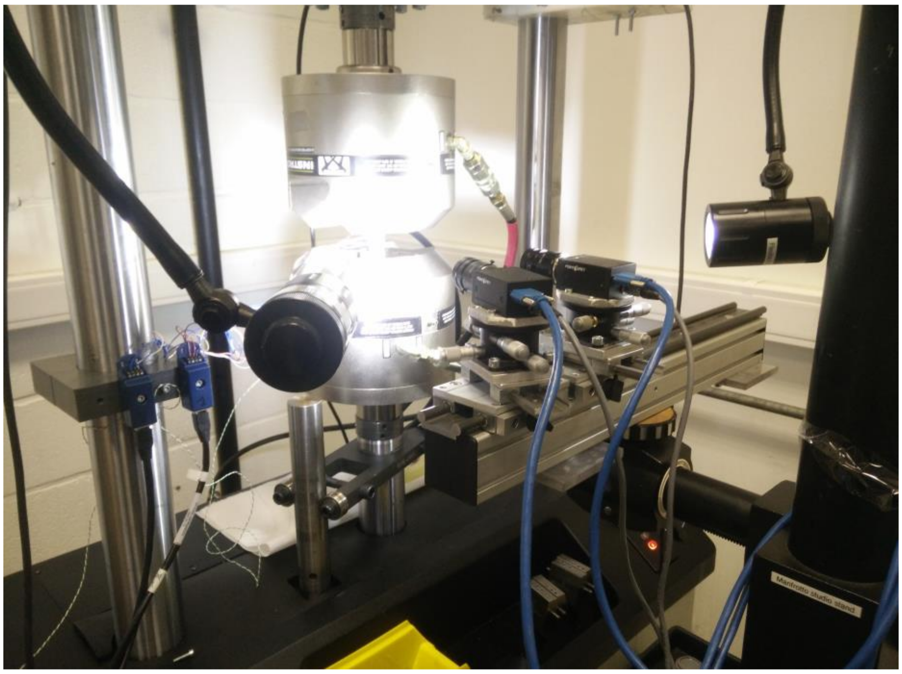

Figure 3.2: *Camera set-up for 3D DIC [29]*

The second attempt at capturing damage phenomena from the side of specimens, a system with two cameras each capturing one side of the specimen was tested. The side of the specimens can also be covered with a speckle pattern to allow for image correlation on the side of a specimen. This pattern is applied together with the front DIC pattern and is similar in terms of resolution. Through camera triggering in the same manner as for 3D DIC, images are still captured simultaneously and information of both can be combined. The lay-out is shown below in **Figure 3.3**. Not using 3D DIC means omitting any out-of-plane displacement data. However, this can be justified since previous tests confirmed minimal out-of-plane displacements for all load cases. If out-of-plane displacements would have been present despite this, they can be expected to be picked up by the camera aimed at the side of the specimen.

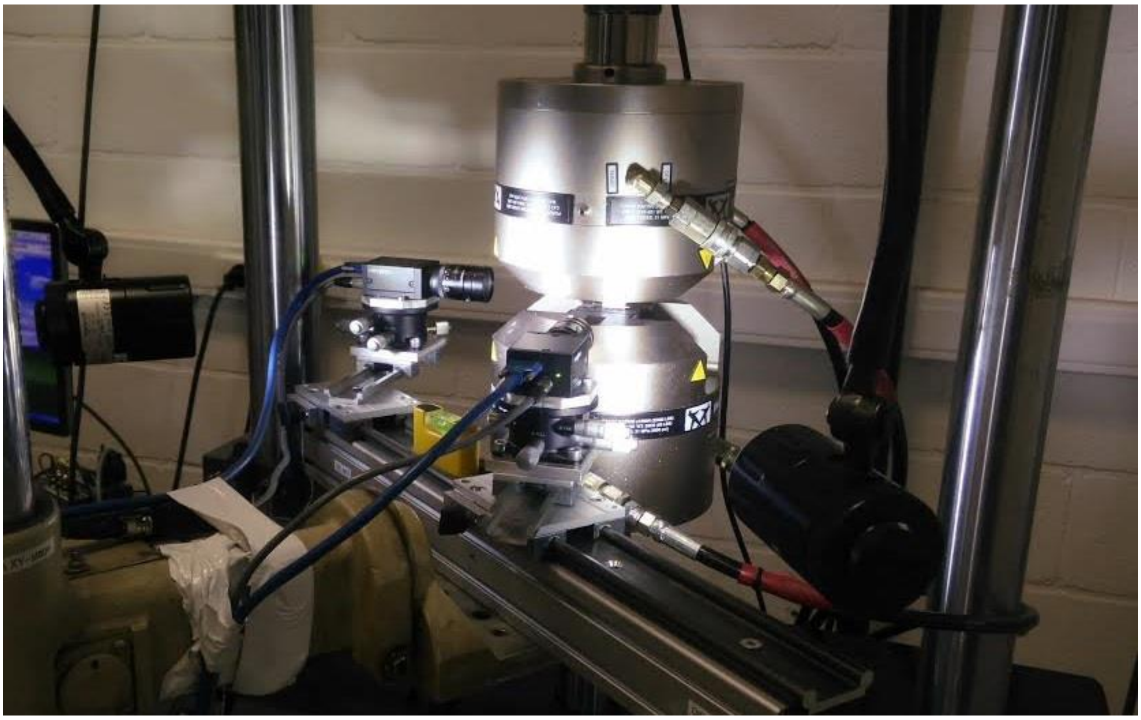

Figure 3.3: *Camera concept capturing two 2D images of a specimen rather than a single frontal 3D image [29]*

3.1.2.2 Measurement system evaluation

In order to test the performance of the system in cyclic loading, the test bench was used to create a rigid body motion (sine wave) of a sample. Analog displacement sensor data was compared to displacement data from DIC measurements. This was done for different motion frequencies and camera frame rates. As can be seen in **Figure 3.4**, there is a clear delay between the analog signal and DIC images, presumably obtained at the exact same moment. By determining this delay, it is possible to correlate analog and DIC data using a shift in time together with interpolation, which is required to match force data with DIC data at exactly the same time point.

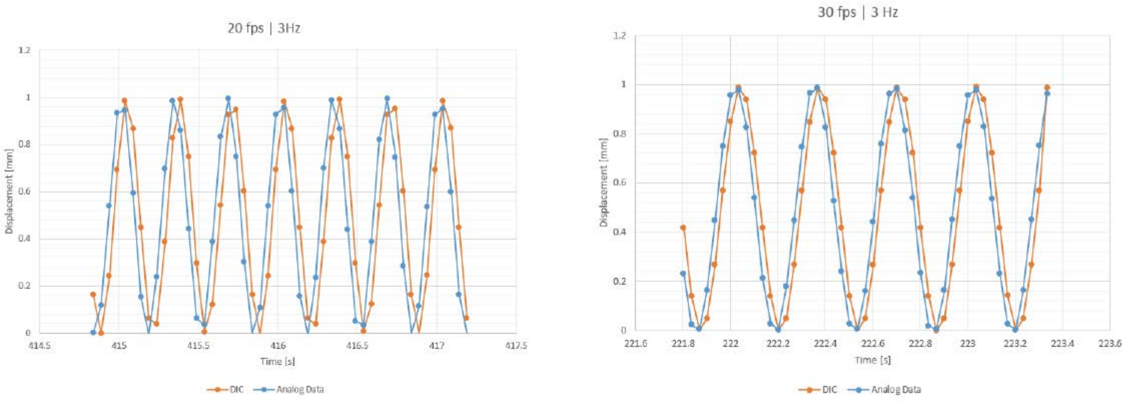

***Figure 3.4**: Rigid body motion of 1mm at 1Hz shots at different fps shows delay between signals*

To ensure efficient post-processing of data of the entire test program, a MatLab script was created to post-process, save and visualize data from fatigue tests. After reading and analyzing both data files (analog and DIC data), the program automatically corrects for delay and calculates the permanent strain and the stiffness evolution [29].

3.1.3 Material and specimen design

In this section, the available material is presented, followed by the specimen geometry design. Hereafter load transfer will be discussed.

3.1.3.1 Material

The material under investigation for this master thesis is a **plain woven carbon-epoxy**. Many plates were available in 8 or 24 layers, with all layers oriented in the same direction. The plates are produced by Mitsubishi Rayon Co., Ltd., one of the industrial partners involved in the M3 project. They are made using Pyrofil fibers denoted by TR30S 3L, with epoxy resin #360, at a resin content of 40 wt%.

The material properties as reported by the manufacturer are shown in **Figure 3.5**.

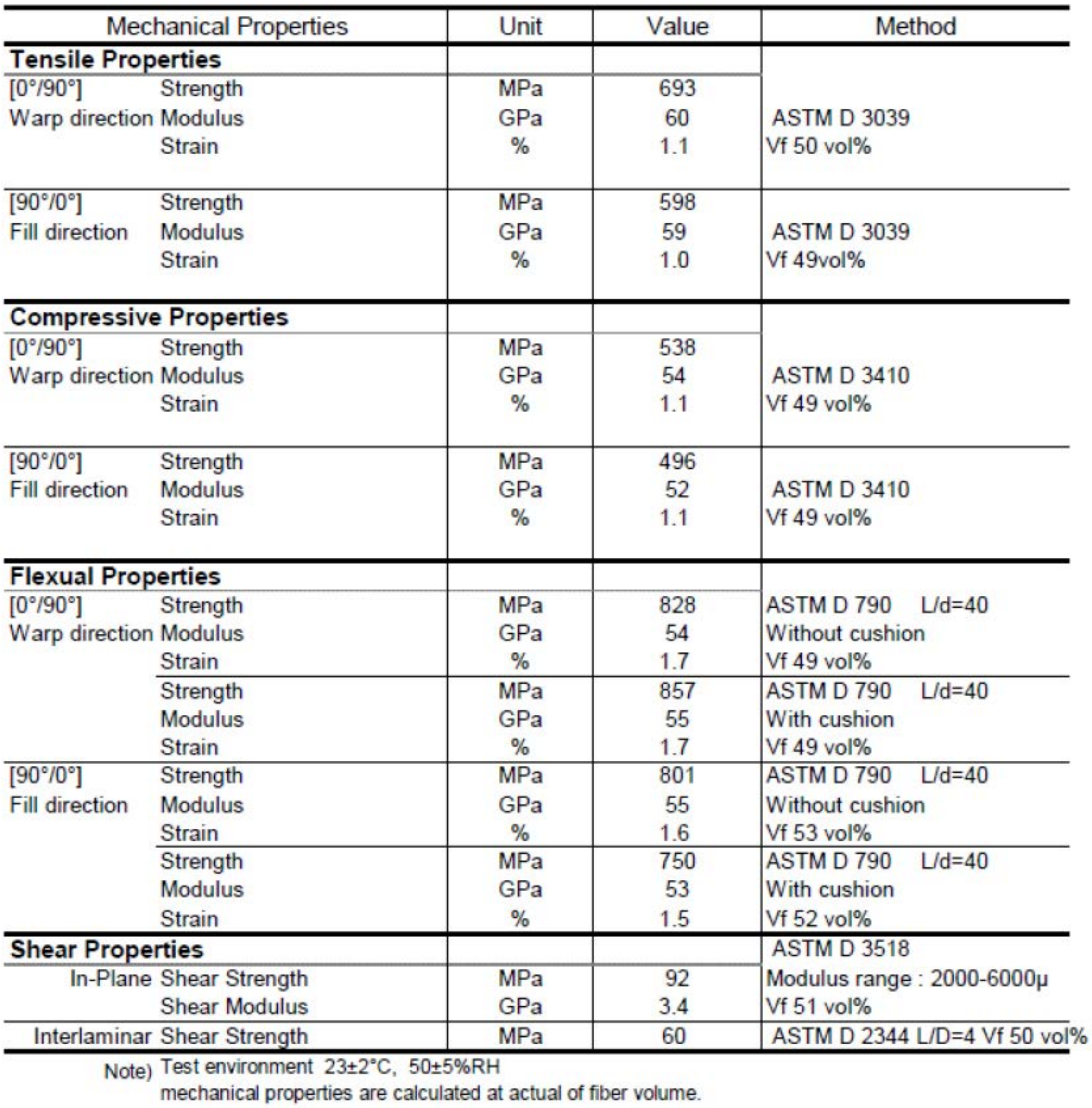

Mechanical Properties		Unit	Value	Method
Tensile Properties				
[0°/90°]	Strength	MPa	693	
Warp direction	Modulus	GPa	60	ASTM D 3039
	Strain	%	1.1	Vf 50 vol%
[90°/0°]	Strength	MPa	598	
Fill direction	Modulus	GPa	59	ASTM D 3039
	Strain	%	1.0	Vf 49vol%
Compressive Properties				
[0°/90°]	Strength	MPa	538	
Warp direction	Modulus	GPa	54	ASTM D 3410
	Strain	%	1.1	Vf 49 vol%
[90°/0°]	Strength	MPa	496	
Fill direction	Modulus	GPa	52	ASTM D 3410
	Strain	%	1.1	Vf 49 vol%
Flexual Properties				
[0°/90°]	Strength	MPa	828	ASTM D 790 L/d=40
Warp direction	Modulus	GPa	54	Without cushion
	Strain	%	1.7	Vf 49 vol%
	Strength	MPa	857	ASTM D 790 L/d=40
	Modulus	GPa	55	With cushion
	Strain	%	1.7	Vf 49 vol%
[90°/0°]	Strength	MPa	801	ASTM D 790 L/d=40
Fill direction	Modulus	GPa	55	Without cushion
	Strain	%	1.6	Vf 53 vol%
	Strength	MPa	750	ASTM D 790 L/d=40
	Modulus	GPa	53	With cushion
	Strain	%	1.5	Vf 52 vol%
Shear Properties				ASTM D 3518
In-Plane	Shear Strength	MPa	92	Modulus range : 2000-6000μ
	Shear Modulus	GPa	3.4	Vf 51 vol%
Interlaminar	Shear Strength	MPa	60	ASTM D 2344 L/D=4 Vf 50 vol%

Note) Test environment 23±2°C, 50±5%RH
mechanical properties are calculated at actual of fiber volume.

Figure 3.5: *Material data sheet from manufacturer [29]*

3.1.3.2 Specimen geometry

Since out-of-plane deformation introduces non-uniform stress fields and detrimental peel forces at fibre bundle edges, buckling is to be avoided at all cost.

To effectively prevent buckling, two options can be used. The first option is to design specimens such that unstable modes do not occur. Typically, this results in short gauge lengths, with certain implications:

- A short specimen clamped at both ends results in a restriction of a certain amount of Poisson contraction (or expansion) due to the clamping effects at the ends
- Strain gage, thermocouple and/or extensometer measurements become unpractical since they have to be performed on a small space

The shape and dimensions of a specimen are critical to ensure that the part of the specimen under consideration will fail first, under a known load which is of interest.

The second option is to create specimens with long gauge length where buckling is prevented through the use of anti-buckling guides. The concept is straightforward: a large stiff guide is placed in which the specimen only just fits. This will induce sideways forces which don't allow the specimen to buckle in any direction.

The use of anti-buckling guides shows lower static strengths. On top of this, the effect of the contact with the side in fatigue loading can be considered questionable. This resulted in the decision to design specimens so that unstable failure modes do not occur.

3.1.3.3 Dimensions

Sizing of the specimens has been done by looking into the clamping method and comparing buckling loads with final compression failure using an analytical and finite element approach.

The analytical derivation of the buckling load can be derived from the methods by Kassapoglou, based on the approach by Whitney. This derivation determines the buckling load for a laminated plate for which the Kirchoff assumption remains true and plane stress can be assumed.

Sizing has also been performed using a finite element buckling load calculation in Abaqus using a 3D shell structure. From this approach, the first sets of unstable eigenmodes are determined from an eigenmode solver. Similarly to the analytical analysis, clamped boundary conditions are assumed on both sides of the specimen.

Using the two approaches as mentioned above with the sizing criterion, final specimen dimensioning was performed for laminates of both 8 and 24 layers. The most important influence is the effect of the free length. Initially a free length of 30mm was chosen. Later, however, to avoid buckling when the stiffness of the specimen reduces due to fatigue, the free length was reduced to 25mm with a width of 20mm.

3.1.3.4 End tabs

Considering end tabs, two important parameters should be considered: tab geometry and tabbing material. Many different tabbing materials are reported by authors such as steel, glass-epoxy and aluminum. Tapered tabs are often applied in tensile specimens to reduce stress concentrations. However, in compression, specimens will typically be very small and we need the largest possible surface area to analyze them. So, while tapered tabs might relieve stress concentrations, they do induce a boundary condition closer to hinged rather than clamped and therefore will result in a smaller free length to perform measurements upon.

From both quasi-static and fatigue tests, it can be concluded that specimens with **aluminum tabs** outperform the design with steel tabs, where failure occurs sooner and initiates in the stress concentration zone. [29]

The adhesive used for the tabs bonding was Locktite® 480. It is a cyonacrilate room temperature curing black coloured epoxy adhesive paste of high strength and toughness. Performances can be enhanced by post-curing at elevated temperature. It is suitable for bonding a wide variety of metals, and especially designed for bonding composites.

3.1.3.5 Final design

From this test series, aluminum tabbed samples have proven to be a good design, with fracture occurring in the middle of the samples rather than the stress concentration regions. This results in higher strengths and fatigue lives due to a better stress distribution. Therefore the final sample design has aluminum tabs of 1-1.5 mm thick and 55 mm long for all specimens, with load introduced through shear loading, a width of 20 mm and a free length of 25 mm. The composite material used has 24 layers oriented in a single direction with a total thickness of 5.3-5.5 mm for all specimens. The final design is shown below in **Figure 3.6**.

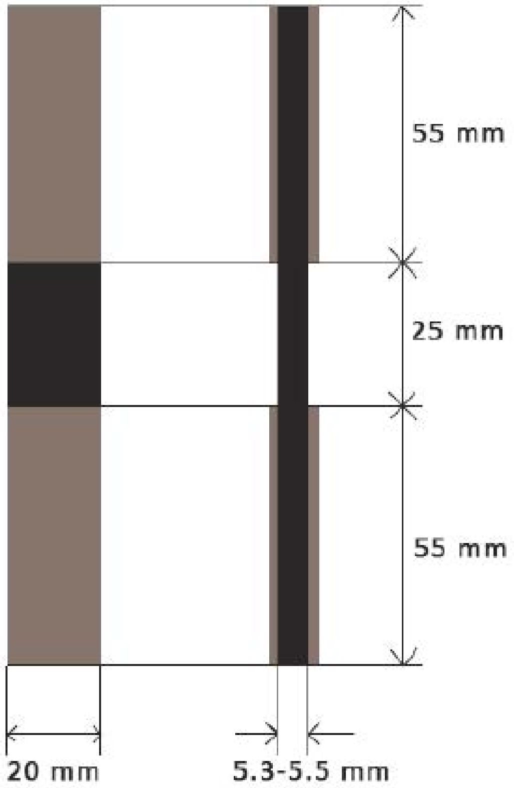

Figure 3.6: *Final specimen dimensions [29]*

3.1.4 Test results

A total of 15 static tests until failure have been performed, mainly to assess the ultimate compressive strengths of both lay-ups. A fatigue test program was performed on the woven carbon-epoxy material. The idea behind it is to capture relevant characteristics regarding C-C and T-C fatigue.

With regards to R-ratio, the experiments have been limited to 2 values. For C-C loading, the critical case to consider is a full loading/unloading cycle of the structure. The load is not returned completely to 0 but rather to a value of 10% of the maximum compressive load. This corresponds to R = 10. To characterize T-C loading, the typical method is to use fully reversed loading (R = -1), which is frequently encountered in literature as well.

3.1.4.1 *Quasi-static tests*

Uniaxial loading of a $[\#(0/90)]_{24}$ lay-up can be expected to be fiber-dominated. Therefore, strain rate dependence can be expected to be negligible for both strength and stiffness, with final failure occurring at low strains.

For a $[\#(\pm45)]_{24}$ lay-up, where failure is matrix-dominated under uniaxial compression, the case is somewhat different. As can be expected, much larger strain until failure can be observed.

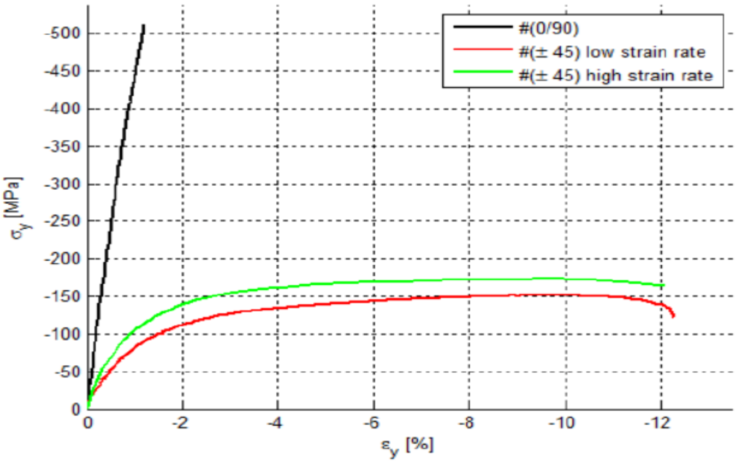

Figure 3.7: *Stress-strain behaviour for static tests [29]*

3.1.4.2 Fatigue tests

In **Figure 3.8** are shown the **S-N curves** for all the tests configurations.

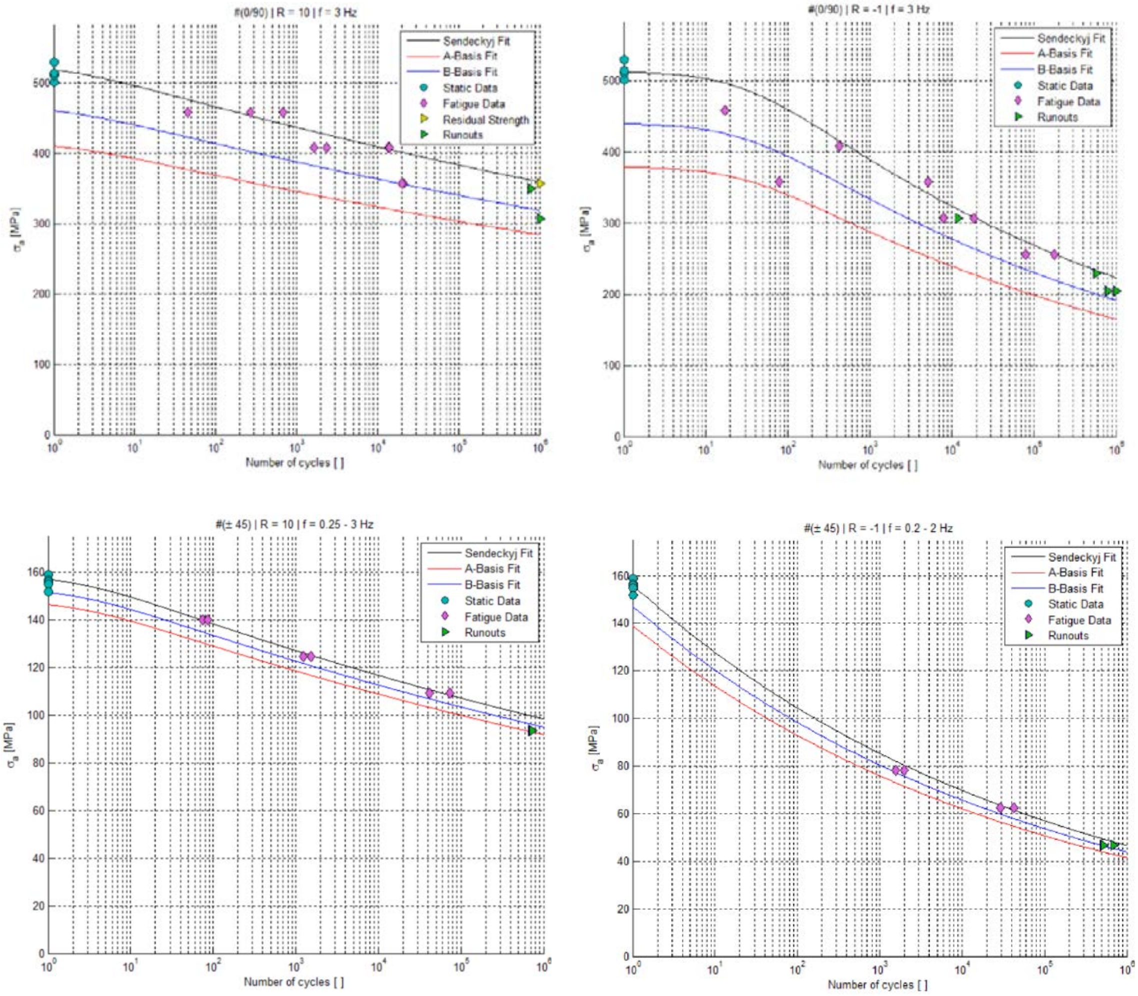

Figure 3.8*: S-N curves for $[\#(0/90)]_{24}$ with R=10 above left, $[\#(0/90)]_{24}$ with R=-1 above right, $[\#(+-45)]_{24}$ with R=10 below left, $[\#(+-45)]_{24}$ with R=-1 below right [29]*

For C-C loading of [#(0/90)]$_{24}$ laminates, in general, little hysteresis can be observed, both for high and low cycle patterns. In terms of stiffness, the pattern seem to be that little changes can be observed until final failure occurs. For high cycle fatigue, stiffness is pretty much unchanged throughout fatigue life (see **Figure 3.9**).

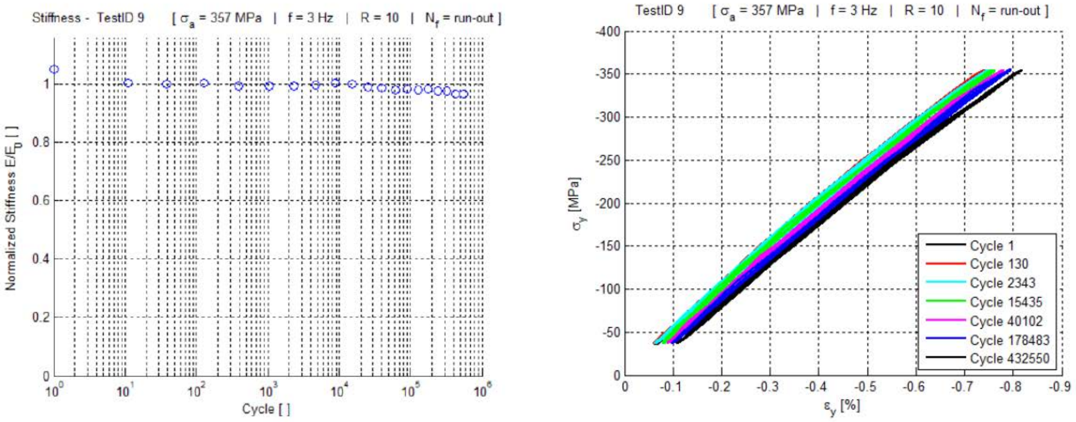

__Figure 3.9:__ [#(0/90)]$_{24}$ R = 10, Stiffness evolution on the left and stress-strain behaviour on the right [29]

T-C loading of [#(0/90)]$_{24}$ laminates typically shows little evolution in stiffness through time, little hysteresis and little permanent deformations for all loads applied. (see **Figure 3.10**)

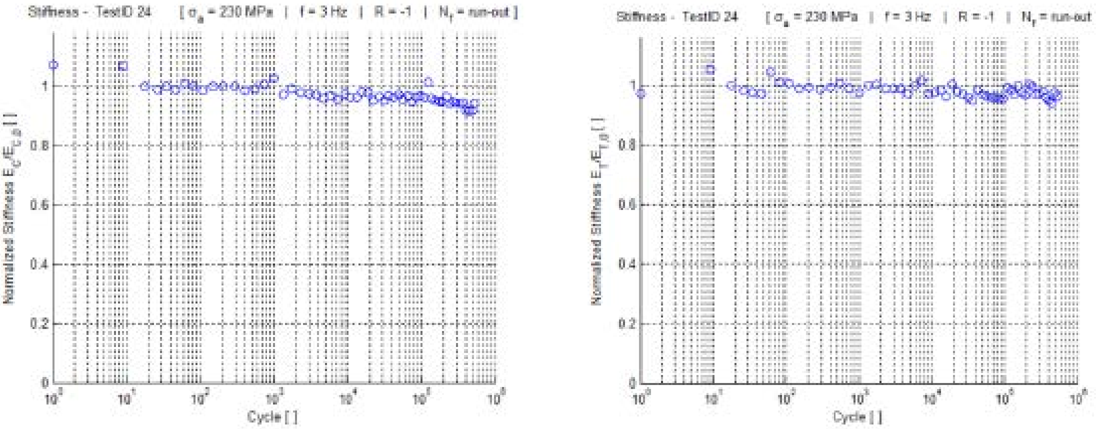

__Figure 3.10:__ [#(0/90)]$_{24}$ R = -1, Stiffness evolution on the left and stress-strain behaviour on the right [29]

As can be expected, laminates with only [#(±45)]$_{24}$ layers behave entirely different compared to [#(0/90)]$_{24}$ laminates. Comparing both laminates, it can be stated that for [#(±45)]$_{24}$ laminates, hysteresis is much more apparent, as well as stiffness evolution and permanent strain deformations. This subsection summarizes results for [#(±45)]$_{24}$ laminates tested at R = 10 (see **Figure 3.11**)

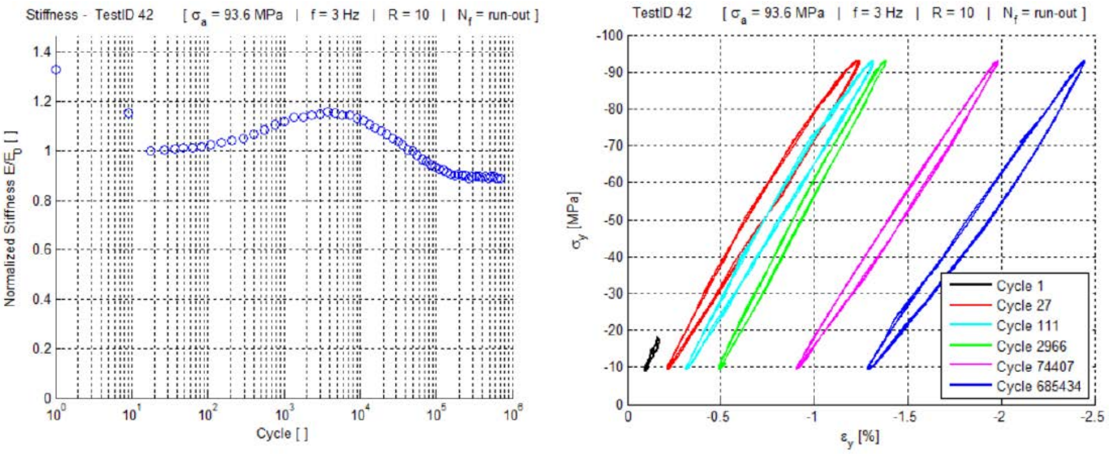

Figure 3.11*: Stiffness evolution [#(±45)]$_{24}$ R = 10 on the left and stress-strain behaviour on the right [29]*

The final load case is the one for [#(±45)]$_{24}$ laminates under fully reversed loading. It has already been substantiated that for this loading sequence, only the lower load cases have been tested (50, 40 and 30%) since the higher ones proved to be very difficult to test due to heating issues, are unlikely to be found in actual structures and had very short fatigue life. This loading/lay-up combination seems to be characterized by a considerably decreasing stiffness with large hysteresis cycles towards the end of life of a specimen (see **Figure 3.12**).

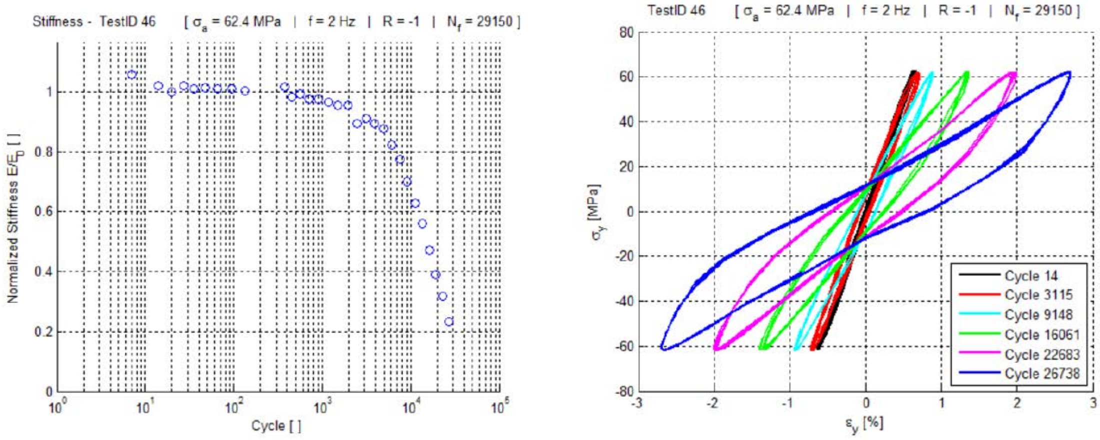

***Figure 3.12**: Stiffness evolution [#(±45)]$_{24}$ R = -1 on the left and stress-strain behaviour on the right [29]*

3.1.5 Issues encountered

In this paragraph will be focused on the issues encountered during the work:

- The **temperature** was monitored throughout every experiment. For [#(±45)]$_{24}$ laminates, the shearing motion of fibers resulted in heating of the material. To avoid this heating, the frequency was adapted for highly loaded tests, in combination with air cooling installed on the set-up. This kept the temperature within acceptable limits for most tests, except for high loading at R = -1.
- For [#(±45)]$_{24}$ loaded under C-C, an initial (shear) **stiffness increase** is observed. This is followed by a decrease in (shear) stiffness which is steady but decreases in steepness. However, this test method fails to effectively show the effects near the end of life of a specimen. Permanent (shear) strain evolution and hysteresis are more significant when the applied loads are higher and therefore more in the plastic region of the static stress-strain curve.

3.1.6 Improvements to apply to further works

After recognizing the issues, the way to fix it will be exposed in this paragraph:

- In order to solve the temperature issue, the fatigue test frequencies that caused high temperature on the specimen will be avoided. Only frequencies that in the past works didn't generate high temperature on the samples will be used. An example of some test with temperature issue is shown in **Figure 3.13**, with a [#(±45)]$_{24}$ loaded under C-C (R = 10).
- The stiffness increase during the fatigue life is false and not representative of the real fatigue behaviour of the stiffness. The reason for the stiffness increase during a fatigue test for [#(±45)]$_{24}$ loaded under C-C is the tabs debonding. The progressive debonding of the tabs during the test increase the free length of the sample. Increasing the free length, the tension field becomes more uniform and the stiffness should increase to the true value.

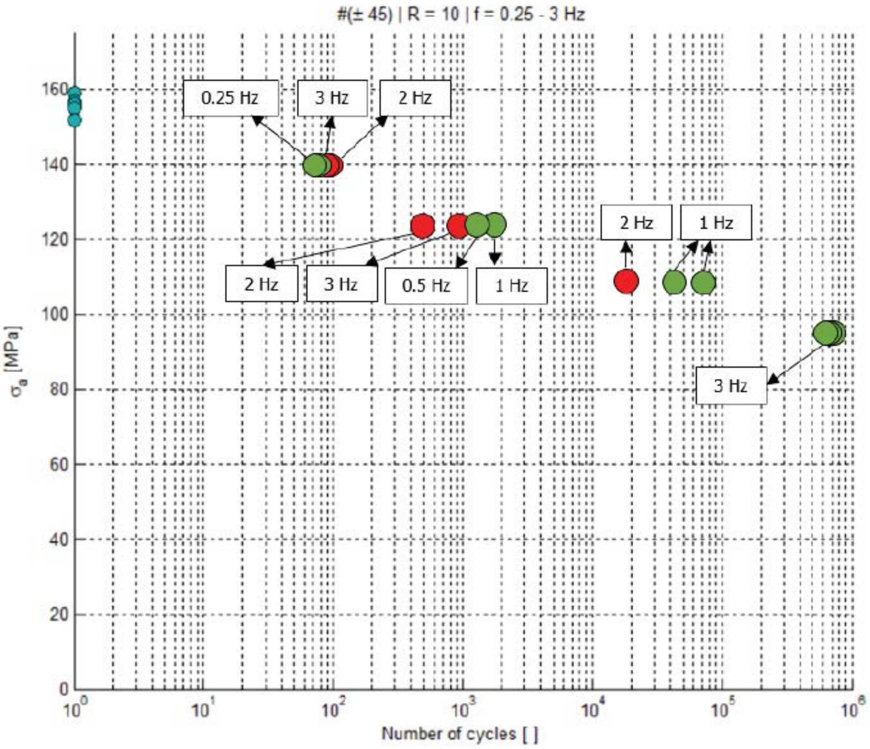

***Figure 3.13**: data points in case of [#(±45)]$_{24}$ loaded under C-C (R = 10). Frequencies of 2 and 3 Hz for this configuration will be avoided due to specimen overheating [29]*

3.2 “The effect of partially debonded tabs on the compressive stress-strain curve of angle-ply laminates” Pablo H. Jimenez [30]

3.2.1 Objectives

The objective of this research is to generate reliable **static test data for unidirectional CFRPs loaded in compression**. This work is a continuation of S. Walraet work: “C-C and T-C fatigue of woven carbon epoxy composites”. The first objective of this work is to solve the issues found by S. Walraet during his work and continue the study of fatigue behaviour of UD CFRP under compression load.

The aim is to keep track of the evolution of parameters like:

- Stiffness
- Poisson’s ratio
- Permanent (shear) strain

3.2.2 Set-up configuration

The set-up configuration used for this work was the same used by S. Walraet. Only few adroitness were adapted to improve the general set-up configuration of the test.

3.2.2.1 DIC cameras

The cameras used for this project were two Point Grey Grasshopper USB 3.0 cameras with a resolution of 2448 x 2048 (5 MP) and can reach up to 75 frames per second. A combination of two cameras has been used to obtain a 3D image, capable of detecting out of plane motion.

3.2.2.2 Measurement system evaluation

The evaluation system used for this work was the same used by S. Walraet, with the only exception that for this purpose, not any fatigue test was executed. All the part of S. Walraet's study about the delay between DIC and the machine's analog inputs was omitted.

3.2.2.3 Post-processing and calculations software

The post-processing software used to sort the images from the cameras was a MatLab algorithm. To elaborate data, calculate and plot graphs, Microsoft Excel© is used.

3.2.3 Material and specimen design

In this section, the available material is presented, followed by the specimen geometry design. The starting point for the specimen design was based on S. Walraet's work, but with a new configuration for material and some improvements of the dimensions to improve the uniformity of the stress field. A new type of interphase between the material of the specimens and the aluminium tabs was developed in order to avoid the stiffness increase during fatigue life.

3.2.3.1 Material

The material under investigation for this master thesis is **unidirectional carbon-epoxy**. Many plates were available in 24 layers, with a stacking sequence of $[0/90]_{6S}$. The plates are produced by Mitsubishi Rayon Co., Ltd., one of the industrial partners involved in the M3 project. They are made using Pyrofil fibers denoted by TR361, with epoxy resin E250S, at a fibre volume content of 58%.

To obtain samples with $[+45/-45]_{6S}$ stacking sequence, it's necessary to cut the samples from the composite plate with an angle of 45°.

3.2.3.2 Specimen geometry

As it was for the previous work, for this too, the option to have short specimen clamped at both ends, was used to prevent buckling. It results in a restriction of a certain amount of Poisson contraction (or expansion) due to the clamping effects at the ends.

An Abaqus model was created to investigate buckling and the uniformity of the stress field. The results obtained from the F.E.M. model and the analytical ones were compared to obtain the optimal free length and width of the specimens.

A new type of specimen geometry was introduced to prevent debonding of the tabs during the fatigue life. This type of specimen has a Teflon tape between the composite and the tab which reduces the bond surface. However, the gauge length is increased below the tabs which allows a non uniform stress distribution. Many tests were done on that new geometry to determine the optimal type of tape, the debonded length and the thickness of the tape. [30]

3.2.3.3 Dimensions

Sizing of the specimens has been done by looking into the clamping method and comparing buckling loads with final compression failure using an analytical and finite element approach. Sizing has also been performed using a finite element buckling load calculation in Abaqus.

Using the analytical and the F.E.M. approaches as mentioned above with the sizing criterion, final specimen dimensioning was performed for laminates with 24 layers. The most important influence is the effect of the free length. It was chosen a free length of 25mm, and a width of 20mm and was modified into 17 mm because Abaqus showed that a narrower sample would have a more uniform stress field.

3.2.3.4 End tabs

As well as for the previous work, aluminum tabs with a length of 55mm and a width of 17mm are used. This type of tabs ensures a good load transfer between the clamps and the composite.

The adhesive used for the tabs bonding has been ARALDITE® AW4858 mixed with a hardener. It's a two-component room temperature curing black coloured epoxy adhesive paste of high strength and toughness. Performances can be enhanced by post-curing at elevated temperature. It is suitable for bonding a wide variety of metals, and especially designed for bonding composites.

3.2.3.5 Final design

The final sample design has aluminum tabs of 1-1.5 mm thick and 55 mm long for all specimens, with load introduced through shear loading, a width of 17 mm and a free length of 25 mm. The composite material used has 24 layers oriented in a single direction with a total thickness of 5.3-5.5 mm for all specimens. The two types of specimens, the completely bonded (B type) and the partially bonded (D type) are shown in **Figure 3.14** below.

For the D-type, Teflon© inserts below the tabs surface up to a distance of 70 mm.

***Figure 3.14**: Final design and dimensions of B and D type specimens. Dimensions of tabs and coupon are not drawn to scale [30]*

3.2.4 Test results

The stress field of the B and D types of specimens have been compared to see which one can generate a more uniform strain field. The Abaqus analysis and the results obtained from the DIC correlated solution are compared on the following **Figure 3.15** and **Figure 3.16**.

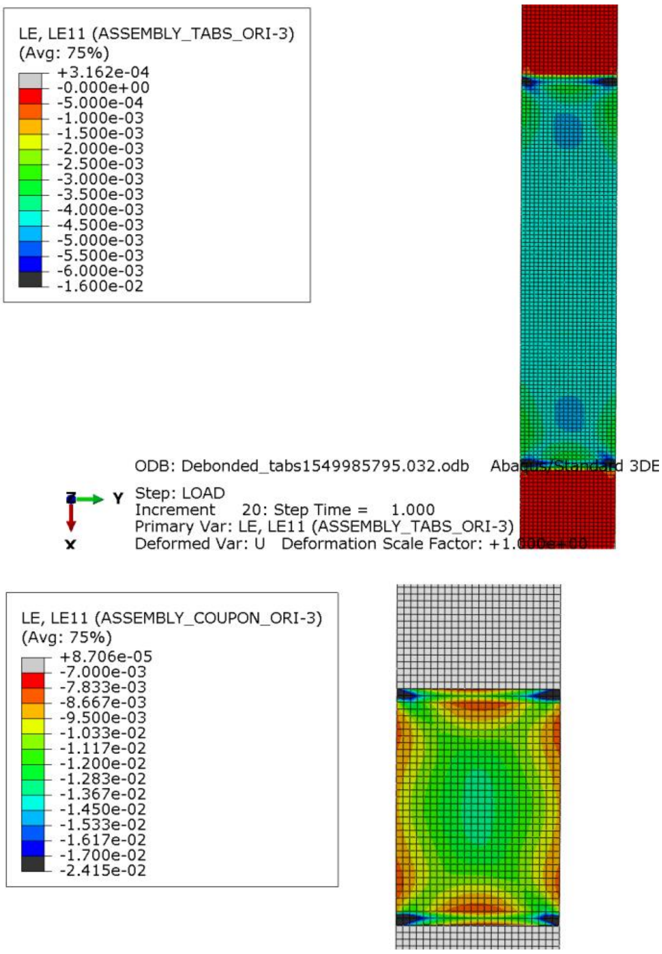

***Figure 3.15**: ε_{xx} Strain field comparison between B (below) and D (above) type specimen analysed on Abaqus [30]*

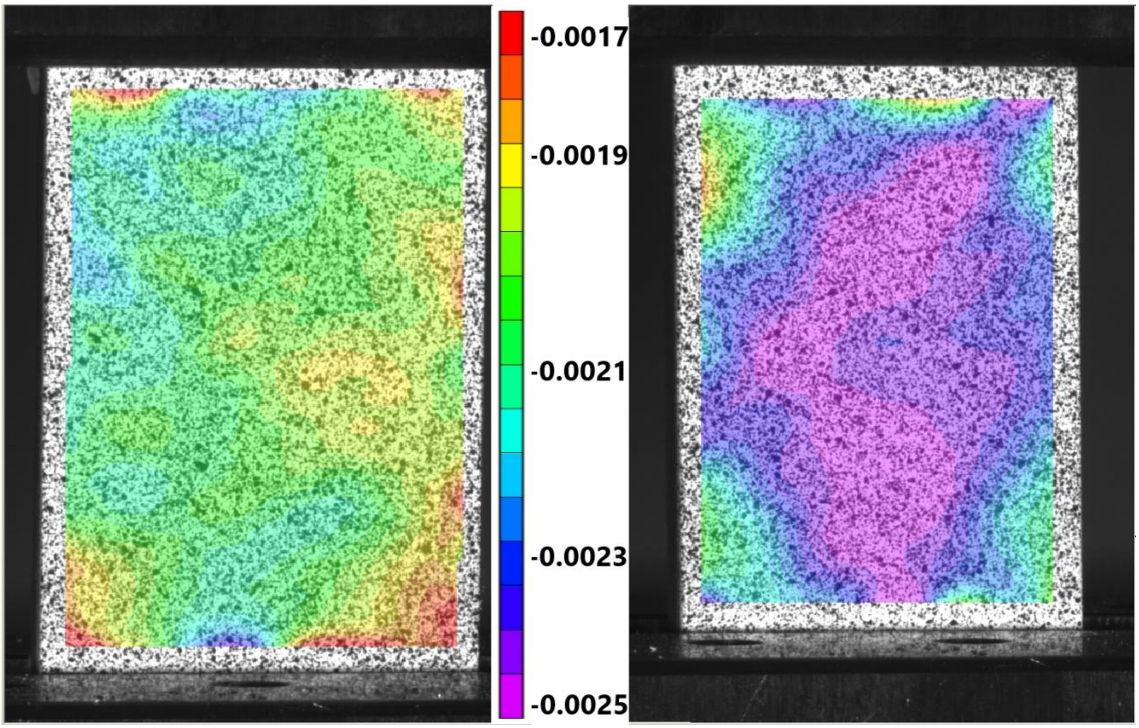

***Figure 3.16**: ε_{xx} Strain field comparison between D (left) and B (right) type specimen obtained at 30 MPa with Vic3D software [30]*

It’s clearly visible from **Figure 3.15** and **Figure 3.16**, that the strain field on the D type specimen is more uniform compared to the B type.

The stress-strain plot obtained from the static tests of the B and D type specimen is shown in **Figure 3.17**. The initial slope of the stress-strain curve is higher for the D type. It can be seen the initial stiffness of the D type is higher than the B type and it will be subsequently investigated. The trend of the curves is similar and they end with similar values of UCS (Ultimate compressive strength). As shown in **Figure 3.18**.

The only exception is B1 that has a different behaviour, more similar to the D type at the beginning.

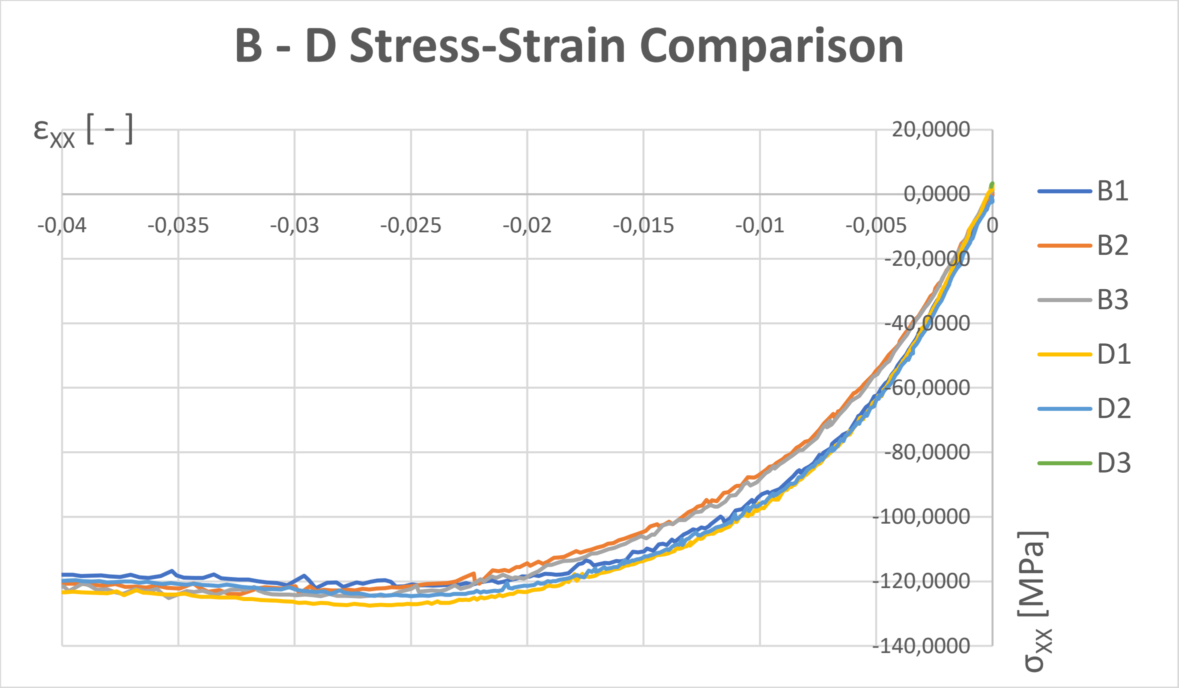

***Figure 3.17**: Stress-Strain curves comparison for B and D type specimens [30]*

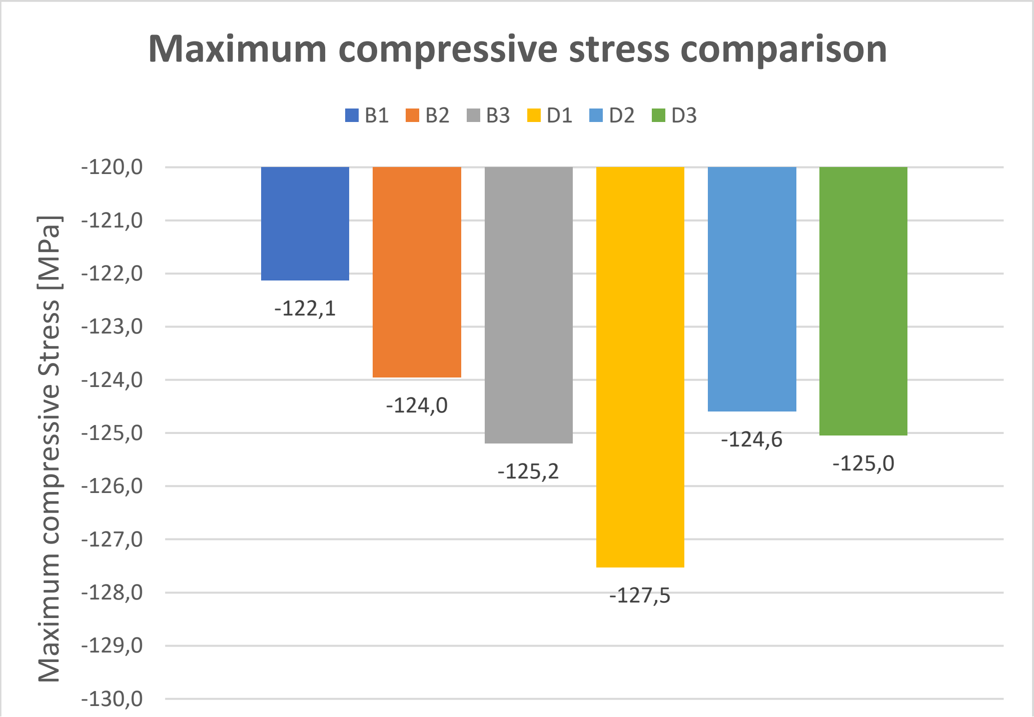

***Figure 3.18**: Maximum compressive stress comparison between B and D type [30]*

The initial stiffness of the B and D type specimens has been compared. According to ASTM D 3410 [44], the modulus of elasticity is defined as follows:

$$E^{chord} = \Delta\sigma / \Delta\varepsilon$$

where:

E^{chord} = tensile chord modulus of elasticity [GPa];

$\Delta\sigma$ = tensile stress range

$\Delta\varepsilon$ = strain range

The normative also gives indication for the strain range on where the stiffness should be calculated: 0,001 and 0,003 of absolute strain. To improve the reliability of the result, a linear regression has been applied on the datapoints in this interval.

According to ASTM D 3410 [44], the results of the initial stiffness of the samples are presented in **Figure 3.19** below:

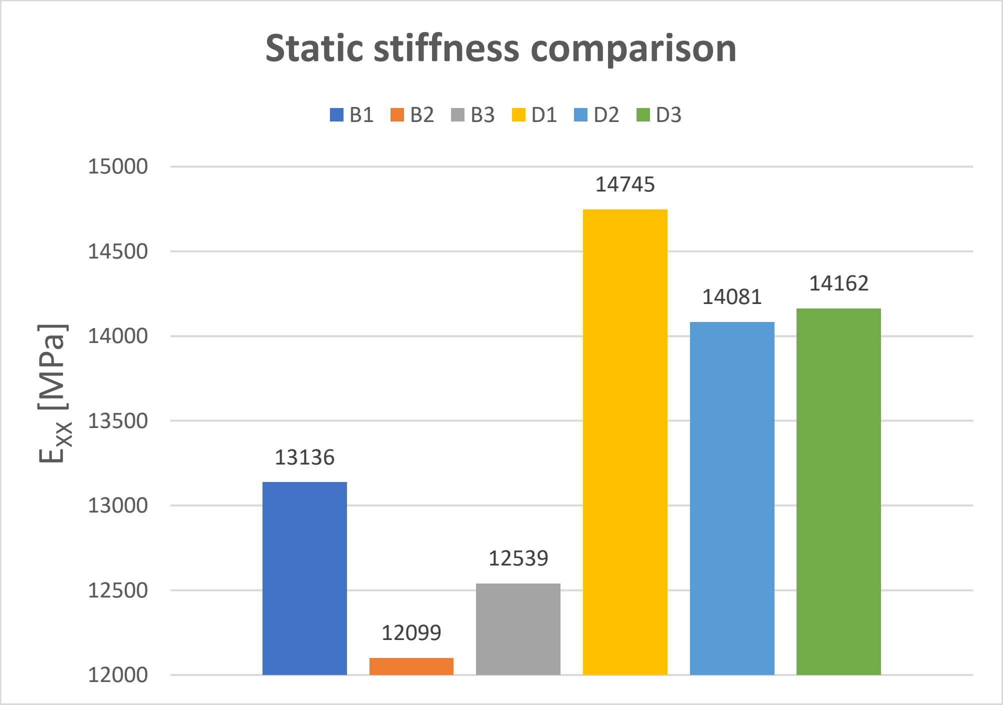

***Figure 3.19**: Stiffness comparison evaluated from static tests [30]*

As can be seen from the figure, the average stiffness for D type is 14.3 GPa while the average stiffness for the B type is 12.6 GPa.

This difference of the initial stiffness is due to the more uniform stress field on the D-type samples.

3.2.5 Issues encountered

In this paragraph will be focused on the issues encountered during the work:

- **Issues during waterjet cutting** appear sometimes in form of delamination or low precision of the cut itself. This involves discarding some samples. An example is shown in **Figure 3.20**.

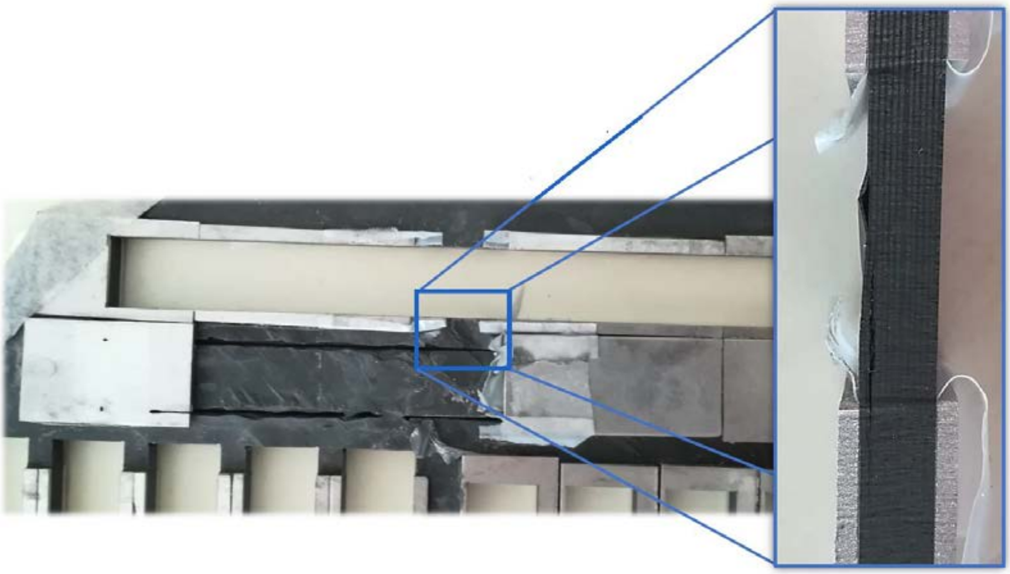

***Figure 3.20**: Manufacturing issues with waterjet cutting [30]*

- **Paint detachment issue:** Local buckling on the paint before coupon failing or buckling appear. It involves in non-correlation of the solution related to the zone characterized by paint detachment. It means that DIC does not correlate on these zones. An example of that damage is shown in **Figure 3.21**.

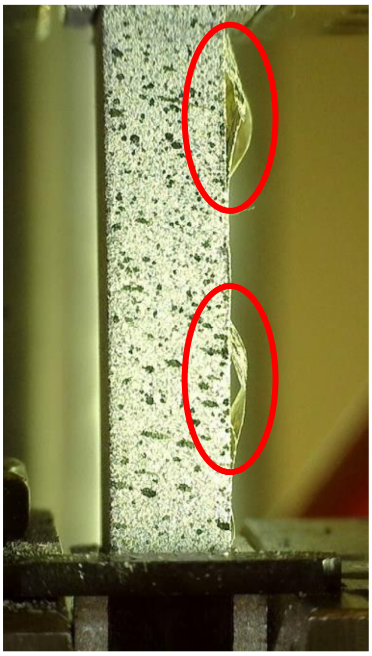

Figure 3.21: *Paint detachment issue [30]*

3.2.6 Improvements to apply to further works

After recognizing the issues, the way to fix it will be exposed in this paragraph:

- **Low manufacturing precision and the water-jet cut issue** has been solved using a pattern to help the tabs placing and bonding on the plate. The Teflon© tape has also been placed at the proper length, ensuring more control over final debond. An overview of the new cupons manufacturing technique is shown in **Figure 3.22**.

  The final result present:
    - no major deviation appreciated on tabs
    - good overall quality of the water-jet cut
    - Maximum deviation between the tabs of 1,5 mm

  - Teflon tape not coming out of the debond

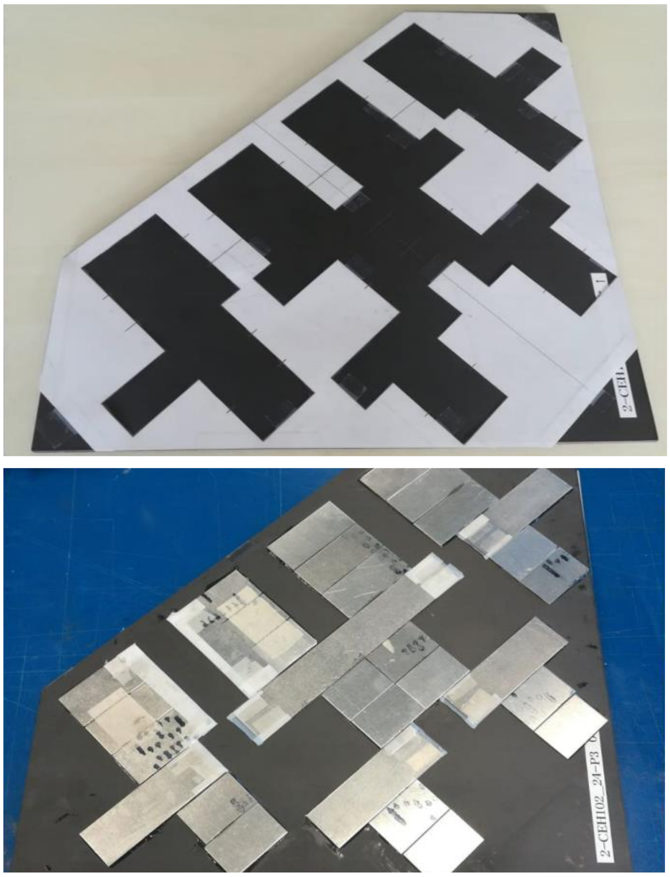

***Figure 3.22**: Overview of the new coupon's manufacturing technique [30]*

- **New Airbrush base paint** has provided an enormous improvement to the paint issue. It avoids completely the paint detachment from the sample. As it is shown in **Figure 3.23**, three samples were tested with both paints to check the paint differences.

  Another improvement was made to **refine the speckle pattern** of the airbrush base paint. It implies in a better correlation of the solutions from the DIC cameras and a significant noise reduction. The difference between the speckle pattern is shown in **Figure 3.24**.

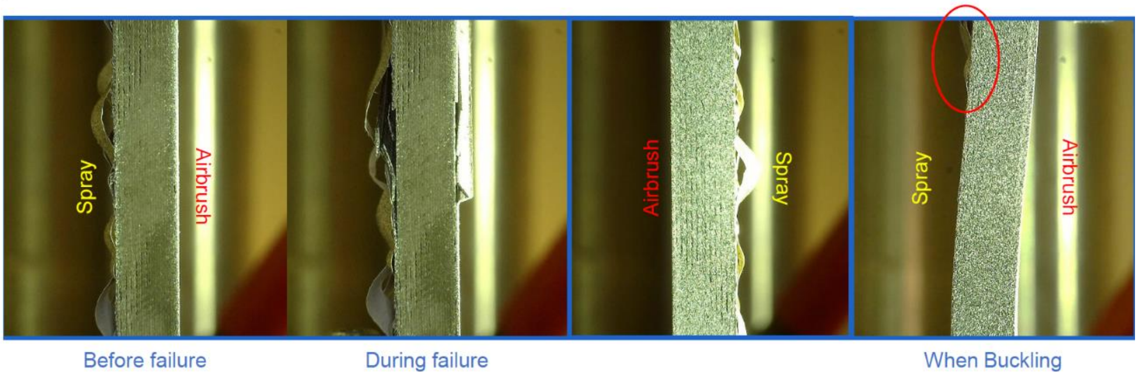

Figure 3.23: *Paint comparison between three specimens [30]*

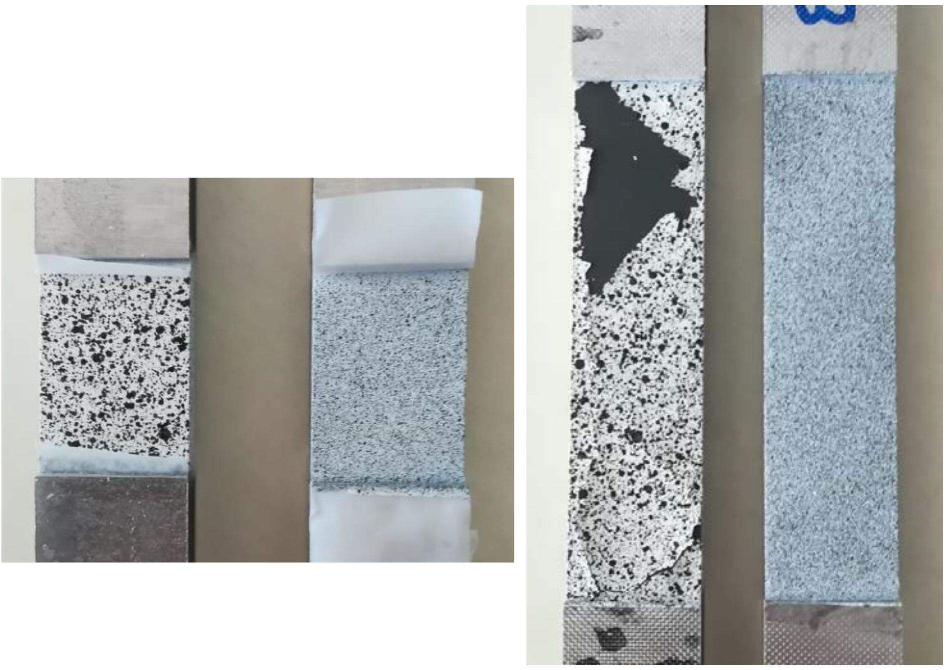

***Figure 3.24**: Different speckle pattern between the old painting and the new airbrush base paint (left and right) [30]*

4 EXPERIMENTAL SET-UP

This section is focused on the design of the experimental set-up for static and fatigue tests capable to capture relevant parameters and to obtain reliable results. The system should be able to:

- **Capture relevant data** reliably at intervals enough to characterize the fatigue behaviour
- **Perform fatigue experiments** reliably so that they can be representative for a material's fatigue behaviour under relatable loads.
- The system should be **simple in use and to set-up**
- This new system setup combined with the new specimens geometry should be a **new standard for testing composites under cyclic compressive loads**.

4.1 Measurement System set-up

In this chapter, all the components of the system and its relative settings will be exposed. It is exposed how the system acquires and elaborates data.

4.1.1 Machine

All experiments have been carried out on an Instron 8801 (100kN) servohydraulic fatigue testing system, suitable for both high and low cycle fatigue (visible in **Figure 4.1**). This system is capable of handling loads up to 100kN both in compression and in tension.

The 100kN dynacell fatigue load cell is mounted to the top actuator. Before the start of the test program, the accuracy (and repeatability error) of the load cell has been verified in accordance to Annex C of ISO 7500-1 by the Instron Calibration Laboratory. [29]

For compression testing, the machine is fitted with an alignment kit to ensure proper alignment of the clamps in all directions. It is fitted with hydraulic wedge grips rated for fatigue for which the pressure can be controlled if required. The test bench is controlled by a control PC fitted with fast-track software by Instron, with which you can control the system using force, strain (extensometer) or displacement control. Hydraulics can be controlled as well, and the machine has a specimen protection setting, to avoid damage to specimens before the start of a test. The machine can output force, displacement and extensometer strain as analog signals.

***Figure 4.1**: an Instron 8801 (100kN) servohydraulic fatigue testing system*

4.1.2 DIC cameras

The most important source of data acquisition for this project has been DIC.

Strain and displacement are critical parameters within engineering and construction projects. Digital Imaging Correlation (DIC) is a technique which may prove to be ideally suited for the study of crack propagation and material deformation in real-world applications, as it has the potential to become a cheap, yet simple accurate solution. [51]

DIC works by comparing digital photographs of a component or test piece at different stages of deformation. By tracking blocks of pixels, the system can measure surface displacement and build up full field 2D and 3D deformation vector fields and strain maps. For DIC to work effectively, the pixel blocks need to be random and unique with a range of contrast and intensity levels. [51]

Most measurements were performed using a set of Point Grey Grasshopper USB 3.0 cameras (GS3-U3-51S5M-C), shown in **Figure 4.2** below. These monochrome cameras have a resolution of 2448 x 2048 (5 MP) and can reach up to 75 FPS.

Figure 4.2: *Point Grey Grasshopper USB 3.0 cameras (GS3-U3-51S5M-C)*

The cameras recording mode, the exposure, the shutter time and other settings are set using FlyCap©.

DIC images are processed using Vic software by Correlated Solutions.

4.1.3 Temperature

The temperature during the fatigue life must be kept under control. High temperature can affect the results and the behaviour during the test.

A thermocouple has been placed on the back of the sample using Kapton tape, see **Figure 4.3**.

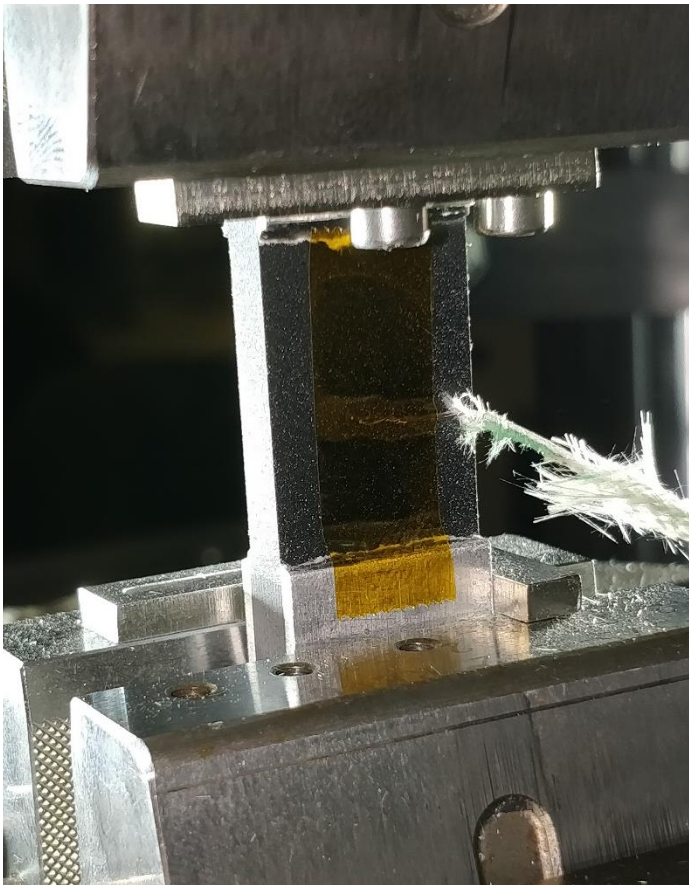

***Figure 4.3**: Thermocouple positioning*

The analogic signal from the thermocouple is acquired and converted into a digital signal by LabView.

4.1.4 Microscope

The optical microscope, often referred to as the light microscope, is a type of microscope that commonly uses visible light and a system of lenses to magnify images of small objects. A digital microscope is a variation of a traditional optical microscope that contains a tiny digital camera and is connected to a computer. The images seen through the microscope's eyepiece can be shown on the computer's monitor and saved on the hard drive as an image or as video.

During this project, a Keyence VHX-2000 digital microscope with possible magnification up to 2500x has been mostly used to capture delaminations, bonding surfaces, fibre cracking, tabs debonding, measure some dimensions. It also has the possibility to stich images and capture a 3D depth image. And it is shown in **Figure 4.4** below.

Figure 4.4: *Keyence VHX-2000 digital microscope*

4.1.5 Measurement system

The main requirement for this measurement system is that it should be able to capture all the analog input from the machine (load and displacement), the temperature from the thermocouple and, the triggered images from the DIC cameras,… The system should be easy to set-up, perfectly reliable and stand alone.

A LabView backbone system has been developed by S. Walraet for the study of “Compression-Compression and Tension-Compression Fatigue of Woven Carbon-Epoxy Composites” [29] and it can be used also for this project. The schema of this measurement system is shown in **Figure 4.5** below.

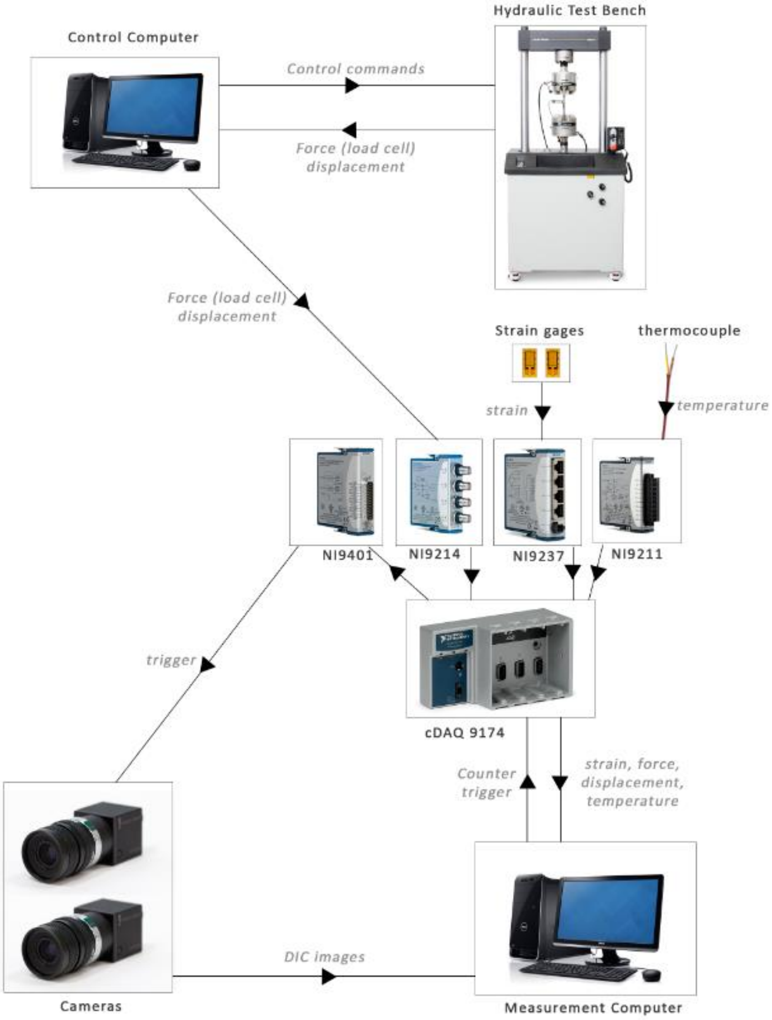

***Figure 4.5**: Labview triggered system [30]*

The real system setup is shown in **Figure 4.6** below. It is clearly visible the Instron 8801, the sample under test, the two DIC cameras and the LED lights.

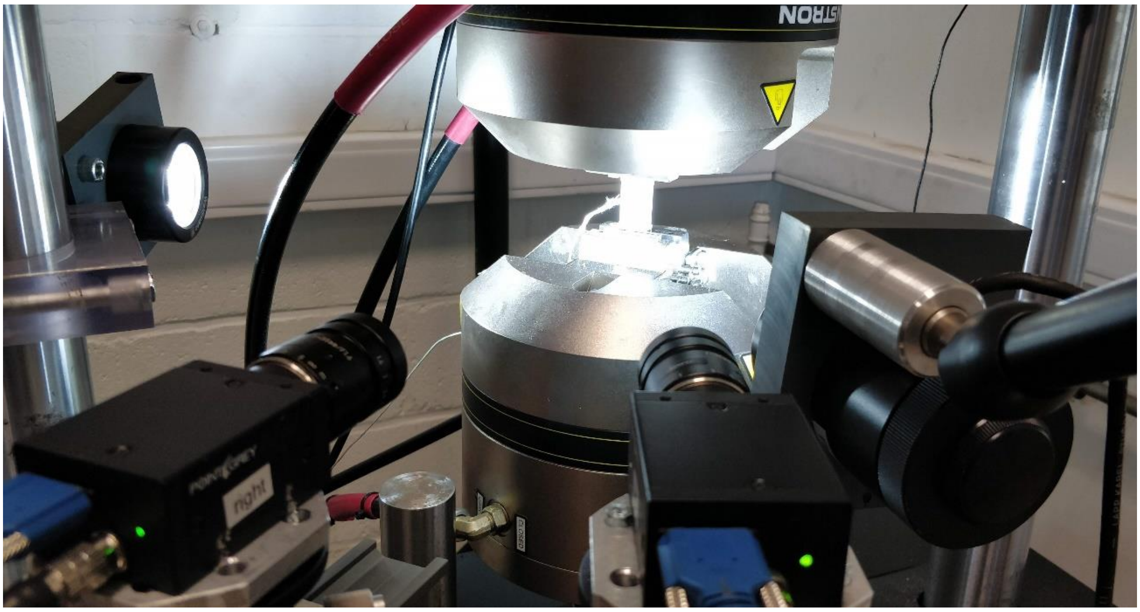

***Figure 4.6**: Real system set-up configuration*

The system has to be able to control and acquire data from both static and fatigue tests. Two different LabView modes allow different test settings and acquires different parameters.

The two recording modes are presented below:

4.1.5.1 Static test mode

This test mode should be able to capture images at a certain number of FPS (Frames per Second) and to set the delay in milliseconds between the trigger signal and the image acquisition. The data to be acquired are the images from the cameras, the analog input from the machine (load and displacement) and the time in which the images were recorded.

During the test it's possible to monitor the force amplitude, the displacement and the analog input from the extensometer (if connected).

The software interface is shown in **Figure 4.7** below.

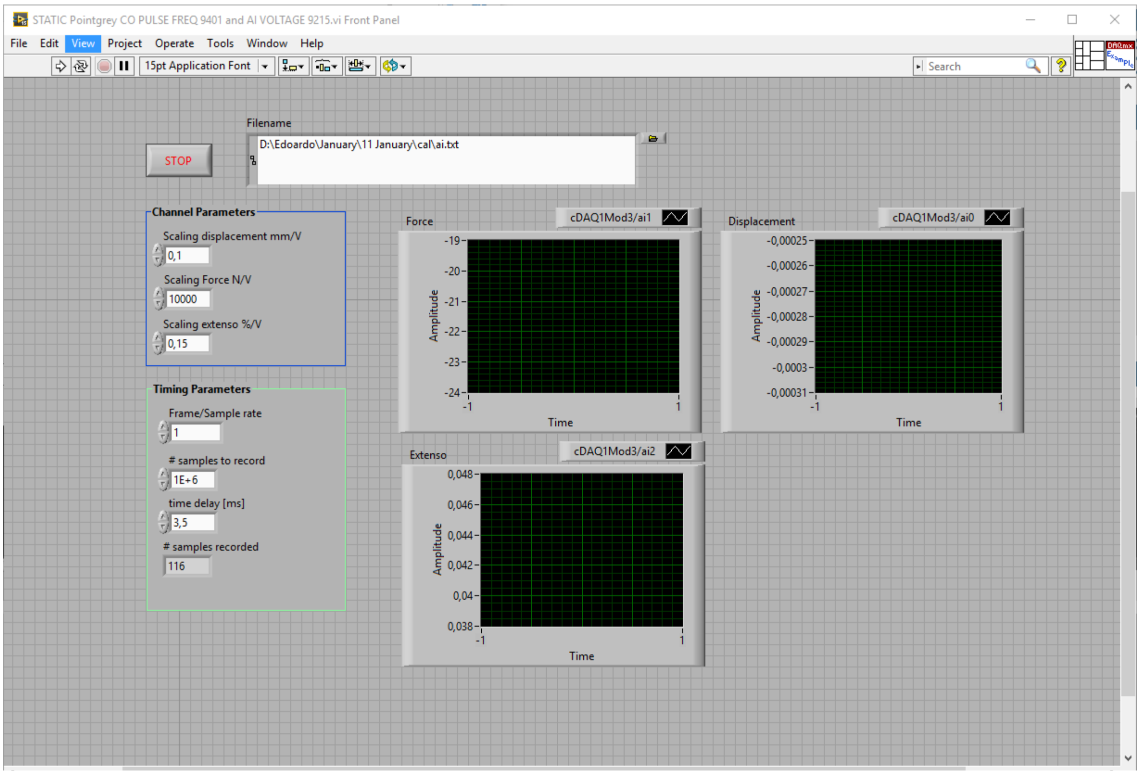

Filename: D:\Edoardo\January\11 January\cal\ai.txt

Scaling displacement mm/V: 0,1

Scaling Force N/V: 10000

Scaling extenso %/V: 0,15

Frame/Sample rate: 1

samples to record: 1E+6

time delay [ms]: 3,5

samples recorded: 116

***Figure 4.7**: LabView static mode interface*

4.1.5.2 Fatigue test mode

This test mode is more advanced compared to the static test mode. It should be able to:

- capture images at a certain number of FPS (Frames per Second)
- acquire the exact number of cycle to the correspondent data recorded
- set the number of cycles to be recorded for each measurement interval
- set the delay in millisecond between the trigger signal and the image acquisition
- set every how many cycles the measurement should be take

The data to be acquired are:

- the images from the cameras
- the analog input from the machine (load and displacement)
- the time in which the images were recorded
- the temperature measured by the thermocouple

During the test it is possible to monitor the force amplitude, the displacement, the temperature and the analog input from the extensometer (if connected).

The software interface is shown in **Figure 4.8** below.

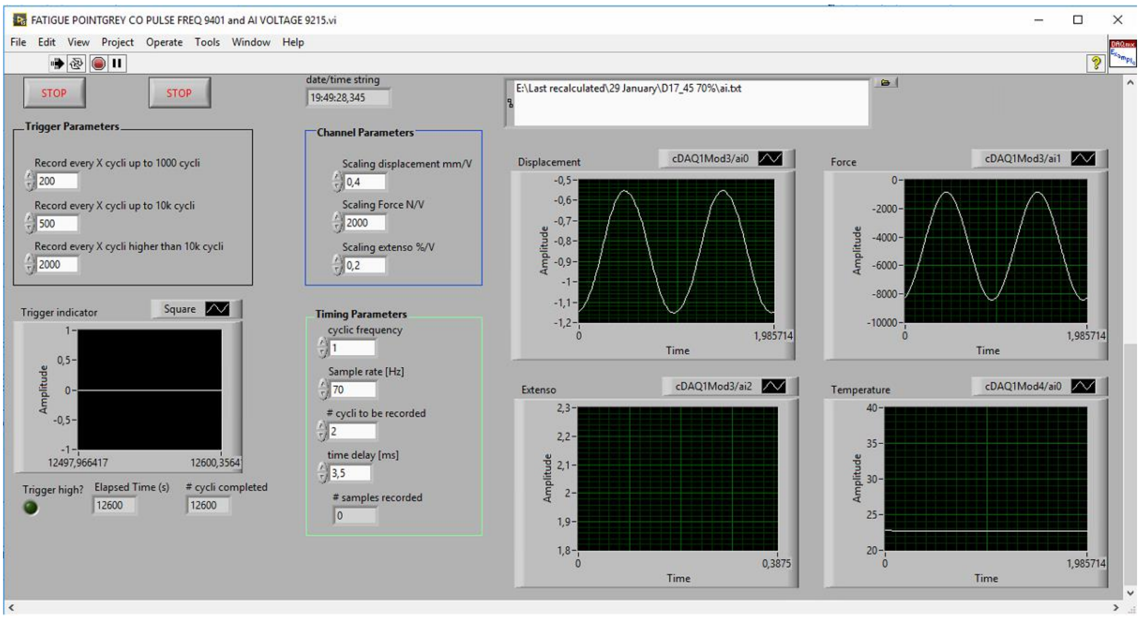

FATIGUE POINTGREY CO PULSE FREQ 9401 and AI VOLTAGE 9215.vi

date/time string
19:49:28,345

E:\Last recalculated\29 January\D17_45 70%\ai.txt

Trigger Parameters

Record every X cycli up to 1000 cycli
200

Record every X cycli up to 10k cycli
500

Record every X cycli higher than 10k cycli
2000

Channel Parameters

Scaling displacement mm/V
0,4

Scaling Force N/V
2000

Scaling extenso %/V
0,2

Timing Parameters

cyclic frequency
1

Sample rate [Hz]
70

cycli to be recorded
2

time delay [ms]
3,5

samples recorded
0

Trigger high?

Elapsed Time (s)
12600

cycli completed
12600

***Figure 4.8**: LabView fatigue mode interface*

4.2 Material and specimen design

In this section, the available material is presented, followed by the specimen geometry design. The starting point for the specimen design was based on S. Walraet's work [29] followed by the improvements developed by P. Jimenez [30] to increase the uniformity of the stress field and it is explained respectively in 3.1.3.2 and 3.2.3.2.

4.2.1 Material

The material under investigation for this master thesis is unidirectional carbon-epoxy and is the same used by P. H. Jimenez in "The effect of partially debonded tabs on the compressive stress-strain curve of angle-ply laminates" [30]. Many plates were available in 24 layers, with a stacking sequence of $[0/90]_{6S}$. The plates are produced by Mitsubishi Rayon Co., Ltd., one of the industrial partners involved in the M3 project. They are made using Pyrofil fibers denoted by TR361, with epoxy resin E250S, at a fibre volume content of 58%.

To obtain samples with $[+45/-45]_{6S}$ stacking sequence, it's necessary to cut the samples from the composite plate with an angle of 45°.

4.2.2 Specimen geometry and dimensions

As it was for the previous work, for this too, the option to have short specimen clamped at both ends, was used to prevent buckling.

The specimen design, the geometry, the dimensions and the end tabs has been studied and developed by P. H. Jimenez in "The effect of partially debonded tabs on the compressive stress-strain curve of angle-ply laminates" [30] (paragraph 3.2.3).

The new specimen geometry developed by P. H. Jimenez is shown in **Figure 4.9** below.

Figure 4.9: *Fully bonded (B) and partially debonded (D) design comparison [30]*

The dimensions of the two types of samples are:

- Length = 135 mm
- Width = 17 mm
- Thickness = 5,5 – 5,8 mm
- Free length B type = 25 mm
- Free length D type = 70 mm

4.2.3 End tabs

As well as for the previous work, aluminum tabs with a length of 55mm and a width of 17mm are used. This type of tabs ensures a good load transfer between the clamps and the composite.

The adhesive used for the tabs bonding has been ARALDITE® AW4858 mixed with a hardener.

The plates were cured at 40°C for 16 hours.

4.2.4 Specimen manufacturing

As explained in 4.2.1, the material is available in many plates produced by Mitsubishi Rayon Co., Ltd. The plates have 24 layers, with a stacking sequence of $[0/90]_{6S}$.

To obtain samples with $[+45/-45]_{6S}$ stacking sequence, it's necessary to cut the samples from the composite plate with an angle of 45°. To realize it, a nesting software called Powernest© has been used. This software optimizes the number of shapes that can be cutted from a plate or a sheet. Keeping the assigned distance between the shapes and the borders and optimizing the number of shapes that can be obtained. The input values assigned to the software are:

- Dimension of the plate= 330mm x 330mm
- Dimension of the sample= 135mm x 17 mm
- Distance between the samples = 7 mm
- Distance between samples and plate borders = 10mm

At the end of the analysis, shown in **Figure 4.10** below, 17 samples with $[+45/-45]_{6S}$ stacking sequence and 2 samples with $[0/90]_{6S}$. stacking sequence are obtained.

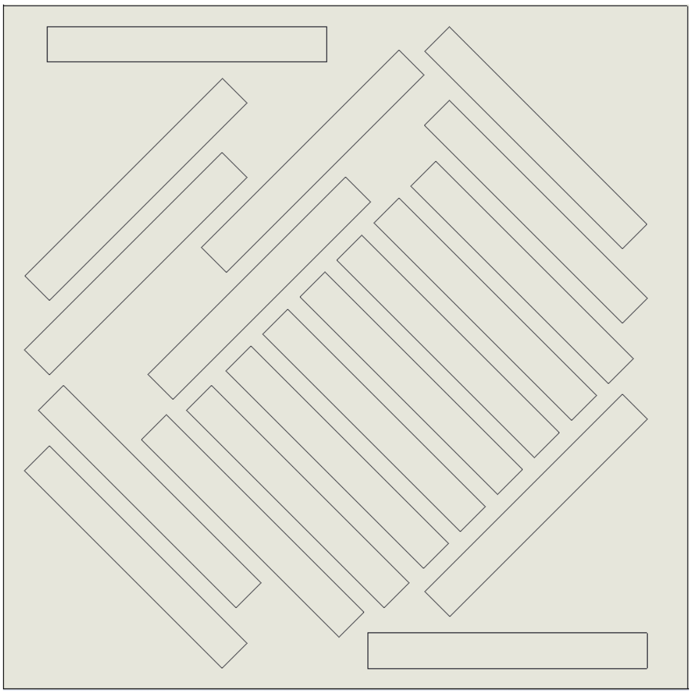

***Figure 4.10**: Nesting drawing of the plate*

It is also necessary to create a pattern for the aluminium tabs placing. A SolidWorks© drawing has been developed, starting from the sketch of the nesting. Many squares with the dimensions of the end tabs are placed at the end of the samples shapes.

The final drawing is shown in **Figure 4.11** and the printed pattern is shown in **Figure 4.12**.

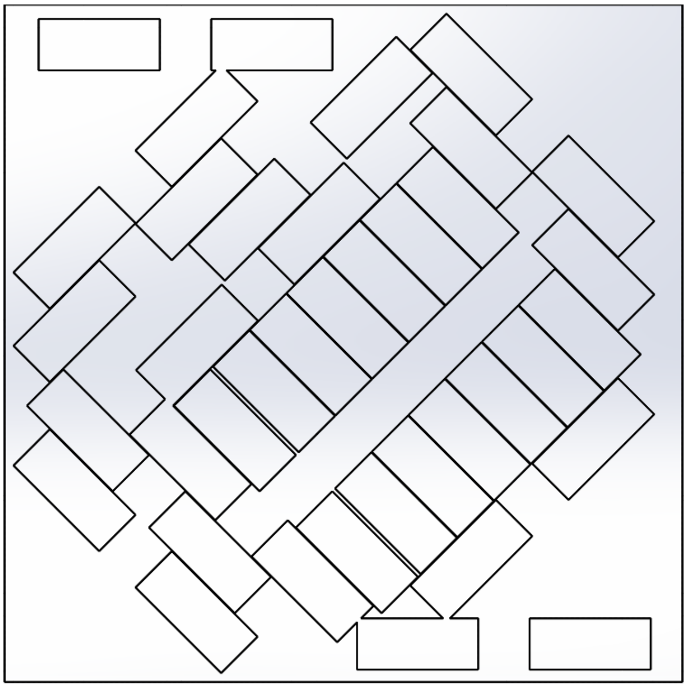

***Figure 4.11**: Drawing of tabs pattern (Solidworks©)*

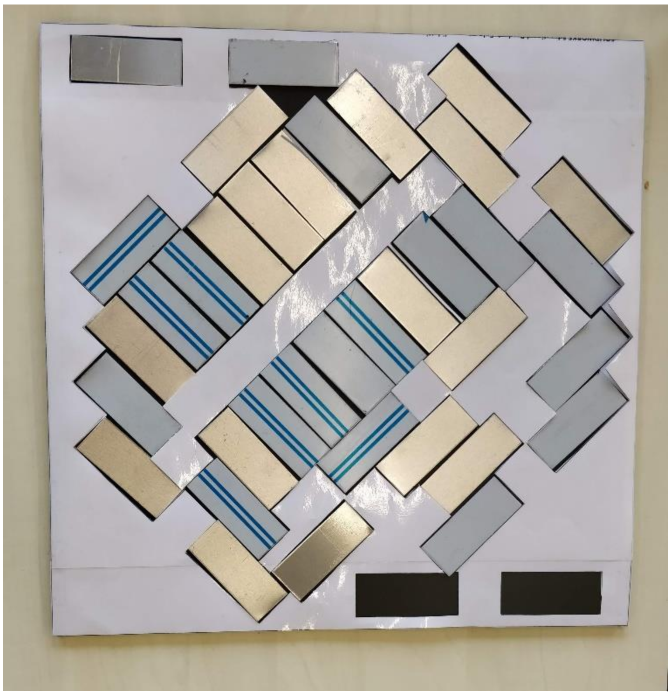

***Figure 4.12**: Printed tabs pattern*

Thanks to the tabs positioning pattern it is possible to glue the aluminium tabs on the composite plate, with a placing tolerance lower than 0,5 mm. Before the bonding application it is necessary to sand both the surfaces of the plate and the aluminium tabs in order to improve the adhesive strength. After the application and bonding of the tabs, to enhance the performance of the adhesive, a curing treatment has to be done in the oven at 40°C for 16 hours. The result before the preparation is shown in **Figure 4.13**

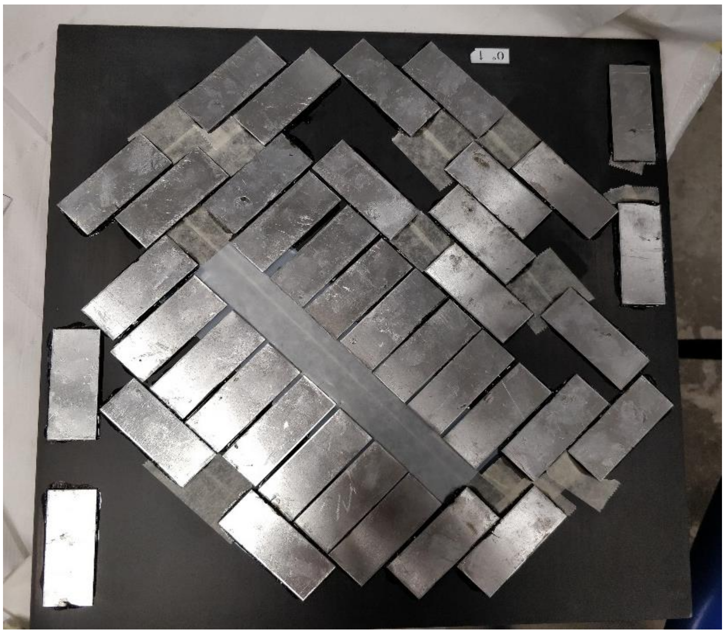

***Figure 4.13**: Plate preparation after the curing time*

After the curing the plates are cutted with water-jet cutting technique by the "Ontwerp- en productietechnologie" workshop center at Odisee.

For the first plate, some delaminations were present on the ends of the sample. This was due to the attack point of the waterjet being too close to the specimens shape. All the specimens have been checked to make sure no delaminations were in the gauge length. After that, no delaminations problem appears again.

After the waterjet-cut the samples can be painted for the DIC analysis and if it is needed to polish the sides.

The final result of the manufacturing process is shown in **Figure 4.14**.

Figure 4.14: *Final result of the manufacturing process*

4.3 Digital Image Correlation

Digital Image Correlation (DIC) is an optical-numerical measuring technique, which offers the possibility of determining complex displacement and deformation fields at the surface of objects under any kind of loading [53].

It is used in several fields of experimental solid mechanics, but its potential application to the characterization of composite reinforcements has not been fully investigated yet. DIC provides additional information on damage pattern (crack location and width) and composite substrate load transfer mechanism (effective bond length and local stress concentrations). It also offers the advantageous possibility of selecting several measurement points after the test, overcoming some drawbacks of traditional transducers. On the other hand, since only on the outer surface of the specimen is monitored, no information is directly available on the textile embedded in the matrix. The combination of DIC and traditional sensors in laboratory testing allows improving the understanding of the mechanical behaviour of composite reinforcements and the identification of their fundamental properties [54].

The advantages to use DIC to obtain the strain field of the samples, compared to the other techniques are:

- Full-field displacement data
- Contactless method applicable to arbitrary geometries
- Covers a wide range of loading conditions, describing deformation at the small strain level up to very high values of plastic deformation
- Relatively cheap, easy in setup and use
- High speed cameras
- Multi-camera system for up to 360 degree measurement around an object and simultaneous front and back side measurements
- Measurement area can be less than 1mm and up to several square meters

4.3.1 How it works

The DIC method is based on the correlation of the digital images taken during test execution. Each element of such matrix corresponds to a pixel representing one specific point of the specimen surface, and its value is based on its intensity (from black to white). To calculate the in-plane displacement of the surface of the specimen, a computational grid is defined on the picture or on a portion of it, named Region Of Interest (ROI). The pictures taken before and after deformation are correlated and the points of the grid in the ROI are matched, i.e., their position after deformation is identified as that associated to the peak of the correlation coefficient. A number of correlation criteria exist, which differ in the computational effort required in calculations and in robustness. The one suggested by recent works as the most robust and reliable is the zero-normalized sum of squared differences, since it is insensitive to illumination lighting noise. To improve the reliability of the correlation, not just two pixels but two subsets of pixels, centred at each point, are correlated to each other. Subsets may be either square or circular. The displacement of each point of the grid corresponds to the relative distance between its positions in the deformed image and in the undeformed one. The displacement of another point provides the deformation of the subset. The displacements and deformations of all the subsets defined in the ROI provide the deformation of the real specimen. DIC results are originally computed in pixels and then converted into millimetres. The pixel-to-millimetres conversion factor can be calculated from the focal length and the distance from the considered specimen surface to the optical sensor. Resolution and accuracy are associated with the resolution of the optical sensor installed in the camera. As a first approximation, the method provides measurements with the resolution of the size of one pixel. Finally, the displacement field directly obtained by this procedure is discrete (as displacements are provided at the nodes of the computational grid), and it is then interpolated with predefined shape functions.

The procedure is briefly schematized in **Figure 4.15**.

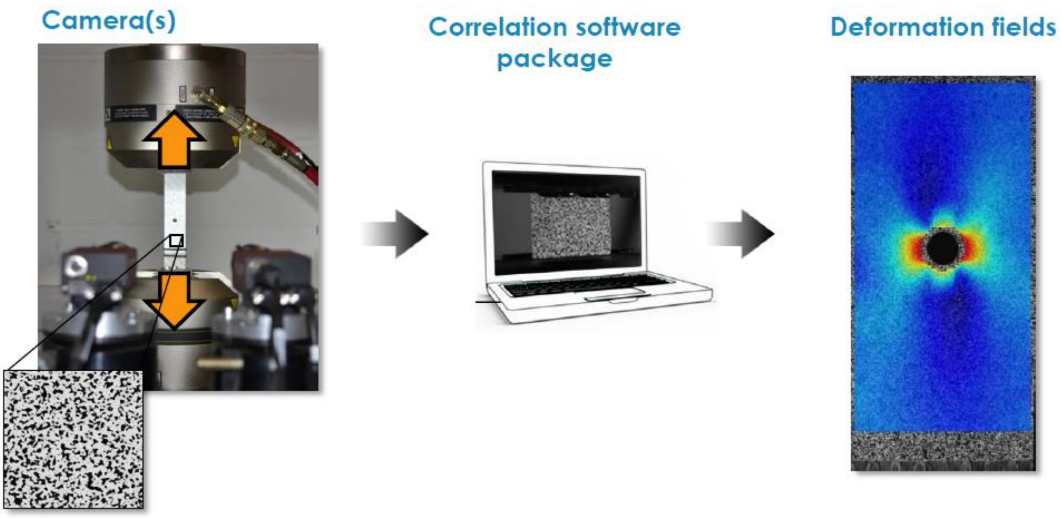

Figure 4.15: *Extensometry with DIC [53]*

4.3.1 Specimen preparation

The application of Digital Image Correlation needs particular care in the preparation of experimental setup. First, a speckle pattern, consisting of black dots, randomly distributed over a white background, needs to be realized on the specimen surface by means of spray or airbrush painting. An example is shown in **Figure 4.16**.The size of the spots in the speckle pattern influences the accuracy of the results, so a suitable balance needs to be identified based on specific setup conditions. If the surface of the specimen is particularly rough, its natural texture could ensure by itself sufficient contrast that no additional preparation is required. As an alternative, in order to measure the displacement of specific points, artificial markers can be placed on the specimen, which also provide information on real dimensions, useful to determine the pixel-to-millimetres conversion factor.

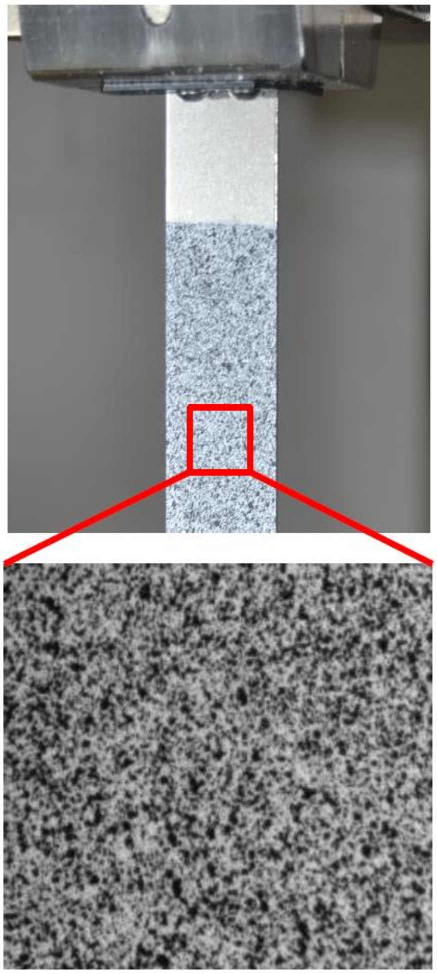

***Figure 4.16**: Speckle pattern painted on the sample*

4.3.2 Cameras and lights positioning - calibration

It is possible to recover the three-dimensional position of the true object points by using two cameras to record simultaneous image points of the same object. The two cameras can be placed to both look to the front of the sample (with a certain inclination angle between them). Or they can be placed to look one the front and one the side, depending on what are the interests of the test.

The camera should be horizontal, with a field of view a bit larger than the specimen's gauge length. The focus point should be the surface of the sample and the lights should provide a diffuse lighting of the specimen surface. The histogram of the pictures should cover at least half of the grey scale but avoiding saturation of the pixels.

Once the system (cameras and lights) are placed, the calibration process has to be executed using a special target. During calibration, the target is tilted and rotated into different orientations while images are acquired. The bundle adjustment calibration determines all of the intrinsic camera parameters (image center, scale parameters, image skew, distortion parameters) and the extrinsic parameters (pinhole location, orientation of each camera relative to target) and the orientation and position of the target during the calibration motion sequence. [55]

Figure 4.17 below shows a schematisation of the calibration procedure and the parameters to be determined for a stereo-vision system.

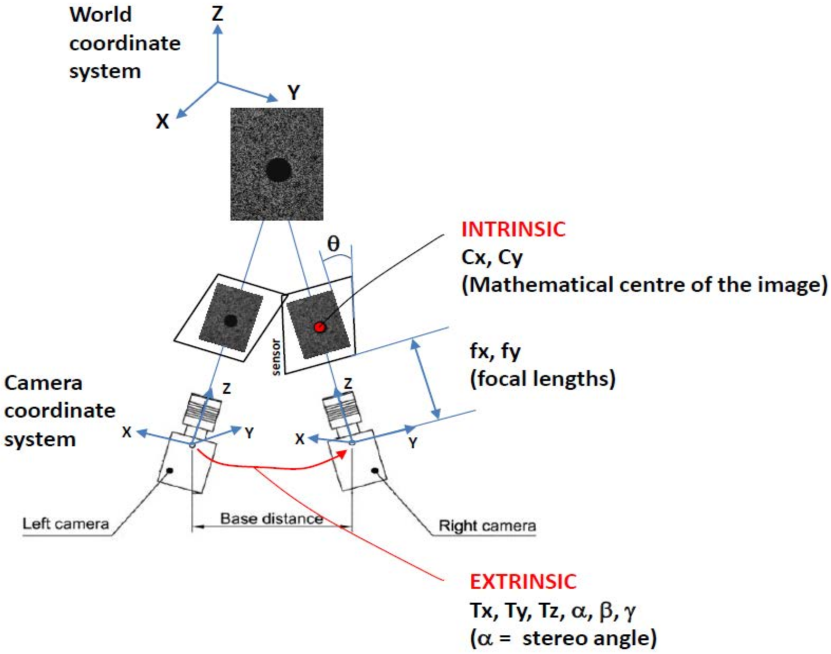

***Figure 4.17**: Schematisation of the calibration parameters to be determined*

4.3.3 Images sorting and post-processing

After the test the images needs to be sorted, changing their names in ascending order and adding a final 0 or 1 to distinguish the images captured by left or right camera. They should also be converted into a matrix. These operations are achieved by a MatLab© script and after this operation the images can be post-processed.

The software VIC-3D© is used to analyse all the images acquired by both calibrated system and perform image matching to quantify 3D displacement fields using the stereovision system. All the displacements from the front surface are expressed in the same common global coordinate system, with all displacement components defined in the same system. Calculating the displacement derivatives and partial derivatives from a quadratic polynomial approximation it is possible to calculate the surface deformation field.

In order to analyse the surface of the sample, the Region of Interest (ROI) should be chosen, generally trying to avoid the edges of the sample. The subsets dimension has to be set with a correct dimension to take in account the movement and the deformation of the original subsets.

Vic-3D© can now calculate the solution analysing the ROI, see **Figure 4.18**.

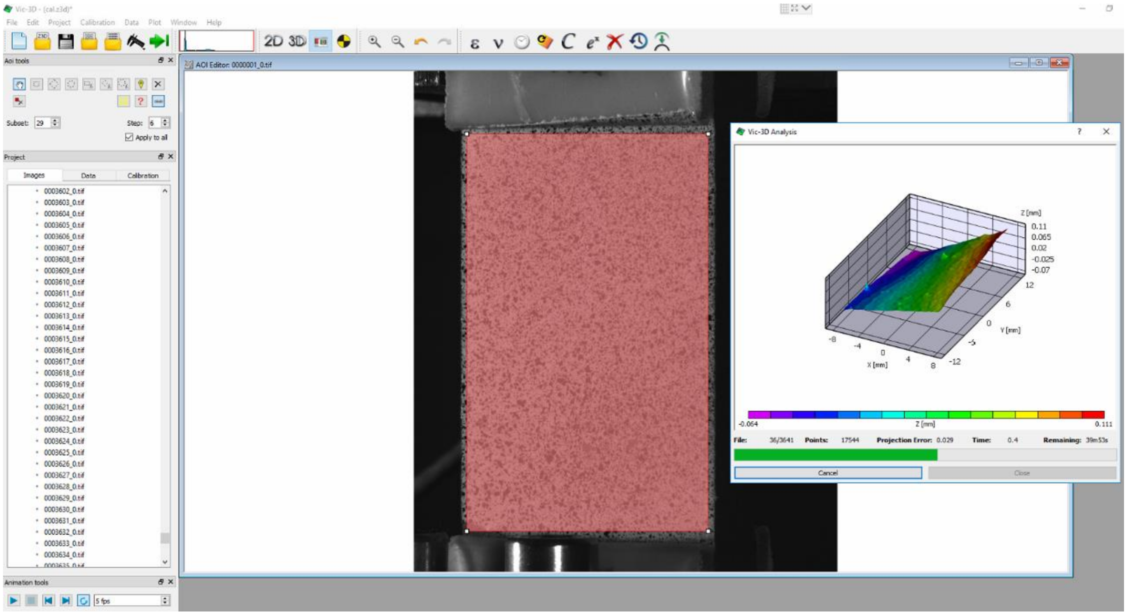

Subset: 29
Step: 6
☑ Apply to all

File: 36/3641 Points: 17544 Projection Error: 0.029 Time: 0.4 Remaining: 39m53s

***Figure 4.18**: Vic-3D© analysing the Region of Interest defined by the user*

When the analysis is be completed, results can be virtually plotted on the surface of the sample. For example, **Figure 4.19** shows the vertical strain field on the gauge length of the specimen.

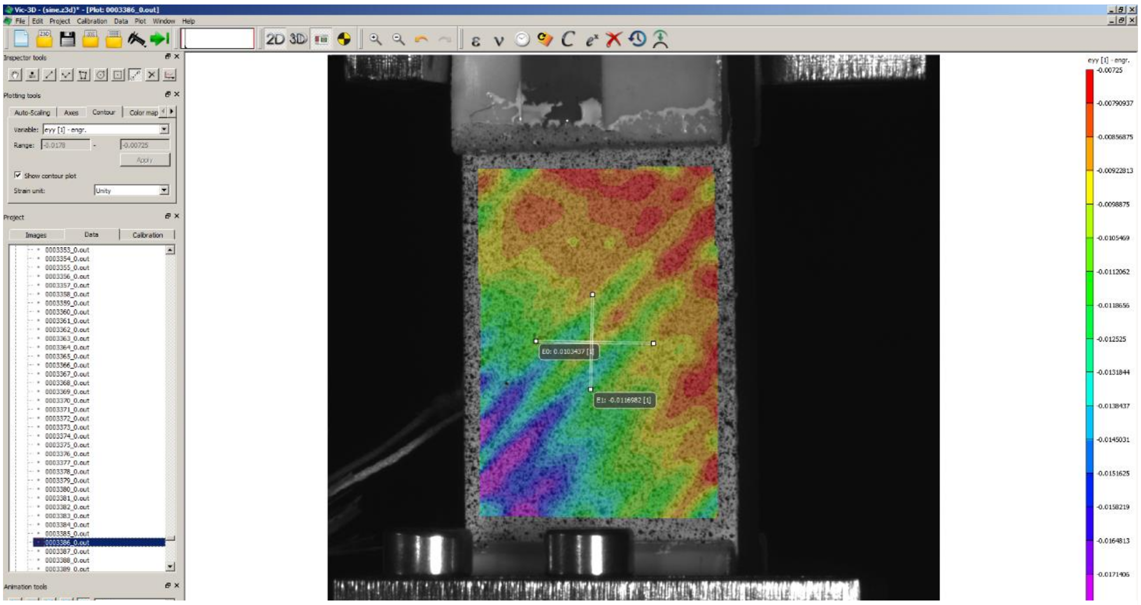

Variable: eyy [1] - engr.

Range: -0.0178 - -0.00725

☑ Show contour plot

Strain unit: Unity

E0: 0.0103437 [1]

E1: -0.0116982 [1]

__Figure 4.19__: Display of results on Vic-3D©

The results from the DIC analysis done with Vic-3D© can be exported using a comma-separated values file (.csv) which can be converted into an Excel© worksheet.

4.3.4 Rigid body motion

Usually, before starting a real test, a rigid body motion should be executed in order to :

- ensure the correlation of the speckle on the sample surface
- calculate the displacement error between the machine and the DIC cameras
- calculate the delay between the signals from the machines and the trigger signal to the cameras
- ensure that the machine is working properly

All these operations should be executed before the test, avoiding any damage to the sample. Rigid body motion of the specimen is obtained clamping only the lower end of the sample and starting the machine, setting it to make a displacement-controlled movement that can be linear or sinusoidal.

4.3.4.1 Static

The static rigid body motion is obtained by moving the sample at a constant speed from a point to another point. The output data of the displacement from the machine and the DIC are compared to see what is the error between this two measures.

An example of the results of a static rigid body motion is shown in **Figure 4.20**, where the average error between the two measures is 1,58%. To reduce the error from the DIC analysis it is necessary to have calibrated correlation speckles with exact distance between the dots, or at least set the exact distance between the dots during the calibration procedure. The calibration speckle has to be measured under the microscope to check the exact offset between the dots, as shown in **Figure 4.21**.

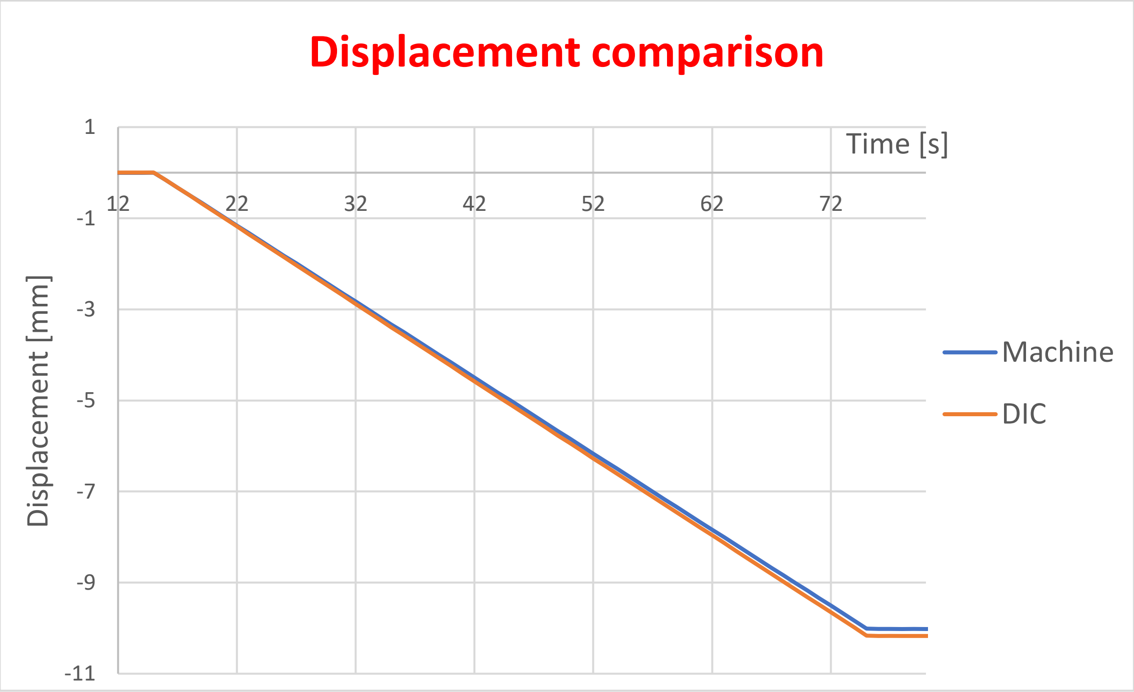

***Figure 4.20**: Displacement comparison from a static rigid body motion with an error of 1,58%*

Setting the exact value of the offset of the calibration speckle helps to reduce the error between the displacement measures from the machine and the DIC analysis. The enhancement of the previous static rigid body motion is shown in **Figure 4.22** below.

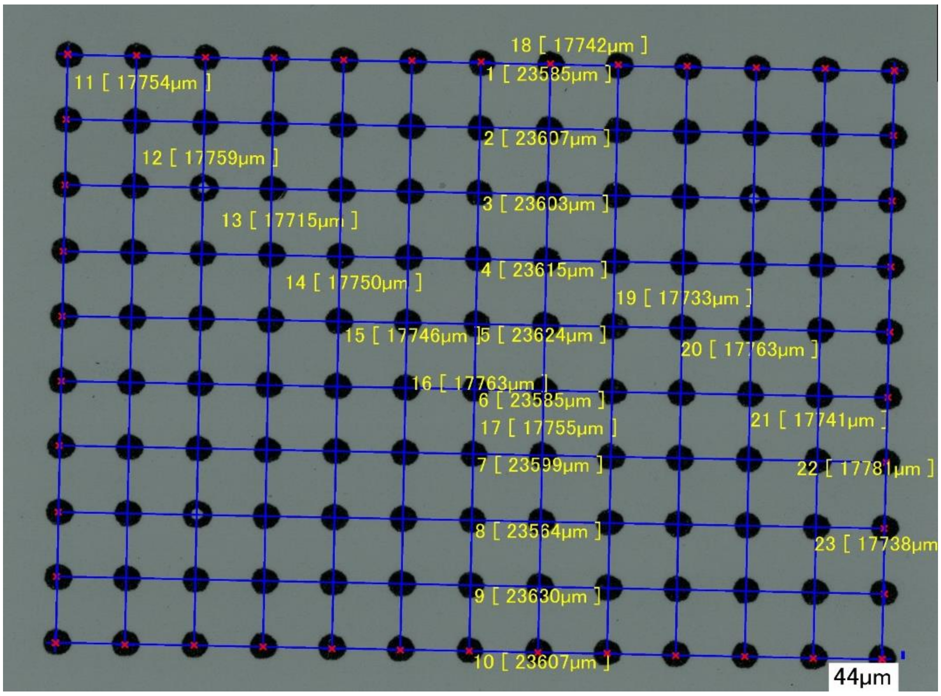

***Figure 4.21**: Calibration speckle measurement under the microscope*

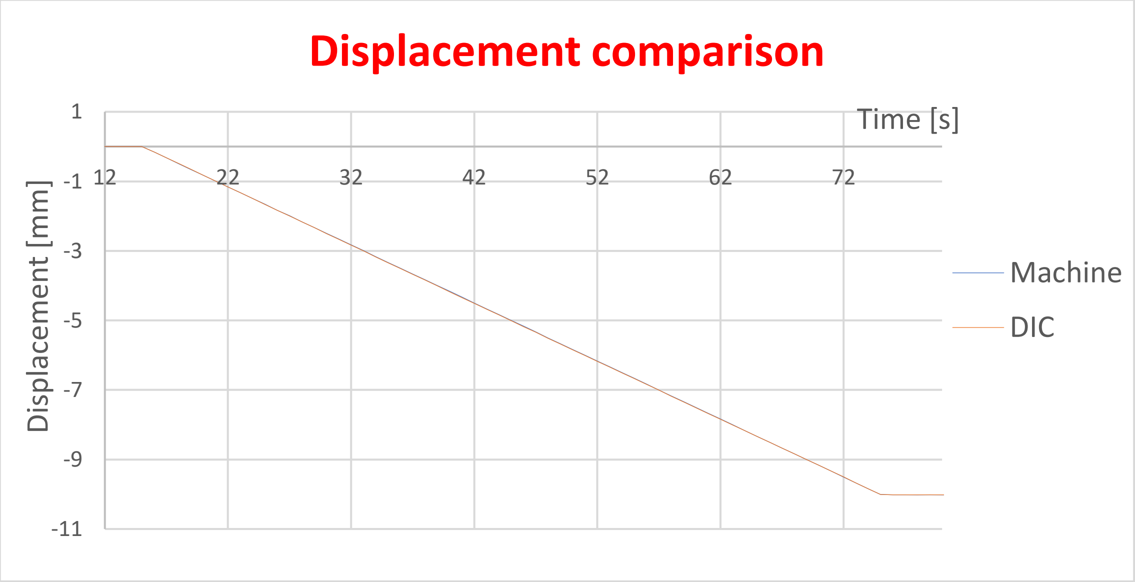

***Figure 4.22**: Displacement comparison from a static rigid body motion with an error of 0,11%*

4.3.4.2 Sinewave

The fatigue rigid body motion is obtained moving the sample to perform a sinewave controlled in displacement. The output data of the displacement from the machine and the DIC are compared to see if there is a delay between them.

For example, as it is shown in **Figure 4.23**, a delay between the signals is present. It can be easily calculated and correct, setting the value of the delay on the LabView input interface.

The delay is function of the shutter time of the cameras. For this project, a shutter time of 5 ms has been used for all the tests and it results in a delay time of 3,5 ms.

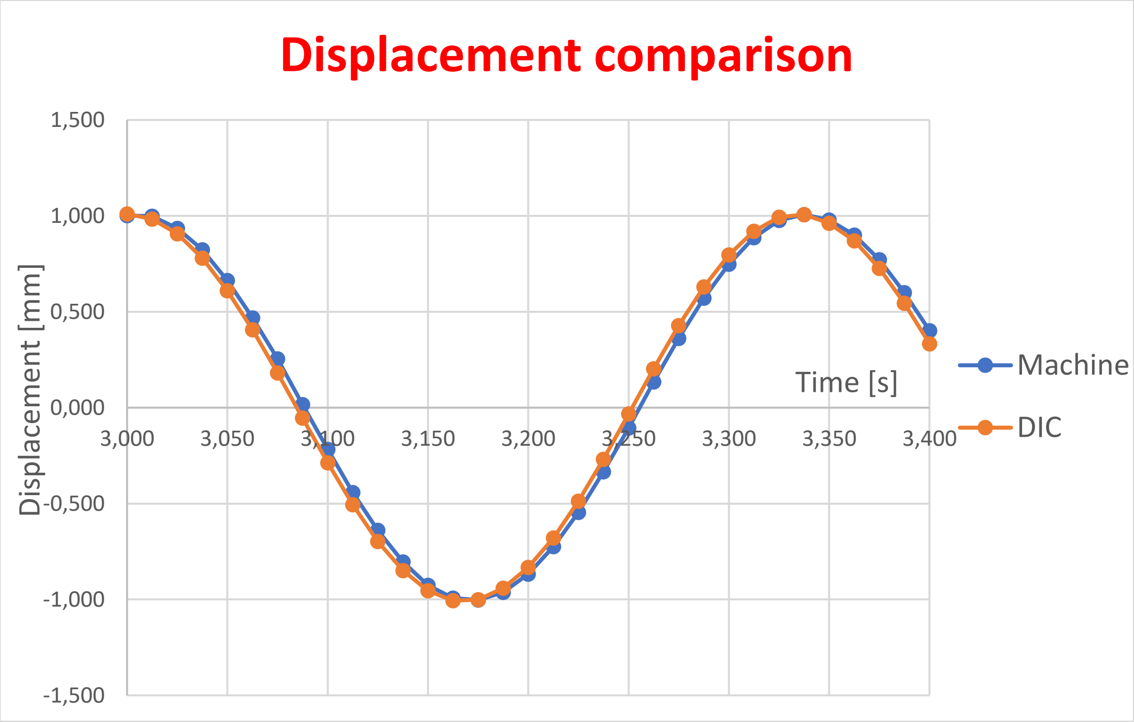

Figure 4.23*: Displacement comparison from a sinewave rigid body motion with a delay between the signals*

Calculating and correcting the delay on LabView, it is possible to align the signals, as shown in **Figure 4.24**.

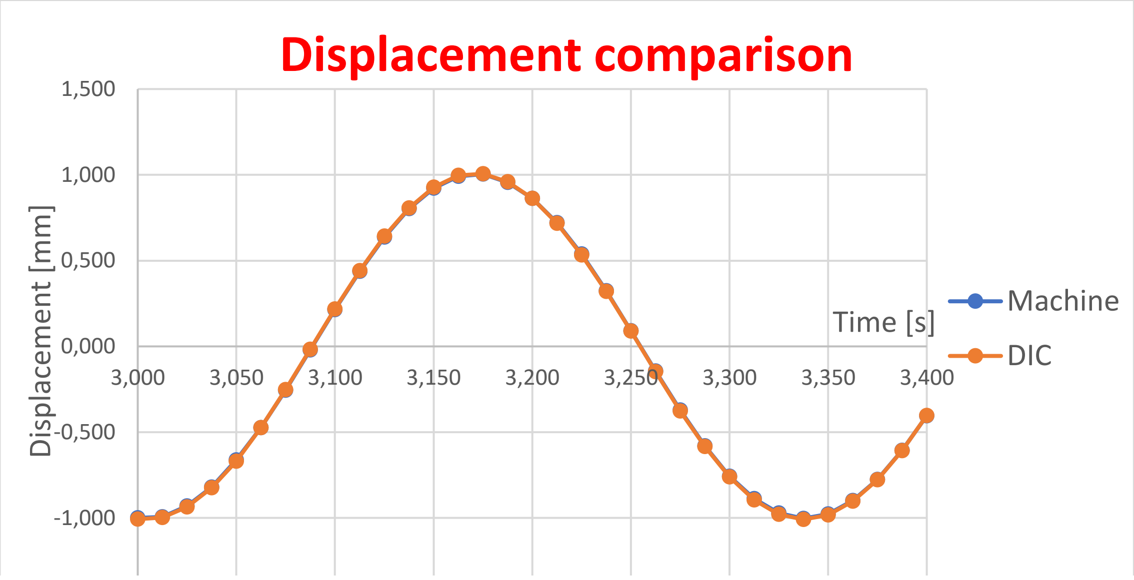

***Figure 4.24**: Displacement comparison from a sinewave rigid body motion without delay between the signals*

5 TEST RESULTS

A fatigue test program was performed on the unidirectional carbon-epoxy material. The idea behind it is to capture relevant characteristics regarding C-C fatigue, sufficiently but within the bounds of what can be done within the timeframe of a master thesis project. In this section, an overview of the tests which have been performed is shortly presented.

When fatigue is typically mentioned, it depicts a phenomenon in which a sample is damaged through cyclic loading at levels below which static failure can be expected. In this sense it is of interest to know exactly what load levels result in (quasi-)static failure of a sample. A total of 6 static tests until failure have been performed, mainly to assess the ultimate compressive strengths of both specimen types.

5.1 Static Tests

To perform fatigue experiments under a constant amplitude cyclic load, it is important to be able to relate the applied load to what a specimen can ultimately cope with. To do this, quasi-static tests can be used to compare the applied load in % to a specimen's ultimate strength. For this test series, a set of quasi-static tests in compression have been performed on specimens for $[(+45/-45)]_{24}$ lay-up. All the tests have been performed at the same displacement rate of 2 mm/min. The results are reported in this section.

5.1.1 Stress-Strain curves

The stress-strain curves are obtained plotting the results of the stress, calculated dividing the load (output from the loadcell) by the initial resistant area of the sample.

$$\vartheta_{XX} = \frac{F_{XX}}{A_{initial}}$$

The values of the strain are calculated from Vic-3D© using "virtual extensometers". These extensometers can be placed in any position and orientation inside the Region of Interest (ROI), during the correlation analysis on Vic-3D©. The longitudinal strain needed to plot the stress-strain curves is positioned as shown in **Figure 5.1** below.

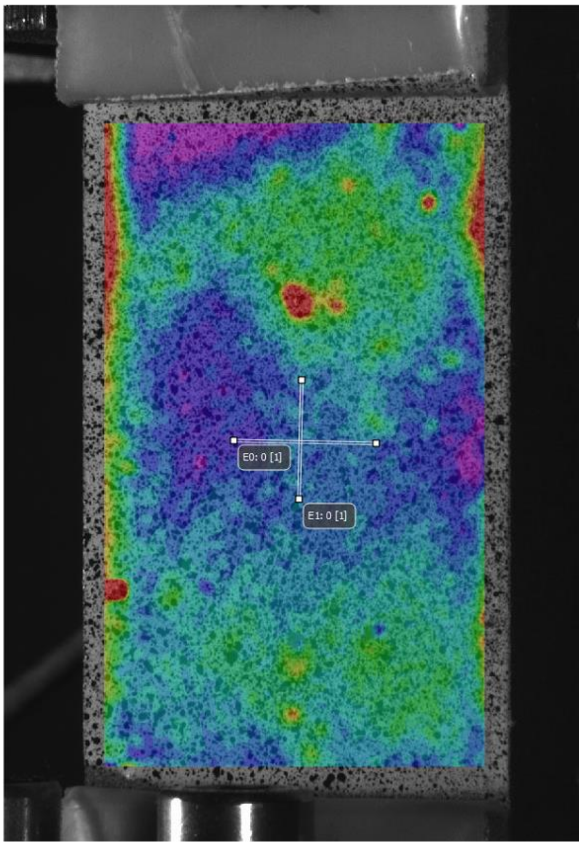

Figure 5.1: *Region of interest correlated and virtually DIC extensometers location: vertical extensometer represents longitudinal strain, horizontal extensometer represents transversal strain*

The behaviour of the stress strain curves, shown in **Figure 5.2**, is different depending on the sample type. The reason is due to the different strain field, as will be explained in 5.1.3. It results in a steeper trend of the D type curves. There is also an exception with the trend of "B12". It has a trend more similar to the D type and at a certain point the strain is increasing. This is probably due to a defect or a premature failure of the sample.

To confirm the typical behaviour, the test results obtained by P. H. Jimenez [30] can also be investigated. The trend of the stress-strain curves can be confirmed, as shown in **Figure 5.3**.

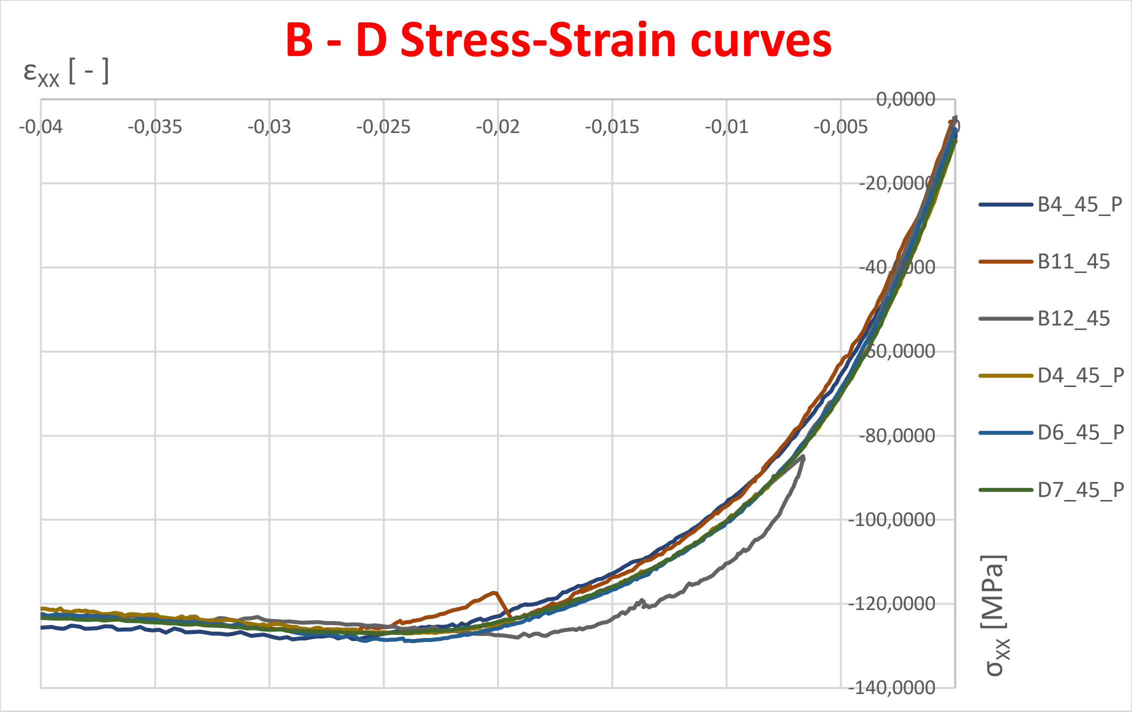

***Figure 5.2**: Stress-Strain curves from static tests*

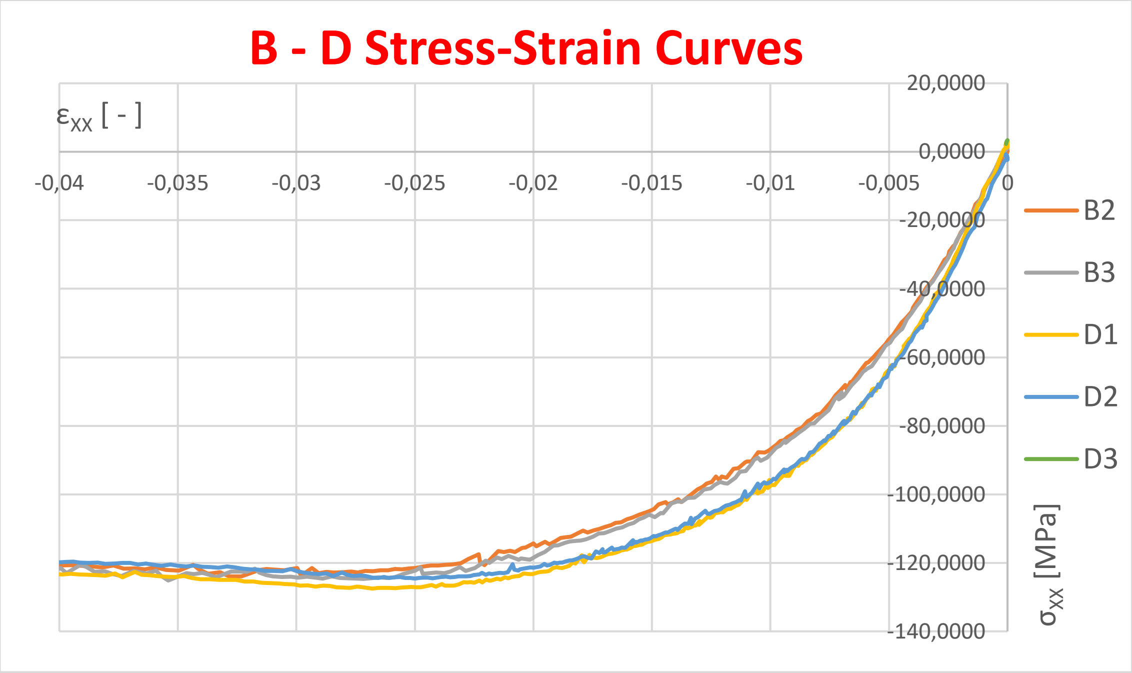

***Figure 5.3**: Stress-Strain curves from P. H. Jimenez [30]*

Looking at the results from P. H. Jimenez [30], shown in **Figure 5.3**, can also be confirmed, that the behaviour of the D type is characterized by a steeper slope of the initial part, that means higher initial stiffness.

It should be mentioned that there is a lower difference of the general trend of the curves between P. H. Jimenez's tests and this project's tests.

5.1.2 Maximum compressive stress

In this paragraph the maximum compressive stress is presented.

Looking at the final part of the stress – strain curves, shown in **Figure 5.4**, the maximum compressive stress is equivalent to the minimum value of the stress reached on the first part of the curve, when the first derivative of the function is negative or null.

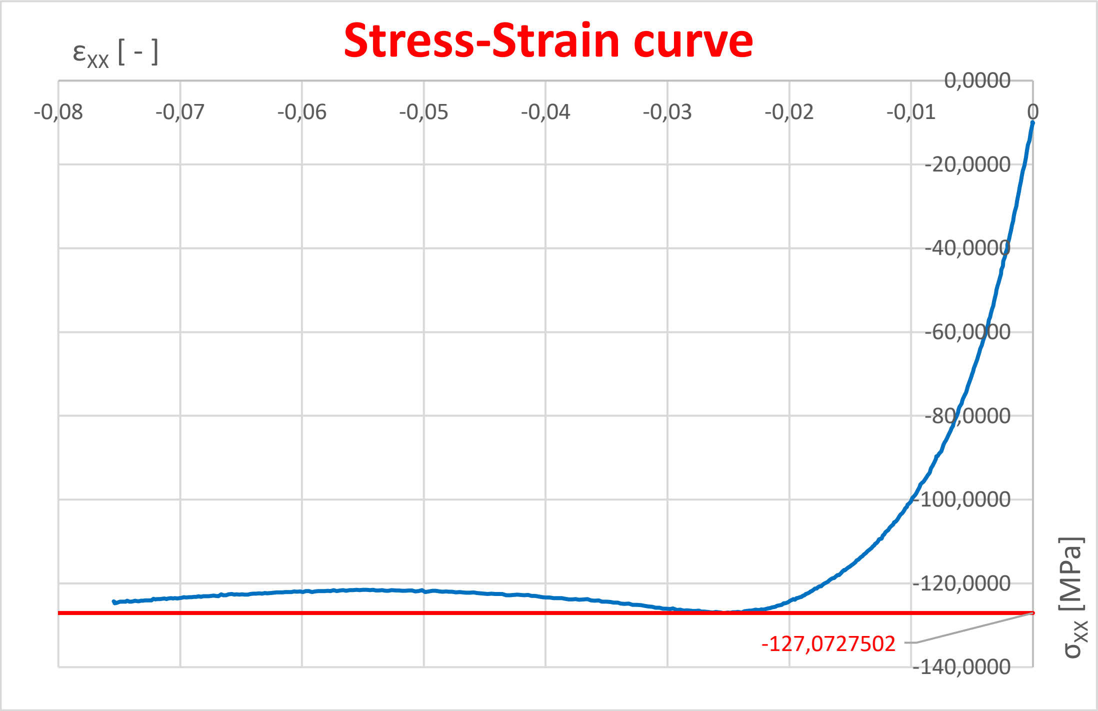

***Figure 5.4**: Maximum compressive stress calculation*

The values of the maximum compressive stress are presented in **Figure 5.5**. All the values are close to each other and the average value is -127,65 MPa. The reason why the values are similar to each other must be searched when the sample is close to the failure. In that condition, the material strength seems not to be altered much by multiaxial stress, this implies very similar values of the maximum compressive stress.

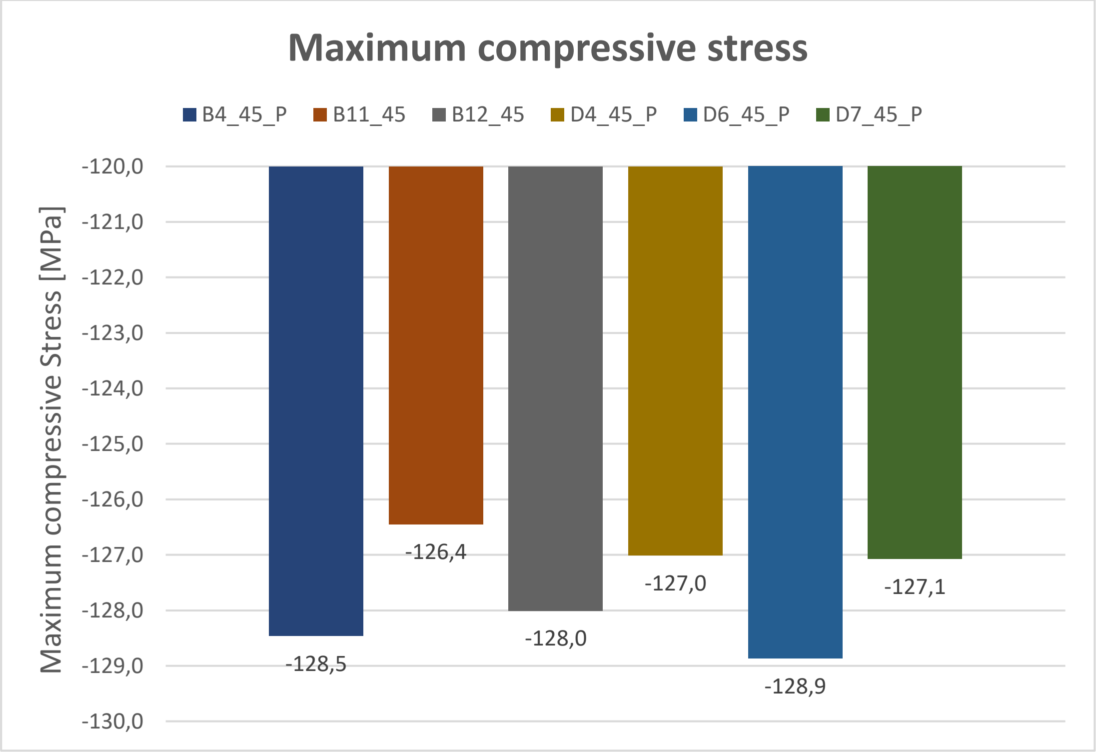

***Figure 5.5**: Maximum compressive stress calculated from static tests*

5.1.3 Strain field comparison

Before to present the result of the stiffness, it is necessary to mention and explain how the strain field is different between the two types of samples. It is due to the different free length characteristic of the different geometry. When on the B type, the tabs are fully bonded, it results in stress concentrations close to the edges of the gauge length. Instead, on the D type, the free length is higher (70 mm) and it allows to better carry tensions without generation of stress concentrations. This comparison has been performed at different stress levels that occurs during a static test. The comparison is shown in **Figure 5.6** below.

Stress Level [Mpa]	D	B
30	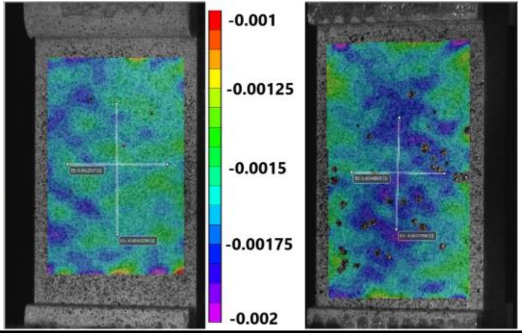	
50	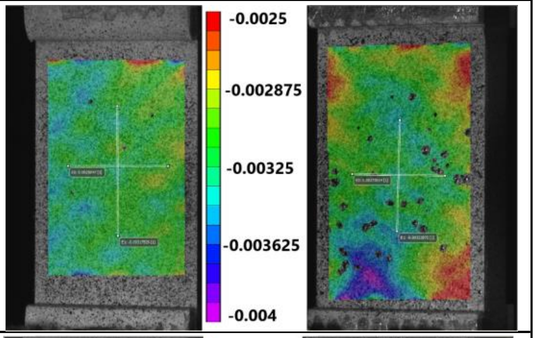	
70	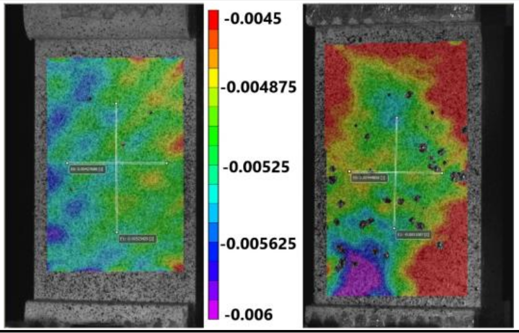	
90	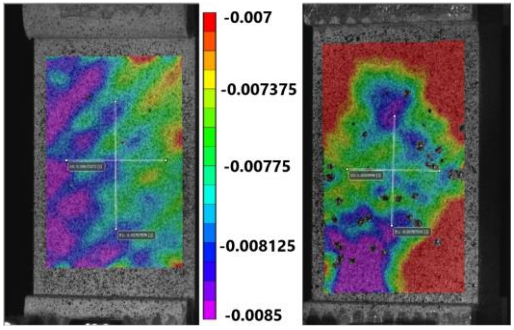	
110	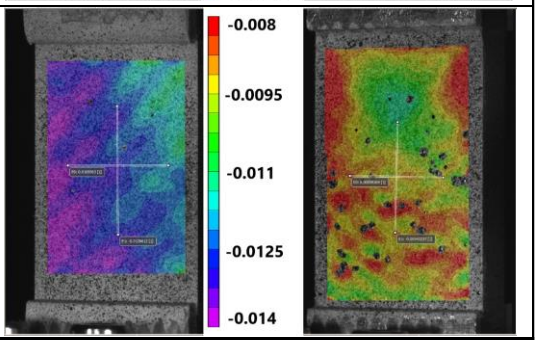	

Figure 5.6*: Longitudinal strain field (ε_{xx}) comparison during a static test, at the same scale (ε absolute value)*

In **Figure 5.6**, the strain field distribution between the two types of samples are compared at different stress levels. It is clearly visible how, on the D type, the strain field is more uniform than the B type. Increasing the stress applied on the specimen it is visible how the fibers are effectively carrying the load on the D type. On the B type, the stress concentrations on the edges becomes higher while the stress level is increasing.

That difference on the strain field of the two samples results in a different behaviour of the stress-strain curves, a different value of the stiffness and in a different stiffness behaviour during fatigue life.

5.1.4 Stiffness

In this paragraph, the definition of the stiffness given by the ASTM D 3410 [44] "Standard Test Method for Compressive Properties of Polymer Matrix Composite Materials with Unsupported Gage Section by Shear Loading" is explained, as well as the results of the stiffness obtained from the static tests.

The normative is presented and explained in 2.2.3.1 and the stiffness calculation has been explained in 3.2.4 before.

To calculate the stiffness, called "Compressive chord modulus of elasticity" on the normative, these instructions are given: "Select the appropriate chord modulus strain range from 0,001 μ_ε and 0,003 μ_ε. Calculate the compressive chord modulus of elasticity from the stress-strain data using the equation below. If data are not available at the exact strain range end points (as often occurs with digital data), use the closest available data point. Report the compressive chord modulus of elasticity to three significant figures. Also report the strain range used in the calculation" [44].

$$E^{chord} = \Delta\sigma / \Delta\varepsilon$$

where:

E^{chord} = tensile chord modulus of elasticity [GPa];

$\Delta\sigma$ = tensile stress range

$\Delta\varepsilon$ = strain range

To improve the reliability of the result, a linear regression has been applied on the datapoints in this interval.

According to ASTM D 3410 [44], the results of the stiffness of the samples, evaluated from static tests, are presented in **Figure 5.7** below.

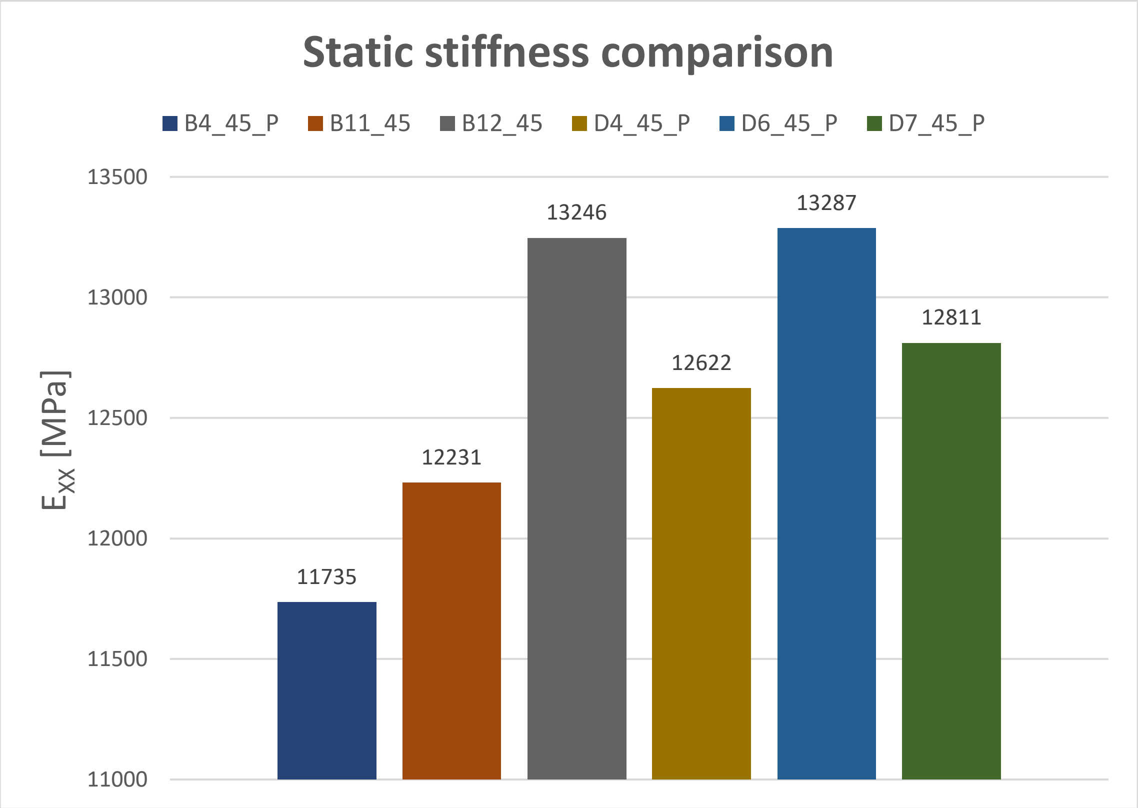

***Figure 5.7**: Stiffness evaluated from static tests according to ASTM D 3410*

As explained before in 5.1.3, due to the different strain field characteristic of the two different specimen types, different values of the stiffness stand out. The only exception is “B12” which, as explained in 5.1.1, has a different behaviour compared on the other B type samples. This is due to an incorrect setting of the distance between the clamps for the “B12”. As can be seen from the **Figure 5.8** below, due to an error during the machine setting, the distance between the clamps was a bit higher than the standard value (35mm).

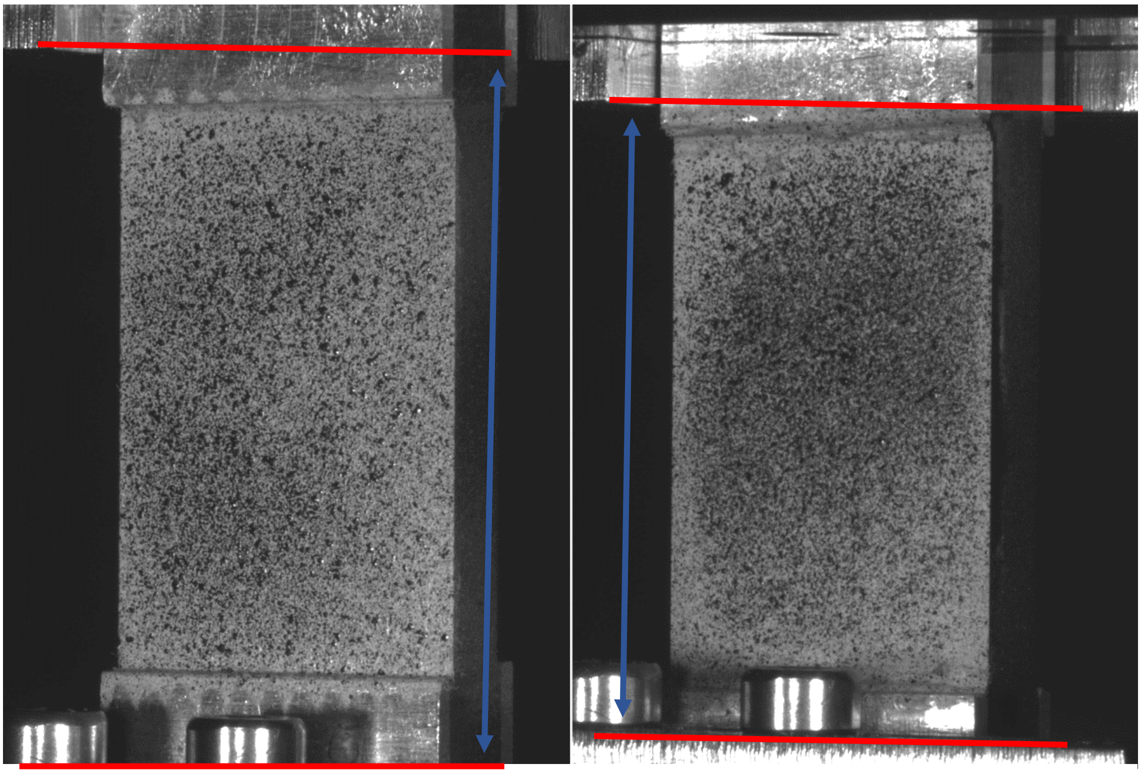

***Figure 5.8:** Normal clamps distance (35mm) on the right and error distance between the clamps on the “B12” on the left*

The bigger distance between the clamps for the “B12” induces a more uniform stress field, as explained before. It is therefore the reason why the stiffness behaviour of the “B12” is more similar to the D trend.

Considering this error, to better investigate the stiffness values from the static tests, P. H. Jimenez’s results obtained with the same samples are shown in **Figure 3.19**. Looking at these results and combining it with results shown before in **Figure 5.7** it is possible to affirm with certainly that the initial stiffness calculated from static tests is higher with D type.

Combining all the results obtained from P. H. Jimenez [30] and from this project, the average stiffness for D type is 13.6 GPa, while the average stiffness for the B type is 12.5 GPa.

5.2 Fatigue Tests

In this second part of the chapter “Test results”, the fatigue test program is presented, followed by the evolution of important parameters characterizing the fatigue behaviour like the temperature, the strain and the stiffness.

To organize, order and elaborate data in output from the correlation analysis and the machine, an Excel© worksheet has been developed. It should also be able to plot results in different graphs. Inside this worksheet, data from DIC and the machine are combined to calculate the evolution of parameters like stress, temperature and displacement during the test. To calculate complex parameters like the stiffness and the permanent strain, two Visual Basic Macro on Microsoft Excel© has been developed. The Macro scripts are presented in 7.1.

5.2.1 Test program

The starting point to define a good test program for the project has been the work done by S. Walraet [29] (presented in 3.1.4.2). Due to the different material (unidirectional CFRP for this project and woven CFRP for S. Walraet’s project), the temperature issue encountered by S. Walraet is now less serious. It means that to perform a fatigue test in less time, the frequency of the fatigue tests for this project can be higher.

The test program of the fatigue test is presented in **Table 2** and **Table 3**.

Fatigue B type				
Code	**Max Stress** [%]	**Stress** [MPa]	**Frequency** [Hz]	**N° cycles** [-]
B10_45_P	80%	-102,1	1	1551
B2_45_P	80%	-102,1	1	1479
B6_45	80%	-102,1	1	1473
B16_45	80%	-102,1	1	1189
B15_45	80%	-102,1	1	1017
B8_45	70%	-89,3	1	18262
B18_45	70%	-89,3	1	12990
B19_45	70%	-89,3	1	10556
B20_45	70%	-89,3	1	10953
B21_45_P	70%	-89,3	1	15507
B23_45_p	70%	-89,3	1	11207
B5_45	65%	-83,0	3	139154
B9_45	65%	-83,0	3	139031
B17_45	65%	-83,0	3	87185
B7_45	60%	-76,6	3	900000

***Table 2**: Fatigue test program for B type*

Fatigue D type				
Code	**Max Stress** [%]	**Stress** [MPa]	**Frequency** **[Hz]**	**N° cycles** [-]
D8_45	80%	-102,1	1	429
D2_45_P	80%	-102,1	1	2181
D11_45	70%	-89,4	1	17242
D15_45	70%	-89,4	1	15114
D16_45_P	70%	-89,4	1	14822
D17_45	70%	-89,4	1	13249
D1_45_P	65%	-83,0	3	112800
D13_45	65%	-83,0	3	88205
D14_45	65%	-83,0	3	86543
D10_45_P	60%	-76,6	3	955000

***Table 3**: Fatigue test program of D type*

As is shown on the tables, many maximum stresses have been used to better describe the fatigue behaviour of the material. The frequency is a function of the stress applied on the sample. A high stress level induces more damage, which induces more friction, that increases the heat generated and results in a temperature rise. For high stress levels the frequency should be reduced. For low stress levels the frequency can be increased.

5.2.2 Temperature evolution

It is important to keep track of the temperature of the sample during the test because if it reaches high values, the fatigue behaviour would be compromised. The main objective for a fatigue test session is to perform fatigue tests in the fastest way possible, without reaching higher temperatures that will invalidate the tests.

For this project, the temperature measurements have been done using a thermocouple, as explained in 4.1.3.

The maximum temperature fixed as a limit for this project is 40 °C (absolute value) and none of the tests exceeded this value.

However, there is a large difference between the temperature behaviour of the two samples, as shown in **Figure 5.9** below. The D type, due to the partially debonded tabs, is more subjected to friction between the aluminium tabs and the composite material. It results in a higher temperature before the sample failure. Anyway, also with the load condition that induces higher temperatures on the materials (65% of the maximum load and a frequency of 3 Hz), the maximum temperature reached is lower than the limit fixed for the acceptability of the test. All the tests performed during this project kept the temperature within the limit for the duration of the test.

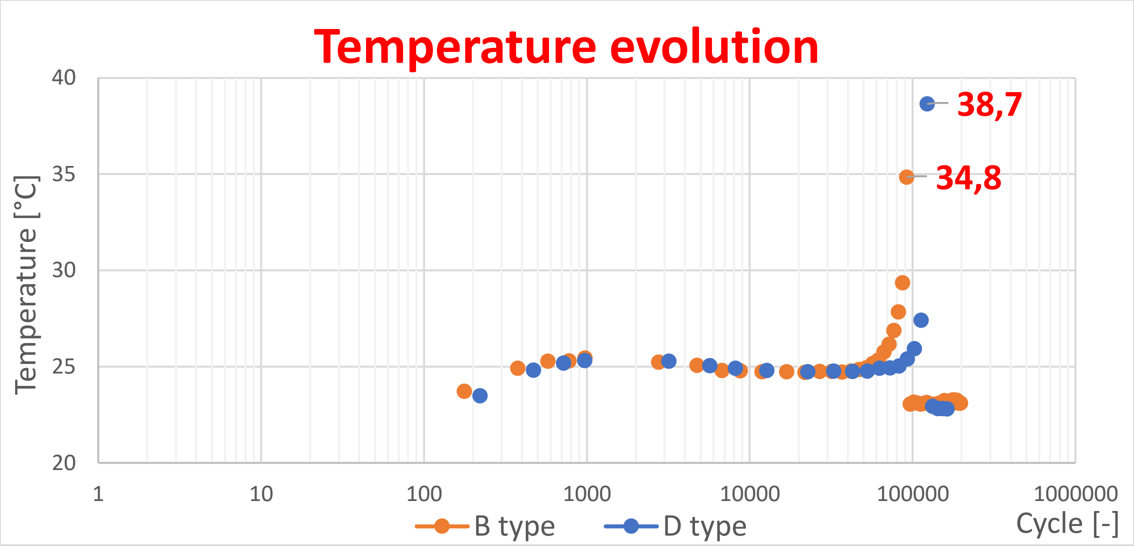

***Figure 5.9**: Temperature behaviour comparison between the two types of samples under the same load conditions (65% of the maximum load and 3 Hz)*

5.2.3 S-N curve – Wöhler curve

In this paragraph, the Wöhler curve, containing the results of all the tests performed during this project, is presented in **Figure 5.10**.

The static values of the maximum stress are plotted close to the Y axis (at a value of the number of cycles equal to 1). This value is the result of the average of the maximum stress obtained from static tests of B and D type samples. The values are respectively -127,6 MPa for the B and -127,7 MPa for the D. Thus, the average value plotted on the curve is -127,65 MPa.

Two datasets containing the results of the B and D type fatigue tests are plotted. The number of cycles at failure, the frequency and the maximum stress applied for each test are presented in **Table 2** for the B type and in **Table 3** for the D type.

Two logarithmic trendlines are plotted to better understand the trend of the curve. Despite the use of trendlines, the behaviour of the B and D type is very similar. It is possible to affirm that the fatigue life behaviour is a function of the material and it is not influenced by the two different sample's geometry used for this project.

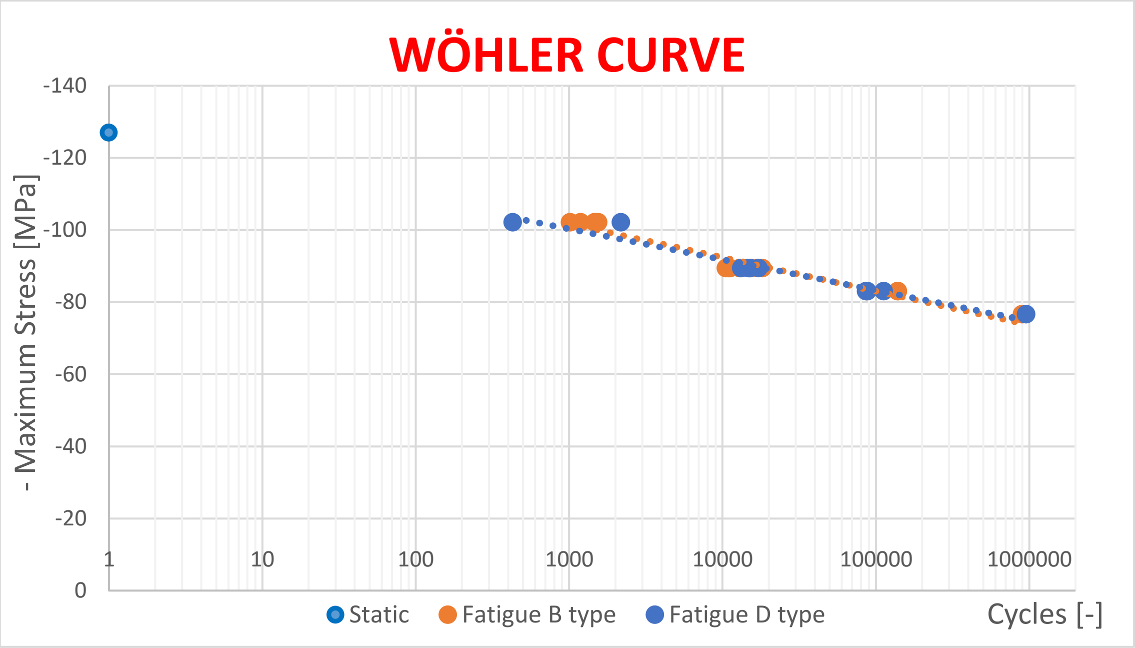

***Figure 5.10**: Wöhler curve for unidirectional carbon-epoxy [+45/-45]$_{6S}$ R=10, the results obtained from B and D type samples are plotted, logarithmic trendlines are plotted*

5.2.4 Strain evolution

In this paragraph, the strain evolution, containing the results of the most representative load condition is presented. In order to plot the hysteresis loops it is necessary to plot the values of the longitudinal (X direction) strain calculated from the correlation of the cameras' images and the stress calculated from the output data from the machine.

To obtain the correct values of the strain from the images acquired by the cameras it is necessary to virtually place two extensometers during the correlation analysis in Vic-3D®. The position of the extensometers is the same as used to calculate the stress-strain curves for the static tests in 5.1.1 and it is shown in **Figure 5.1**.

To calculate the values of the stress, the load obtained from the loadcell on Instron 8801 is divided by the resistant section area of the sample, measured before the test.

A Visual Basic macro on Microsoft Excel© has been developed, in order to plot the cycles with corresponding series' name and cycle number. The Macro script is shown in Appendix (7.1.1).

Combining the values, the stress-strain cycles can be plotted in a graph. With the load condition at 65% of the maximum stress and 3 Hz frequency, the more significant behaviour can be plotted, as shown in **Figure 5.11** and **Figure 5.12**.

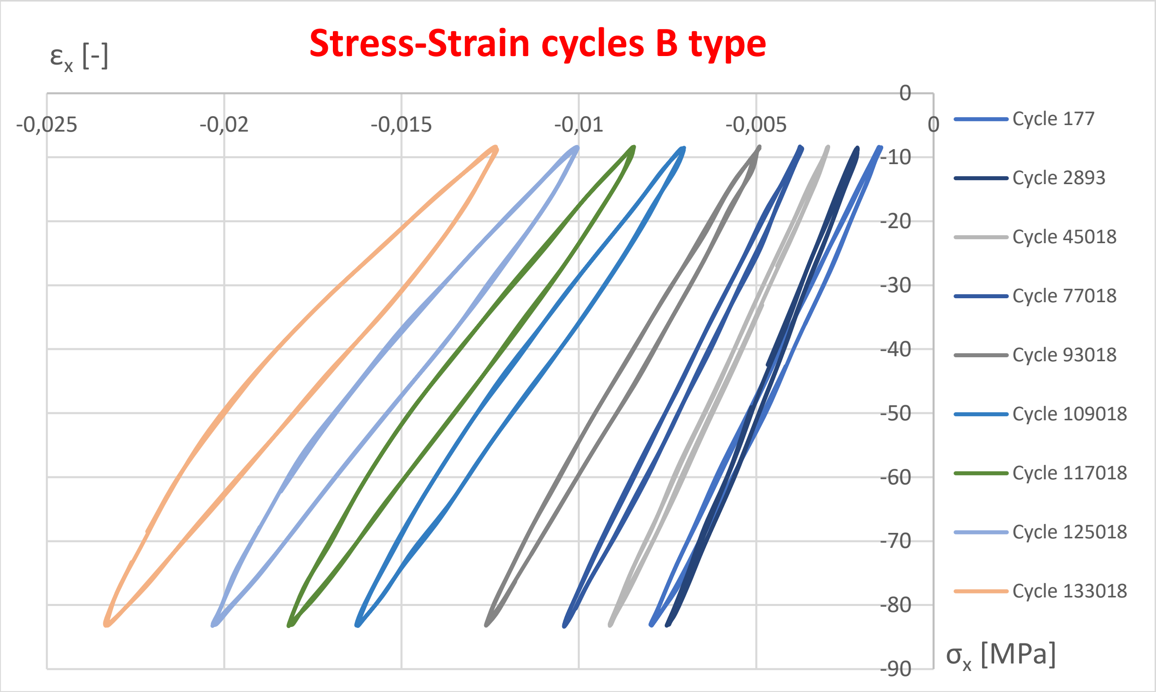

***Figure 5.11**: Stress-Strain behaviour for B type, load condition: 65% of the maximum load and 3Hz frequency*

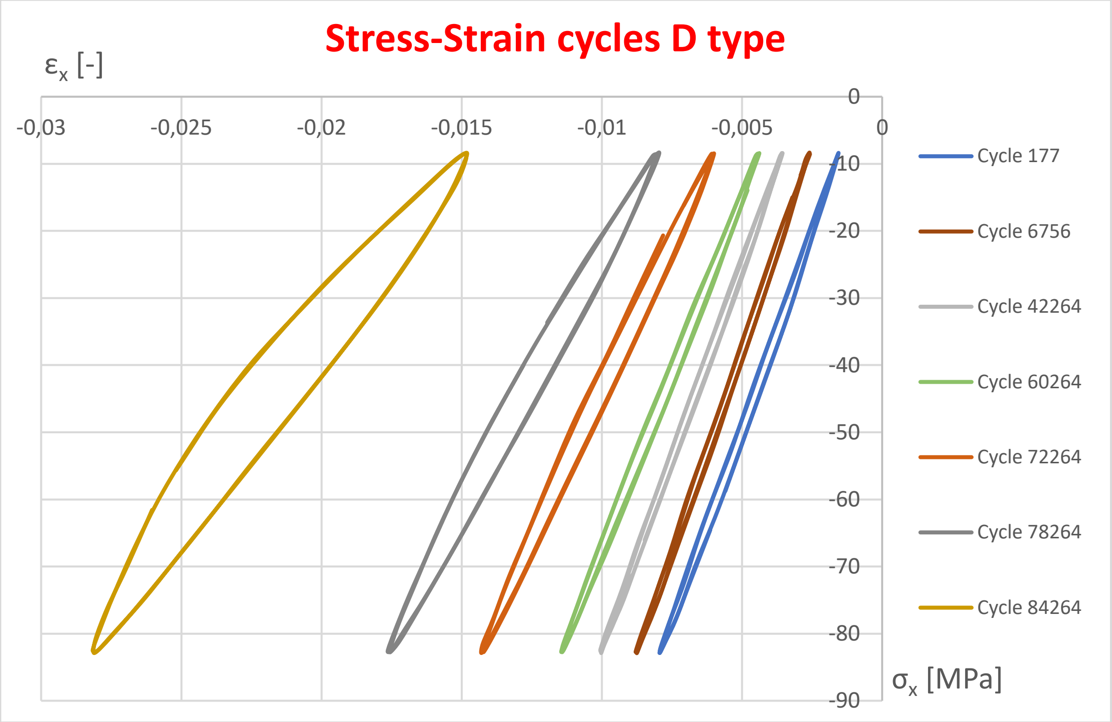

***Figure 5.12**: Stress-Strain behaviour for D type, load condition: 65% of the maximum load and 3Hz frequency*

It is known and it will be explained further that the slope of the stress-strain cycles is representative of the stiffness of the material. Looking at the stress-strain cycles behaviour it is possible to have a general idea of the stiffness trend during the tests. The stiffness behaviour will be focused below, but for now it is possible to have a general idea of it.

It is evident looking at **Figure 5.11** for the B type, how the slope of the cycles is increasing during the test, especially on the first part. This is not true for the D type behaviour, shown in **Figure 5.12**, where the slope of the cycles is decreasing. As explained before, this is representative of the stiffness behaviour. With the B type samples, the stiffness is increasing during the test and it is not a realistic situation and will be deepened further.

Another parameter that can be focused looking at the stress-strain cycles is the area of the cycles. It is related to the hysteresis of the material and it is representative of the damage level of the material. The larger is the area, the higher is the damage inside the material and the heating generated inside. This is also related to visco-elasticity of the material. A perfect linear elastic behaviour should be represented by a line instead of a cycle. During the test, the material is damaged and the permanent strain increases. This can be seen from the translation of the cycles and will be explained below.

5.2.5 Permanent strain evolution

Visco-plastic deformation is a process in which permanent deformation is caused by a load that overpass the limit of the material. It produces a permanent change in the shape or size of a solid body without fracture, resulting from the application of sustained stress beyond the elastic limit.

After a material has reached its elastic limit, further deformation will result in permanent strain, also known as visco-elastoplasticity for fragile composite material like the CFRP.

Unlike purely elastic substances, a viscoelastic substance has an elastic component and a viscous component. The viscosity of a viscoelastic substance gives the substance a strain rate dependence on time. Purely elastic materials do not dissipate energy (heat) when a load is applied, then removed. However, a viscoelastic substance loses energy when a load is applied, then removed. Hysteresis is observed in the stress–strain curve, with the area of the loop being equal to the energy lost during the loading cycle, as explained before in 5.2.4. Since viscosity is the resistance to thermally activated plastic deformation, a viscous material will lose energy through a loading cycle. Permanent deformation results in lost energy, which is uncharacteristic of a purely elastic material's reaction to a loading cycle.

For C-C tests of $[+45/-45]_{6S}$ laminates, permanent strain ϵ_{perm} is a parameter of interest. It is defined in this work as the difference in strain at the smallest compressive load applied in cycle x, compared to the strain at the start of the first fatigue cycle (with a compressive load of 10% $\sigma_{\max}$ already applied). See figure **Figure 5.13**.

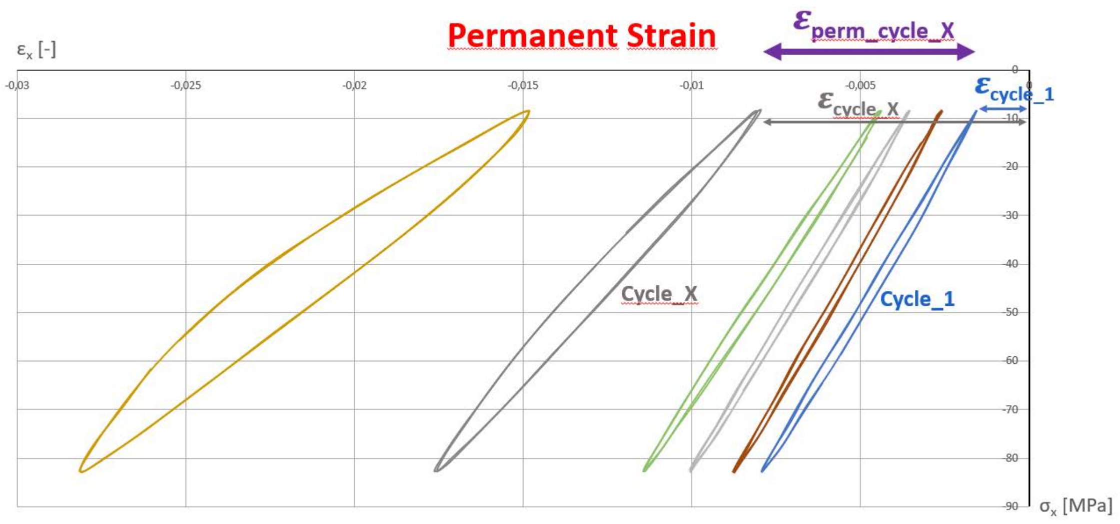

Figure 5.13: *Definition of permanent stress*

A Visual Basic macro on Microsoft Excel© has been developed, in order to calculate the permanent strain and to plot in a graph. The Macro script is shown in Appendix (7.1.1).

The evolution of the permanent strain for all the stress level and the relative frequencies is shown in **Figure 5.14**.

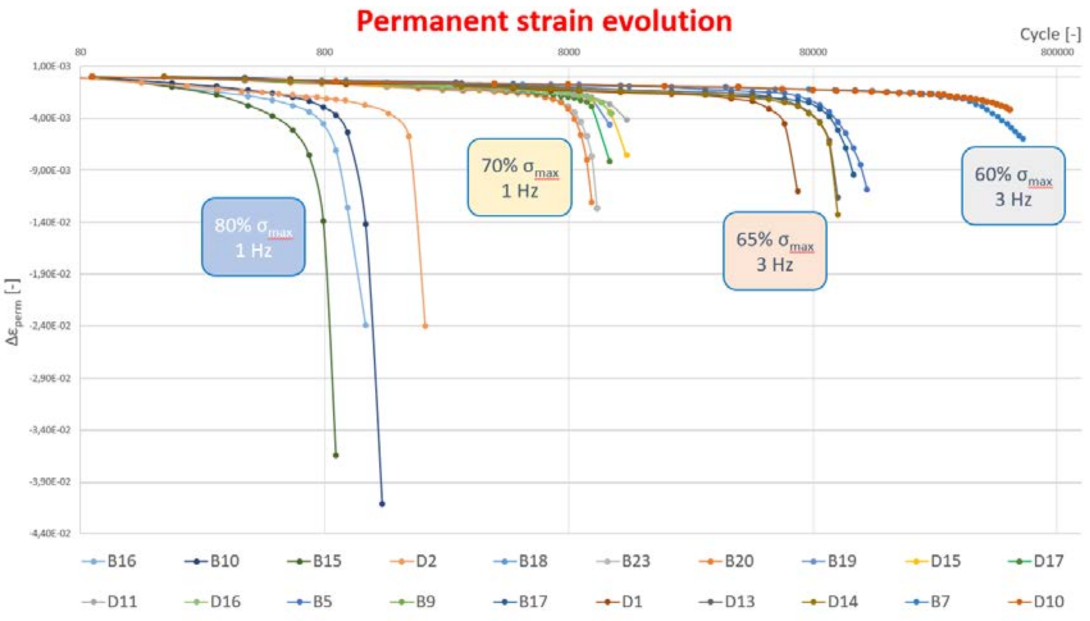

Figure 5.14: *Permanent strain evolution for all the stress levels*

Analysing the behaviour of the permanent strain from the graph, the trend is very clear and coherent for all the samples. The reliability of the results is very good, except for the 80% of the maximum stress where the dispersion of data is higher.

It is possible to affirm that the general trend of the curves is similar for the different stress levels. The first part of the curve has a linear decreasing, in which the slope of the curve is function of the stress applied. Higher is the stress and higher is the slope of the first part of the curve, and vice versa. Close to the failure of the sample, the permanent strain is increasing very fast, until it reaches the failure. The number of cycles at failure is function of the stress applied and it is presented in 5.2.1 above.

5.2.6 Stiffness evolution

It is recognized widely that stiffness changes during the service loading of composite laminates can be significantly large, especially when those changes affect deflections, dimensional changes, vibration characteristics, and load or stress distributions. Several generic sources of stiffness change can be identified, in various degrees, in FRPs. The source which occurs quite early in the life of a specimen or component is matrix cracking, and it will be investigated further and related with the stiffness behaviour in paragraph 5.2.6.

Defining stiffness is important for this section. In order to the define the stiffness, the approach applied here is to take two time points in a cycle and compare stress and strain to obtain stiffness. Caution for selecting these points is important. For cyclic loading, there will be a distinction on the definition of stiffness with respect to R-ratio. In particular when potential permanent strain is considered, the logical approach is to define stiffness in the unloading part of a cycle, the hypothesis being that no new damage is developed in this part of the cycle. For R = 10, the approach is, therefore, to use stress and strain at a peak point (at largest compressive load), choose the following valley point (around 10% of this peak stress) and define stiffness through the interval in between these two points. A linear regression is performed of all the points in between the point at the peak and valley (defined before), see **Figure 5.15**.

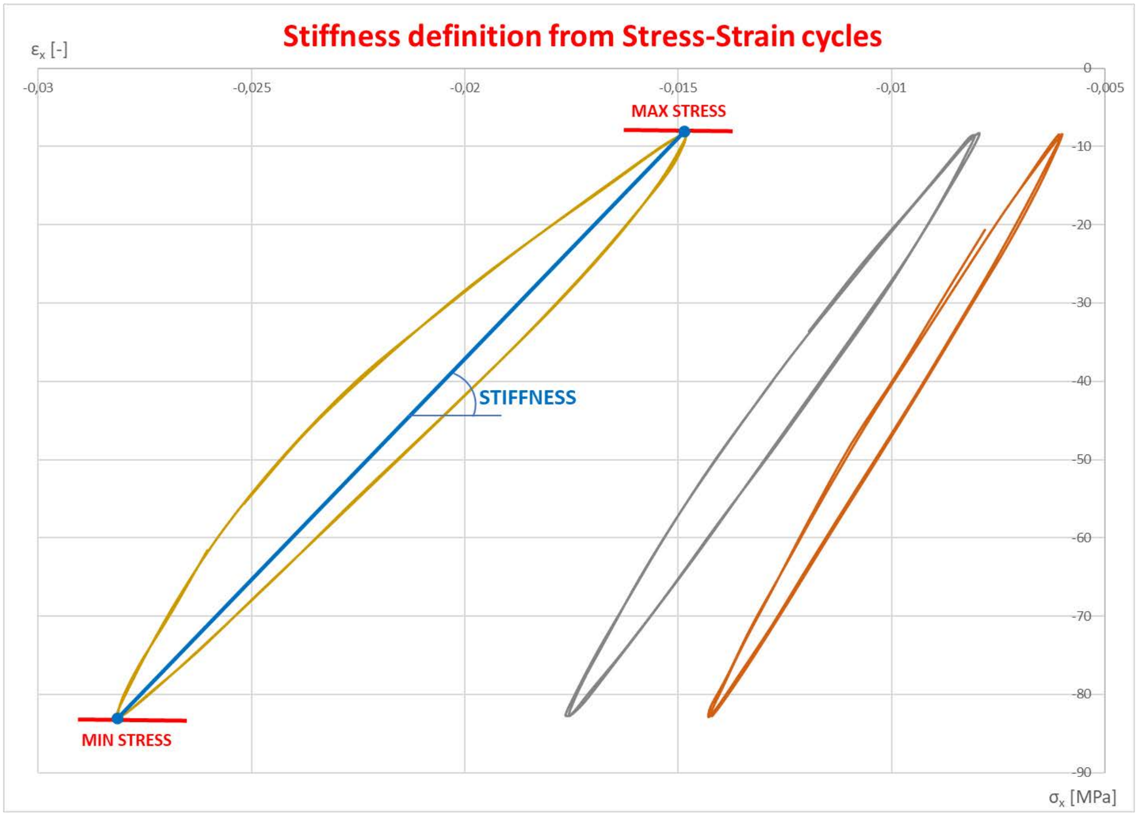

***Figure 5.15**: Definition of stiffness from Stress-Strain curves*

A Visual Basic macro on Microsoft Excel© has been developed, in order to calculate the permanent strain and to plot in a graph. The Macro script is shown in Appendix (7.1.2).

The results of the stiffness evolution obtained from the fatigue tests are plotted on several graph for each stress level in order to have a comparison between the two type of samples' stiffness trend.

5.2.6.1 Load conditions: 60% of the maximum stress and 3 Hz of frequency

In **Figure 5.16** below, the stiffness evolution at 60% of the maximum stress and 3 Hz of frequency is presented.

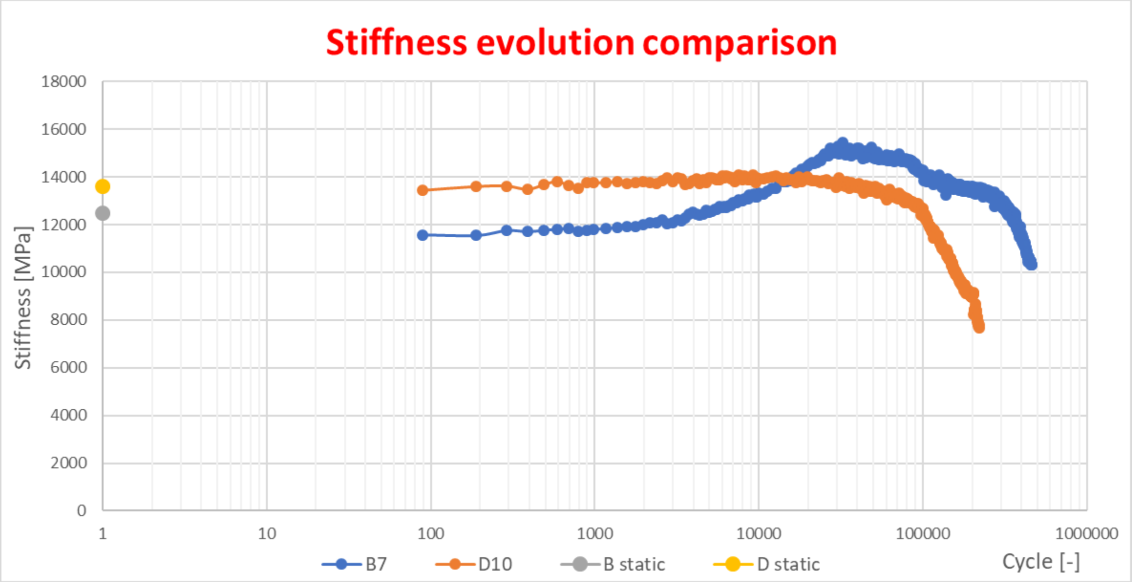

Figure 5.16: *Stiffness evolution comparison: load conditions: 60% of the maximum stress and 3 Hz of frequency*

The results of the stiffness obtained from the static tests are plotted in correspondence of the fictitious cycle 1. As explained in 5.1.4 before, the initial stiffness of the D type is higher.

The stiffness evolution of the B type is characterized by an increasing that start almost immediately. After the peak at 30000 cycles, the stiffness decreases until the sample fails around 950000 cycles. A small increase of the stiffness is also visible for the D type.

Has to be mentioned that the starting value of the stiffness evaluated from the fatigue test is higher for the D compared with the B. The reason is explained in 5.1.4 before, and it is due to the different strain field of the sample. During the fatigue life, the tabs of the B type starts to debond and it induce a stiffness increase. This phenomenon will be investigated and explained below in 5.3.2.

5.2.6.2 Load conditions: 65% of the maximum stress and 3 Hz of frequency

In **Figure 5.17** below, the stiffness evolution at 65% of the maximum stress and 3 Hz of frequency is presented.

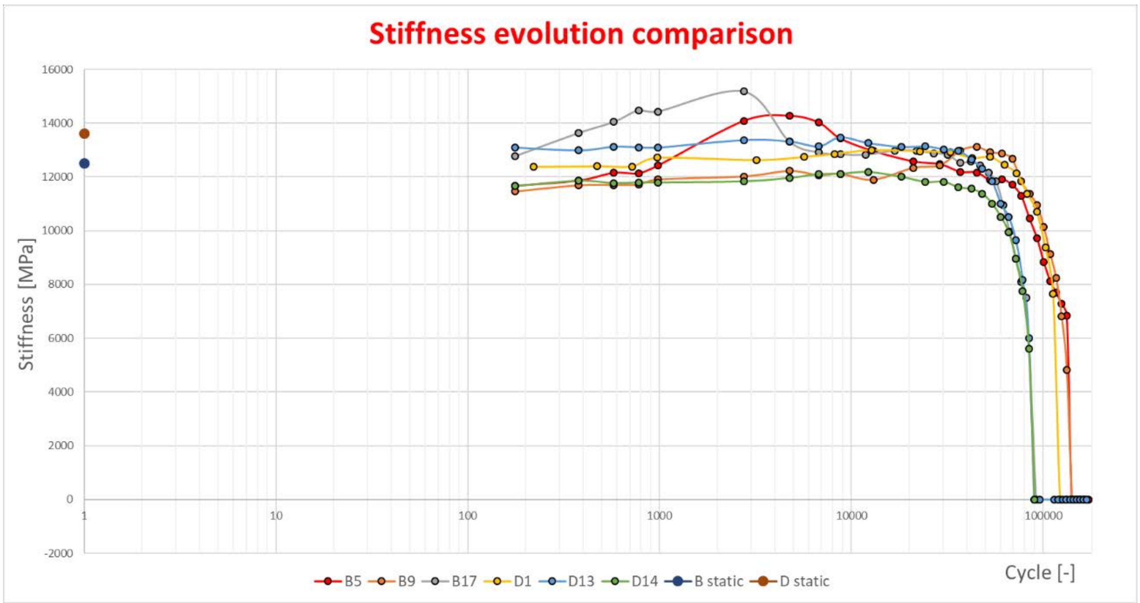

***Figure 5.17**: Stiffness evolution comparison: load conditions: 65% of the maximum stress and 3 Hz of frequency*

For this loading conditions, more tests were performed (3 B type and 3 D type).

The behaviour of the B type is characterized by an increasing of the stiffness during the fatigue life. For the three B type samples, the point at which it begins to increase can be different. The “B17” starts to increase almost immediately, the “B5” starts around 1000 cycles and “B9” increase the stiffness close to the end of the life. This different behaviour is due to a different “starting conditions” of the samples. The reason can be due to the different bonding interphase of the tabs or due to the presence of initial microdefects inside the composite material. It will be investigated further on the next paragraph (5.3), analysing the damage propagation during the fatigue life.

The behaviour of the B type is similar to the previous load conditions (5.2.6.1). For the “D1” and “D14”, a small increasing of the stiffness can be observed. Instead, the sample

"D13" present an almost constant value of the stiffness during the fatigue life and a fast decreasing before the failure.

Has to be mentioned that the starting value of the stiffness evaluated from the fatigue test is usually higher for the D compared with the B. The reason is explained in 5.1.4 before, and it is due to the different strain field of the sample. The only exceptions are the "B17" where the stiffness increase probably start before 100 cycles (before 100 cycles the DIC cameras are not recording) and the "D14" which present a general lower trend compared to the other D type samples.

5.2.6.3 Load conditions: 70% of the maximum stress and 1 Hz of frequency

In **Figure 5.18** below, the stiffness evolution at 70% of the maximum stress and 1 Hz of frequency is presented.

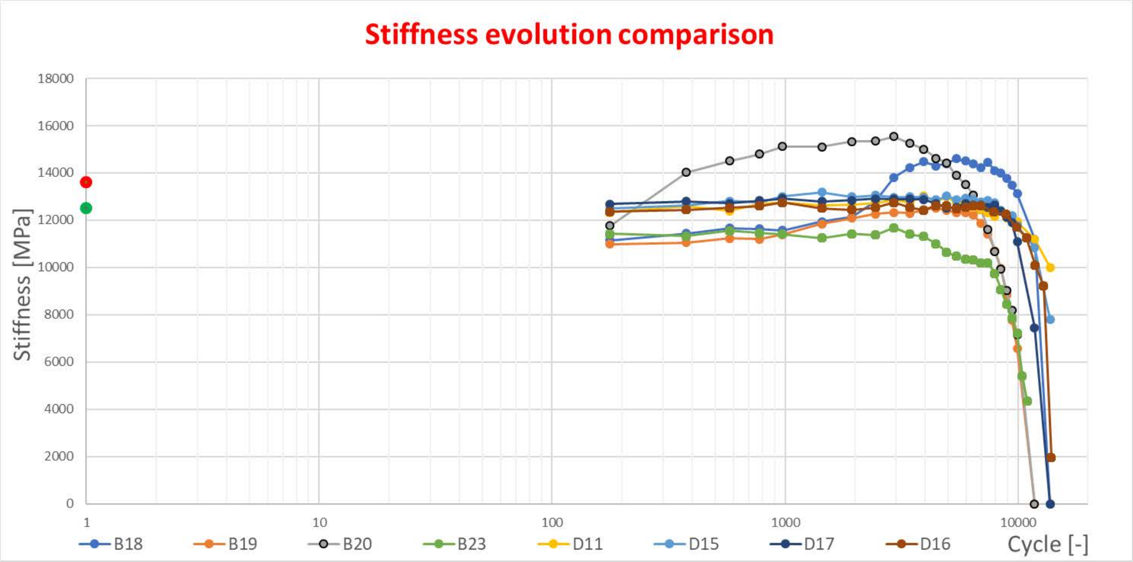

Figure 5.18: *Stiffness evolution comparison: load conditions: 70% of the maximum stress and 1 Hz of frequency*

This load condition gives the best results of the stiffness behaviour. All the B type samples start with a lower value of the initial stiffness compared with the D. All the B type samples show an increase of the stiffness that can appear at the beginning of the fatigue life ("B20"), or close to the end ("B18"). However, all the D type samples start with a higher value of the stiffness. This value of the stiffness remains almost constant for much of the fatigue life and close to the end it decreases until the sample reaches the failure.

5.2.6.4 Load conditions: 80% of the maximum stress and 1 Hz of frequency

In **Figure 5.19** below, the stiffness evolution at 80% of the maximum stress and 1 Hz of frequency is presented.

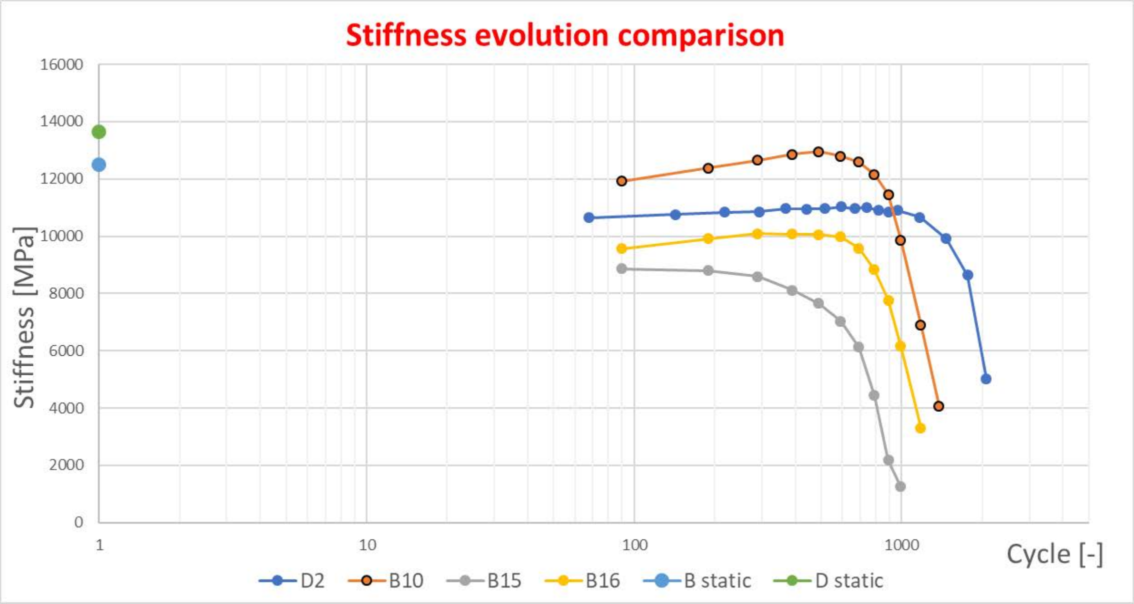

***Figure 5.19**: Stiffness evolution comparison: load conditions: 80% of the maximum stress and 1 Hz of frequency*

This load condition gives the worst results of the stiffness behaviour. The stiffness evolution for this load condition is very fast and it is difficult to monitor the behaviour during the fatigue life. The B and D type trends are difficult to distinguish and characterize.

Another explanation for this behaviour is the non debonding of the tabs due to the short fatigue life. It impedes the achievement of uniformity of the strain field during the test and it result in low peaks of the stiffness value compared to the other load conditions.

5.2.6.5 Stiffness comparison

In **Figure 5.20** below, an overall comparison with the most representative results of the stiffness behaviour of the B type for each load condition is presented.

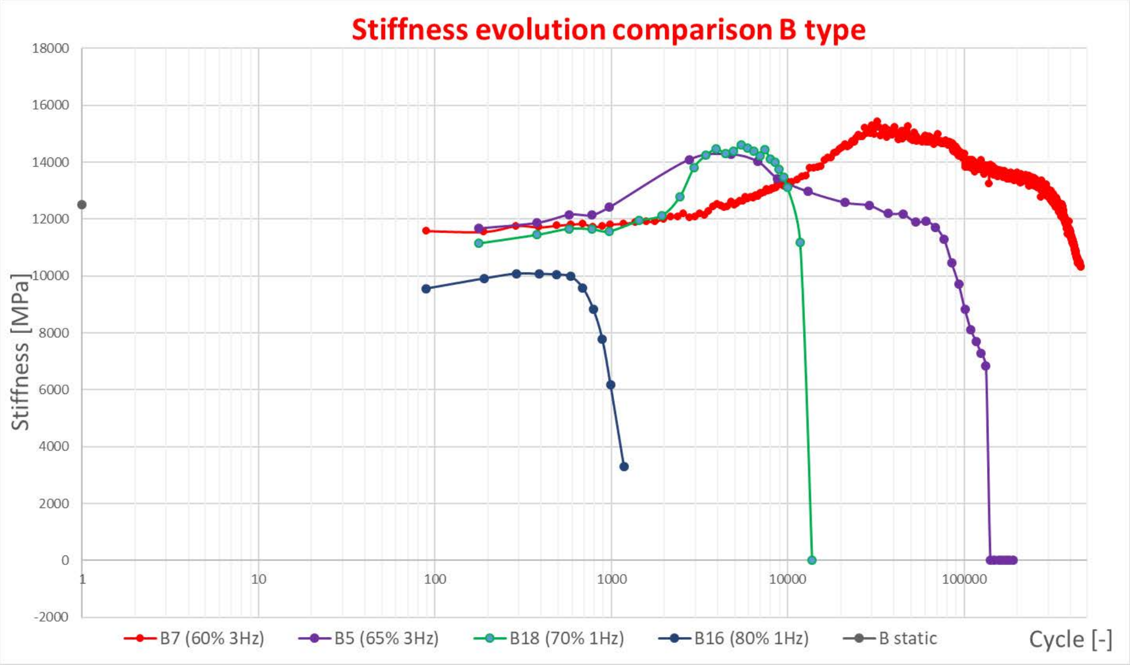

***Figure 5.20**: Stiffness evolution comparison for B type and different load conditions*

Combining the most representative results of the stiffness behaviour, for different load conditions, it is possible to confirm that for each one is characterised by an increasing of the stiffness. It is also possible to affirm that the peak of the stiffness is not function of the stress level applied. It can be noticed by the similar peak for "B18" and "B5", reached at a similar number of cycles but at different load conditions applied.

However, it is still unknown why for the 60%, 65% and 70% of the maximum stress, the value of the stiffness at the peak is higher than the value of the stiffness evaluated from the static tests. It will be further investigated in the next chapter "Damage analysis" (5.3).

In **Figure 5.21** below, an overall comparison with the most representative results of the stiffness behaviour of the D type for each load condition is presented.

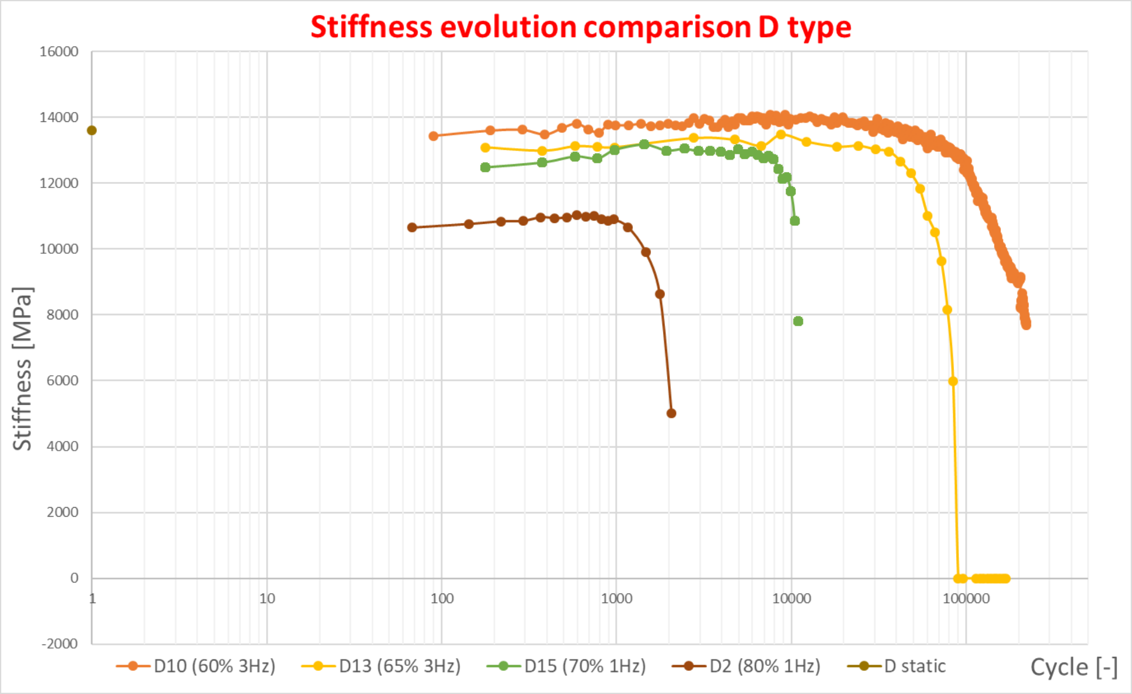

Figure 5.21*: Stiffness evolution comparison for D type and different load conditions*

Combining the most representative results of the stiffness behaviour for different load conditions it is possible to confirm that the curves generally remains constant for the most part of the fatigue life and close to the failure, the stiffness decrease to zero.

The value of the stiffness in the constant stretch of the curve is function of the load applied at the samples. The lower the load and the higher the stiffness in the constant stretch of the curve. The value of the stiffness never exceeds the value of the stiffness evaluated from the static tests.

It is also possible to affirm that, especially for the high load conditions, a small increase of the stiffness at the beginning is visible. It can be due to the exceed of the bonding between the Teflon tape and the tabs that can alter the strain field, inducing a lower stiffness. It will be investigated in the next chapter 5.3.

5.3 Damage analysis

In this third part of the chapter “Test results”, in order to explain some macroscopic parameter’s behaviour presented in the paragraph before (5.2), a damage analysis has been performed on two samples. The damage inside the material will be investigated, monitoring the presence of delaminations and measuring the number of cracks. These measures were made looking at the polished side of the sample, using a microscope, every certain numbers of cycles.

In order to explain the stiffness increase, typical of the B type samples, the debonding of the aluminium tabs has been monitored with the microscope as well.

5.3.1 Number of cracks

To recognise and count the cracks, looking at the side of the sample with the microscope, is necessary to choose a correct magnification. A lower magnification reduces the time spent on the microscope to make the measurements but increase the risk of not recognizing all the cracks present on the surface. However, a higher magnification allows to recognise all the cracks, included the smallest ones, but the time spent to investigate all the side surface of the sample is higher. Using a high magnification can also lead to mismatch between cracks and scratches on the surface.

To better analyse the crack density, the side surface of the sample has been divided into three zones: center, left and right. The zones are delimited by the points in which the tabs are debonded from the composite. The center zone coincides with the free length of the sample. It means that at the beginning, for the B type, there is a 25 mm length center zone, that will grow during the fatigue life. However, for the D type, the Teflon tape is placed to obtain an initial free length of 70 mm. An illustration of the three zones of the sample’s side is shown in **Figure 5.22**.

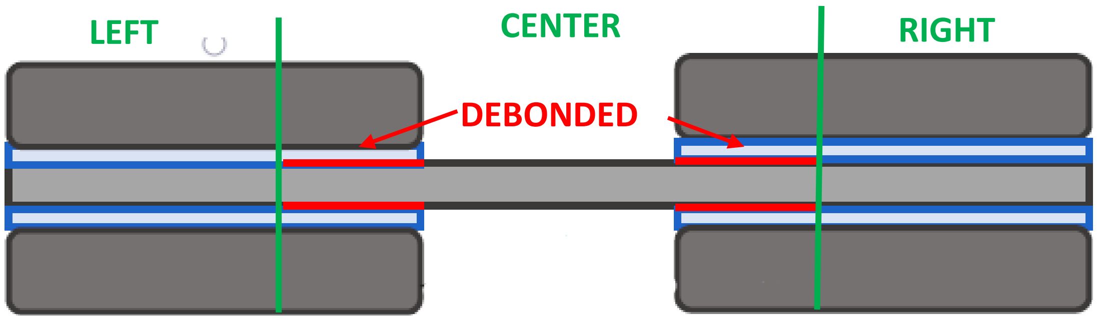

Figure 5.22: *Division of the side zones of the sample*

The objective of this analysis is to explain the stiffness behaviour. The load condition that returns the most representative results for the stiffness trend has been chosen: 70% of the maximum stress and 1Hz of frequency. The acquisition intervals have been chosen, based on the typical number of cycles at failure for this load condition. The average number of cycles at failure is 14000 cycles. The intervals have been chosen to investigate with more frequency at the beginning, where the crack density increases rapidly. The acquisitions intervals are presented in **Table 4** below.

Measurement intervals	
0	1000
1000	3000
3000	5000
5000	7000
7000	10000
10000	13000
13000	16000

Table 4*: Damage analysis measurements intervals*

5.3.1.1 B type crack density evolution

The “B23” type sample has been subjected to the cracks density measurements. The results of the analysis at the microscope are presented in **Table 5** below.

Cracks - Delaminations B23				
Measurement intervals		**Left**	**Right**	**Center**
	0	**0**	**0**	**0**
0	1000	0	0	0
1000	3000	0	0	0
3000	5000	delam	delam	4
5000	7000	delam	delam	6
7000	10000	delam	delam	200
10000	11207	failure at 11207 cycles		

***Table 5**: Cracks and delaminations measurements for B23 (load conditions: 70% of the maximum stress and 1Hz)*

As can be seen, the first damage appears after 5000 cycles. On the left and right side of the sample is possible to notice some delaminations and in the center zone of the sample, the first cracks start to grow. The dimension of the center zone is also increasing, due to the tabs debonding and it will be investigated in the next paragraph 5.3.2.

At 5000 cycles, the outer layer near the tabs fails, as can be seen in **Figure 5.23** below. It is probably due to an original defect or due to a stress concentration originated at the edge of the aluminium tab.

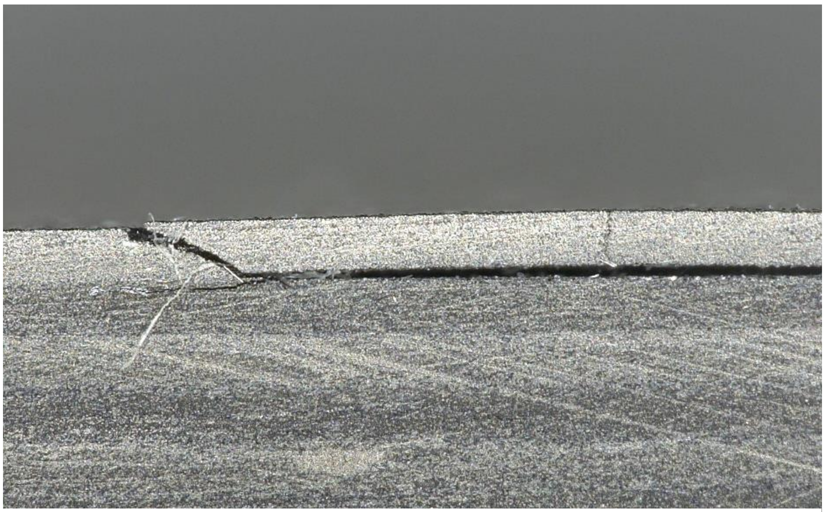

***Figure 5.23**: Outer layer fails at 5000 cycles for B23 sample*

At 7000 cycles the damage slightly increases. The number of delamination raise, as happened for the cracks. The cracks at this point begin to unite to form a bigger crack that cross several layers, as shown in **Figure 5.24** below.

Figure 5.24*: Cracks at 7000 cycles for "B23" sample*

At 10000 cycles the damage level is high, in the center zone there are about 200 cracks. The delaminations at the end of the sample have also increased. Below, **Figure 5.25** at a higher magnification and **Figure 5.26** at a higher magnification shows the damage at 10000 cycles.

Figure 5.25: *Cracks at 10000 cycles for "B23" sample*

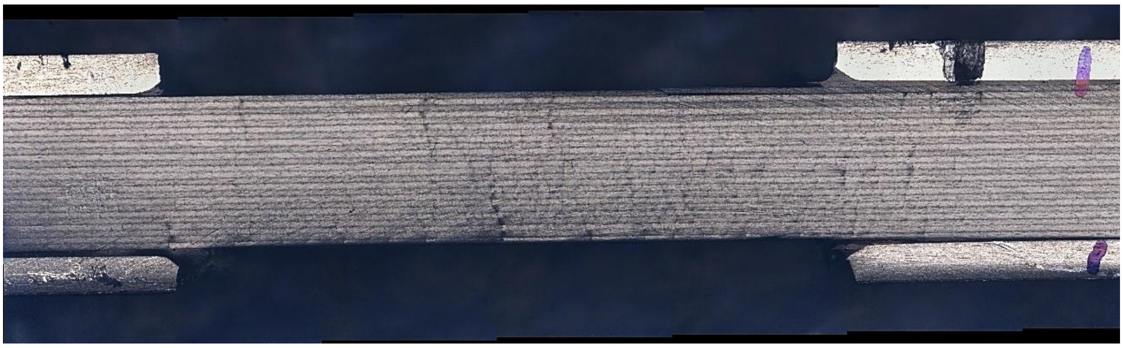

Figure 5.26: *Cracks at 10000 cycles for "B23" sample at a lower magnification*

The sample reaches the failure at 11207 cycles. This value is in line with the other 70% max stress's B type samples fatigue life.

Analysing the side of the sample at the microscope, after the failure, is possible to affirm that the failure was pure compressive, as can be seen in **Figure 5.27** below.

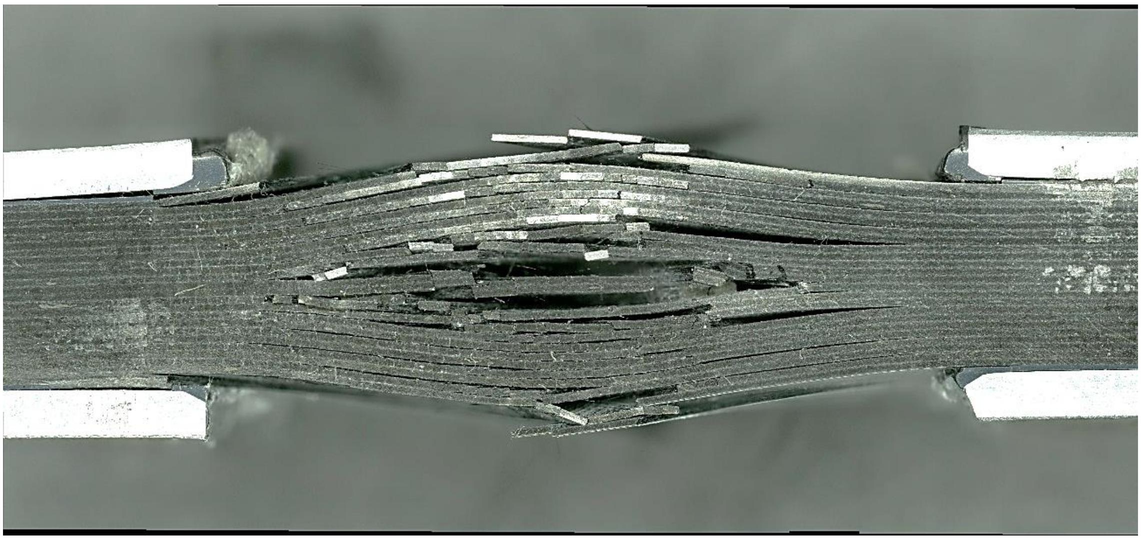

***Figure 5.27**: Microscope image at the failure of "B23" sample (11207 cycles)*

The final failure of the sample is reached when the two center layers break by pure compression. It consequently induces the instability of the adjacent layers and the failure of the more external ones. This effect increases fast as chain effect and involves in a real explosion of the gauge length of the specimen. This failure mode is called pure compressive failure and is accepted by the normatives. This failure mode is difficult to reach due to many complex phenomena involved in compressive loading of CFRPs and is typical of a successful compressive test.

In **Figure 5.28** the stiffness evolution is plotted against the number of cracks. Has to be mentioned that the stiffness behaviour of the "B23" is slightly different than the usual trend for 70% of the maximum load and 1 Hz of frequency, shown in **Figure 5.18** before. In this case, an increasing of the stiffness is not present. This is probably due to the frequent removal of the sample from the machine that results in a redistribution of the strain on the gauge length of the sample.

It is possible to see how the stiffness degradation is related to the number of cracks. Another parameter that influence the stiffness trend is the free length. It will be investigated in the next paragraph (5.3.2).

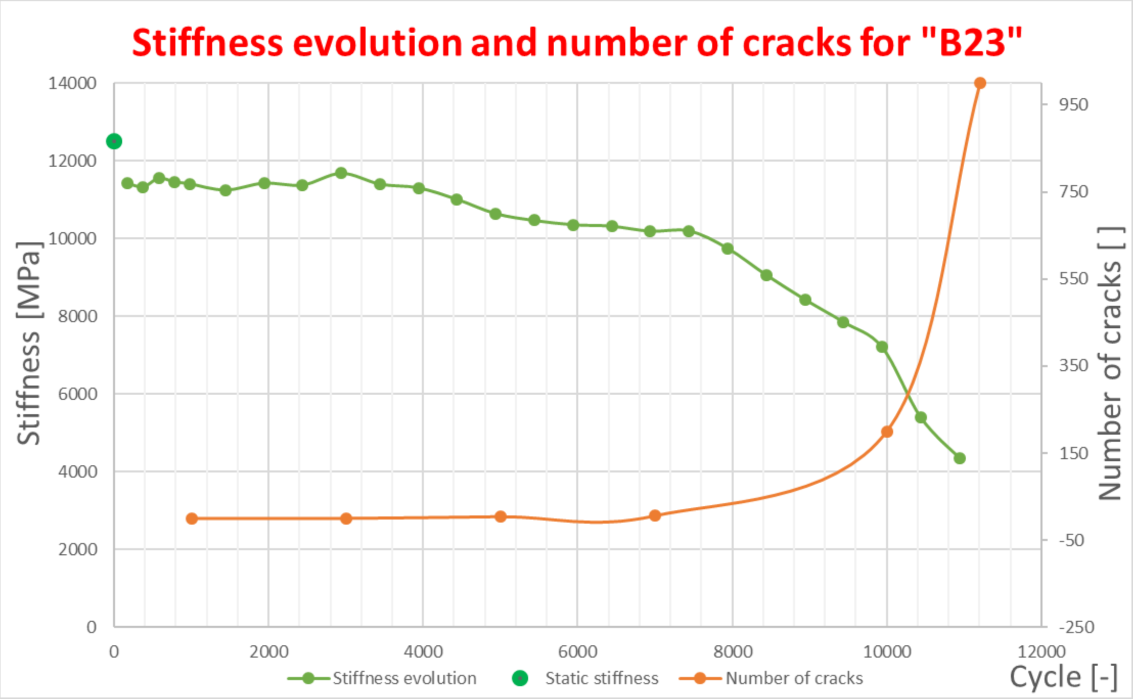

***Figure 5.28**: Stiffness evolution and number of cracks for “B23”*

5.3.1.2 D type crack density evolution

The “D16” type sample has been subjected to the cracks density measurements. The results of the analysis at the microscope are presented in **Table 6** below

Cracks - Delaminations D16				
Measurement intervals		**Left**	**Right**	**Center**
	0	0	0	0
0	1000	0	0	0
1000	3000	0	0	0
3000	5000	0	0	0
5000	7000	delaminations	delaminations	23
7000	10000	delaminations	delaminations	145
10000	13000	delaminations 5 cracks	delaminations 17 cracks	500
13000	14822	Failure at 14822 cycles		1000

***Table 6**: Cracks and delaminations measurements for D16 (load conditions: 70% of the maximum stress and 1Hz)*

The first damage appears after 7000 cycles. On the left and right side of the sample is possible to notice some delaminations and in the center zone of the sample the first cracks start to grow. The dimension of the center zone in this case is not increasing, due to the partially debonded tabs and it will be investigated in the next paragraph 5.3.2.

At 10000 cycles the number of cracks in the center zone increases, the same as the delaminations present on the ends of the sample.

Until this point, the damage evolution is similar to the “B23” sample, presented before. Starting from 13000 cycles some cracks at the ends of the sample appears. This did not happen on “B23” sample, on which there was only delaminations. The cracks in the center zone are much increased to the value of about 500 cracks.

In **Figure 5.29** and **Figure 5.30** below, the cracks observed at the microscope at 13000 cycles are shown.

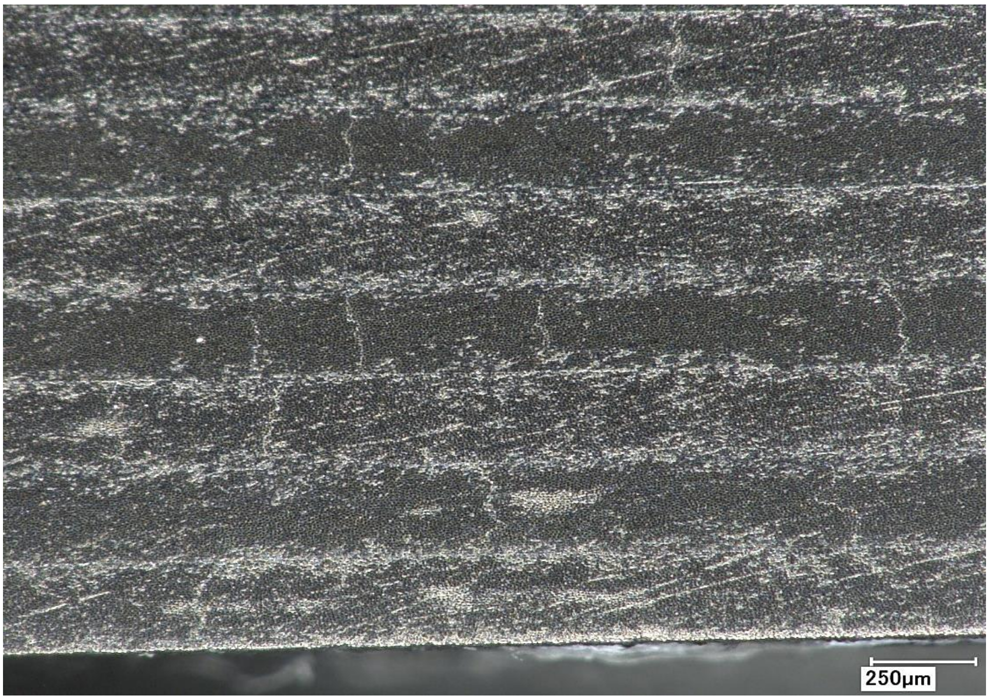

***Figure 5.29**: Cracks at 13000 cycles for "D16" sample*

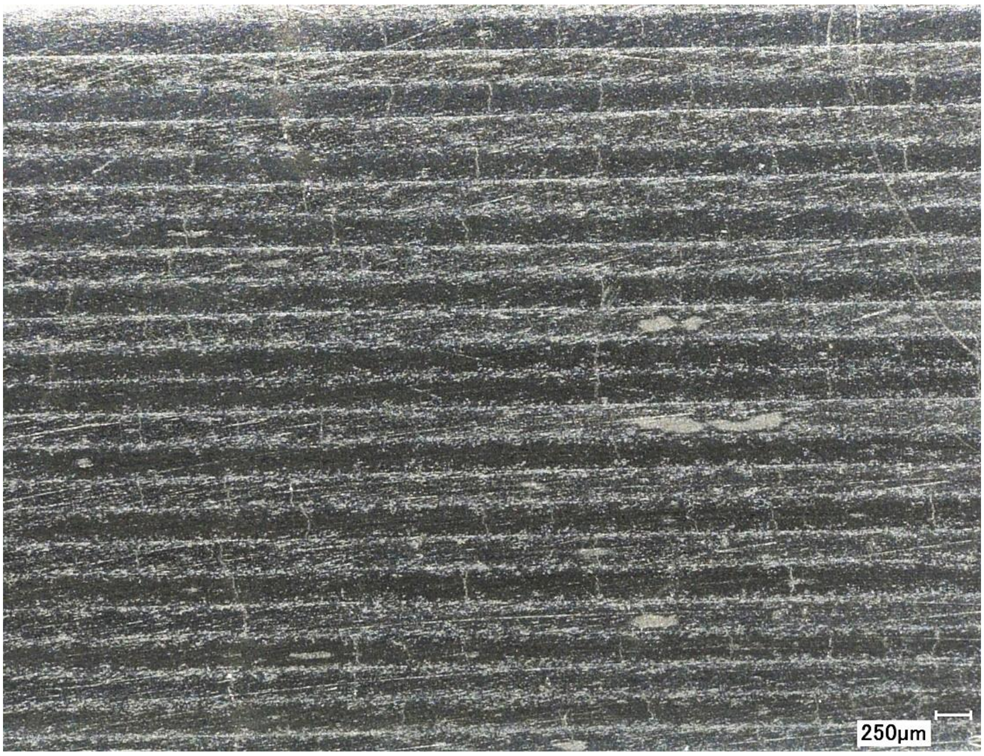

***Figure 5.30**: Cracks at 13000 cycles for "D16" sample at a lower magnification*

The sample reaches the failure at 14822 cycles. This value is in line with the other 70% max stress's D type samples fatigue life.

Analysing the side of the sample at the microscope, after the failure, is possible to affirm that the failure was pure compressive. The final failure mode mechanism is the same of the B type explained before in 5.3.1.1.

In **Figure 5.31** the stiffness evolution is plotted against the number of cracks. It is possible to see how the stiffness degradation is related to the number of cracks.

In the first part of the fatigue life, the stiffness remains almost constant, as it happens for the cracks number. Around 7000 cycles, when the first cracks and delaminations appears on the material, the stiffness start to decrease. Over this point, the amount of cracks increases exponentially, while the stiffness decreases rapidly until the sample reaches the failure. Consequently, it is possible to affirm that the number of cracks and the stiffness degradation are correlated. Also delaminations plays a role in stiffness degradation. They are directly correlated to the cracks number, but it is more complicated to quantify them.

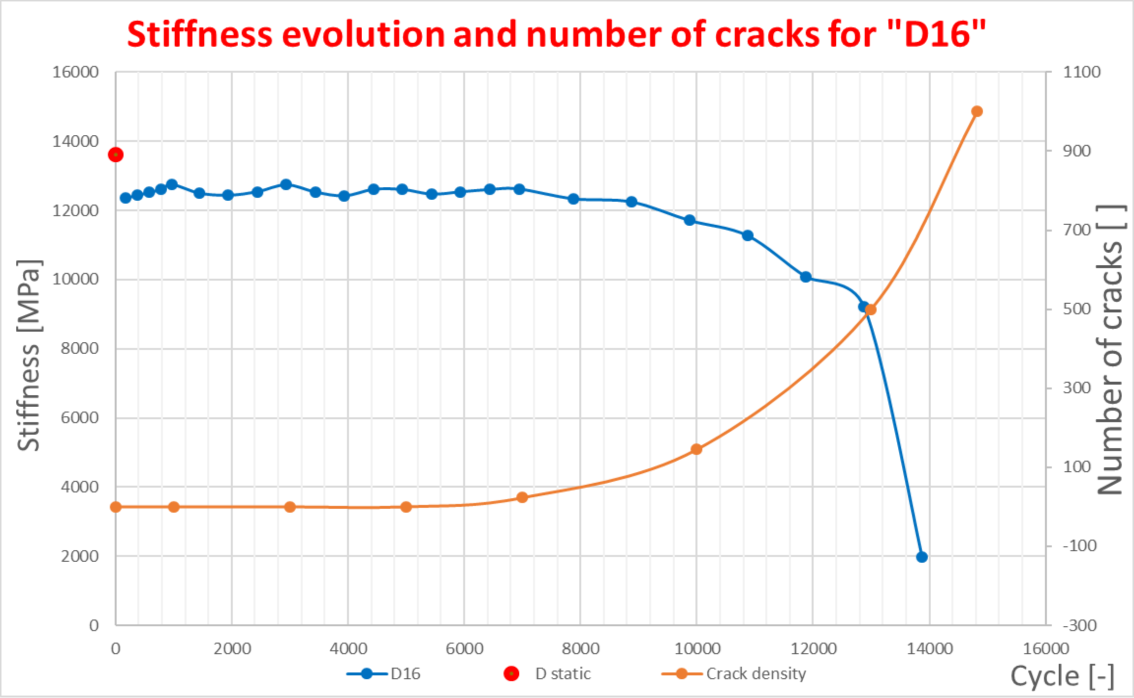

***Figure 5.31**: Stiffness evolution and number of cracks for "D16"*

5.3.2 Free length

The procedure to measure the real free length, looking at the side of the specimen, using the microscope is similar to what was done for for the cracks and delaminations measurements.

To locate with a certain precision the point in which the tabs are debonded from the composite material, is necessary to use a high magnification. Once the four points have been recognised (one debonding point for each tab), it has been marked with a very fine tip pen. After that, removing the sample from the microscope, a caliper has been used to measure the two free length (one length for each tab couple). The final measure of the free length is the average between the two measures.

5.3.2.1 B type free length evolution

The results of the free length analysis at the microscope for the "B23" sample are presented in **Table 7** below.

Cracks - Delaminations - Free length							
Measurement intervals		**Free length 1 [mm]**	**Free length 2 [mm]**	**Average free length [mm]**	**Left**	**Right**	**Center**
	0	25	25	**25**	**0**	**0**	**0**
0	1000	31	32	**31,5**	0	0	0
1000	3000	32	34	**33**	0	0	0
3000	5000	40	42	**41**	delam	delam	4
5000	7000	47	49	**48**	delam	delam	6
7000	10000	47	49	**48**	delam	delam	200
10000	11207	49	49	**49**	failure at 11207 cycles		

Table 7: *Cracks, delaminations and free length measurements for B23 (load conditions: 70% of the maximum stress and 1Hz)*

Contrary to the cracks and delaminations number analysed before, the free length for the B type start to increase immediately after the beginning of the fatigue test. The original free length of the specimen is 25 mm with the tabs completely bonded.

In **Figure 5.32** below, the tabs debonding at 1000 cycles is shown. The debonding start at the tabs edge (adjacent to the gauge length), due to the stress concentration present in this point. The debonding propagates 3,25 mm and consequently the free length reaches the value of 31,5 mm.

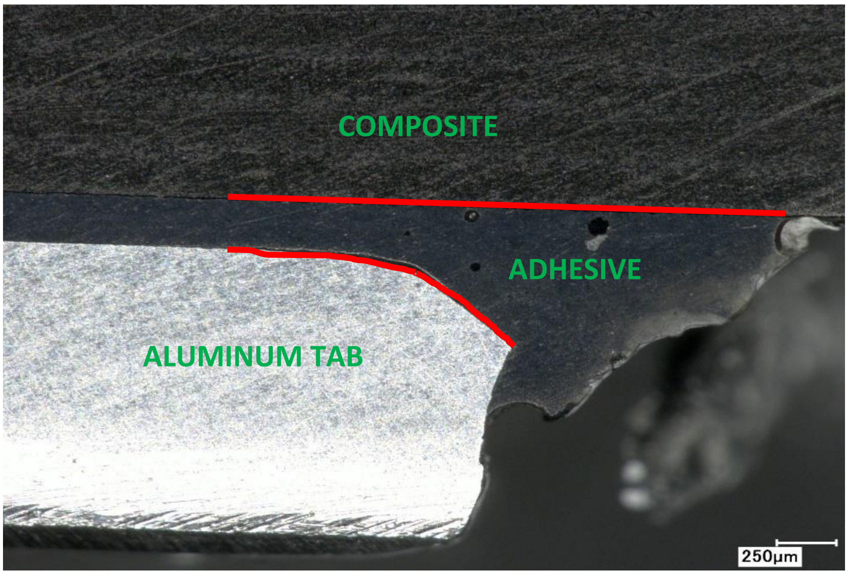

Figure 5.32: *Tabs debonding at 1000 cycles for "B23"*

In **Figure 5.33** below, the tabs debonding at 3000 cycles is shown. The debonding continue to propagate between the adhesive and the aluminium tabs.

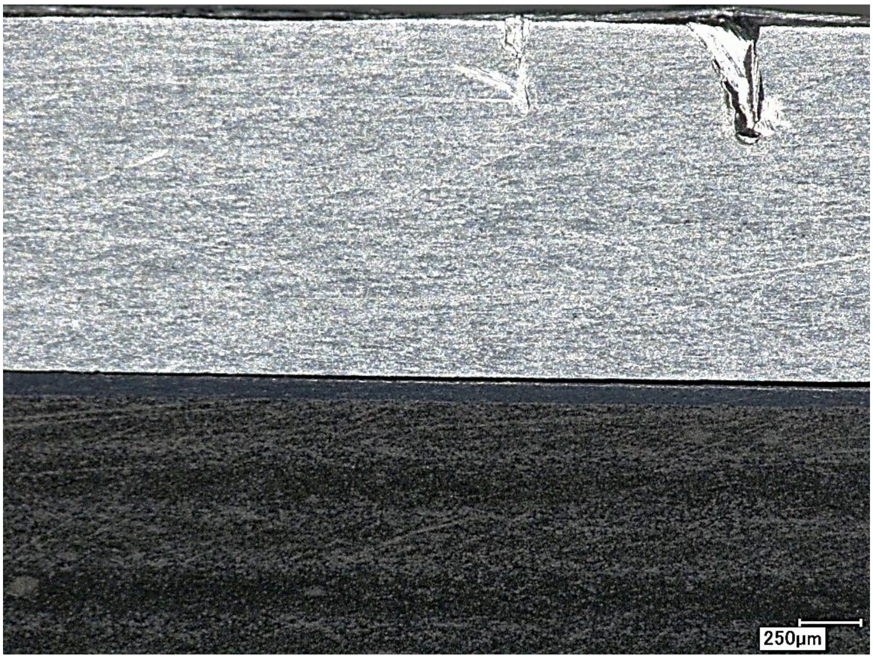

Figure 5.33*: Tabs debonding at 3000 cycles for "B23"*

The free length increases almost linearly until 7000 cycles. Over this point the value remains constant at the value of 49mm until the sample reaches the failure. After the sample's failure, mechanically removing the tabs and measuring the free length with the caliper is possible to confirm that the final free length reached is 49mm, as is shown in **Figure 5.34** below.

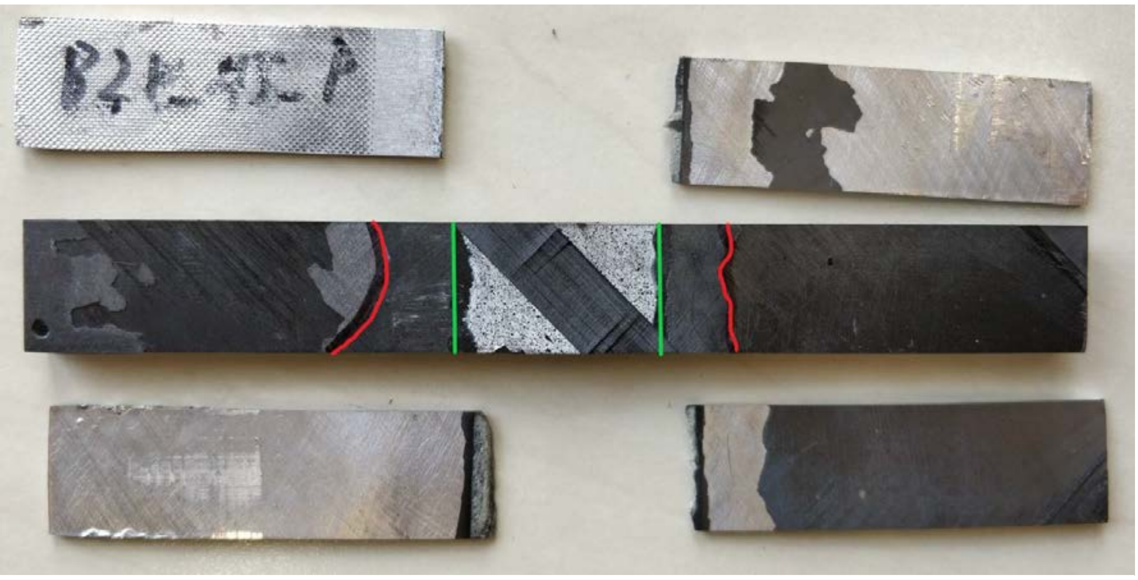

***Figure 5.34**: Tabs debonding surface after failure of "B23" specimen*

In **Figure 5.35** the stiffness evolution is plotted against the free length. As explained before, the stiffness evolution of the B23 is slightly different than the usual trend at the same load conditions and an increasing of the stiffness is not present.

Is visible from the graph that after 7000 cycles the free length is not increasing, while the stiffness is still decreasing. This is since the stiffness behaviour is function of both free length and cracks number. Relating these two parameters like the cracks number and the delaminations (representative of the internal damage of the material) to the stiffness behaviour (macroscopic property of the material), is difficult and complex.

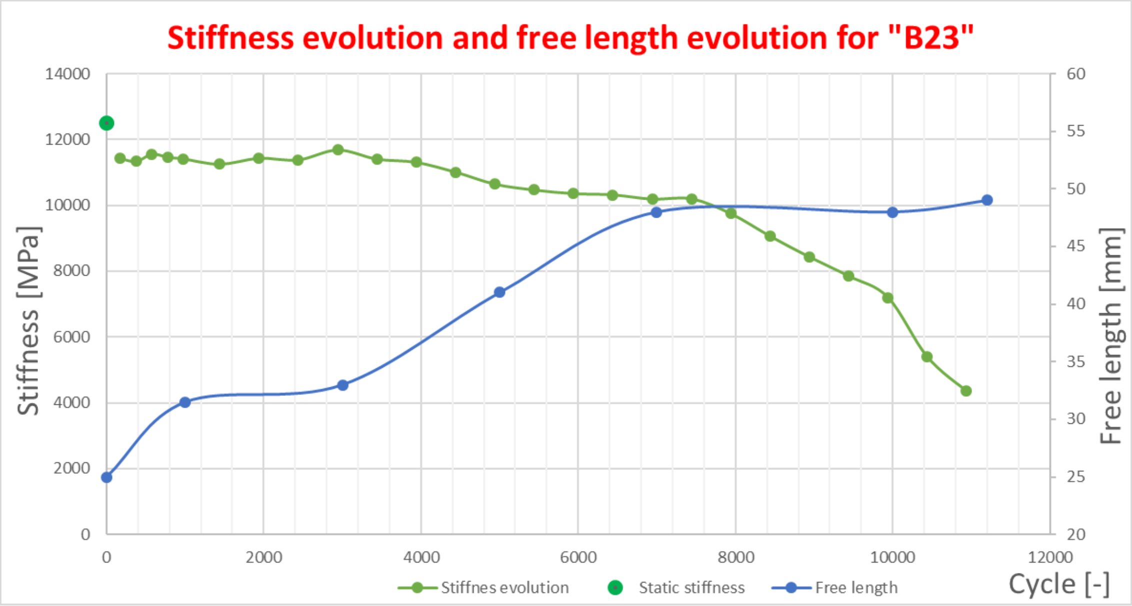

***Figure 5.35**: Stiffness evolution and free length for “B23”*

5.3.2.2 D type free length evolution

The results of the free length analysis at the microscope for the “D16” sample are presented in **Table 8** below.

Cracks - Delaminations - Free length								
Measurement intervals		**Free lenght 1 [mm]**	**Free lenght 2 [mm]**	**Average free length [mm]**	**Left**	**Right**	**Center**
	0	70	70	**70**	0	0	0
0	1000	70	70	**70**	0	0	0
1000	3000	70	70	**70**	0	0	0
3000	5000	70	70	**70**	0	0	0
5000	7000	70	70	**70**	delaminations	delaminations	23
7000	10000	70	70	**70**	delaminations	delaminations	145
10000	13000	70	70	**70**	delaminations 5 cracks	delaminations 17 cracks	500
13000	14822	**70**	**70**	**70**	failure at 14822 cycles		

***Table 8:** Cracks, delaminations and free length measurements for D16 (load conditions: 70% of the maximum stress and 1Hz)*

As can be seen from the table below, for the D type sample the tabs are not debonding during the fatigue life. It is since the strain field for the D type is more uniform. The load is transferred from the clamps, through the aluminium tabs and into the composite material without stress concentrations on the bonding surface. It induces a non debonding of the tabs, characteristic of the D type sample.

After the sample's failure, mechanically removing the tabs and measuring the free length with the caliper is possible to confirm that a debonding of the tabs is not present and the free length is constant at the value of 70mm, as is shown in **Figure 5.36** below.

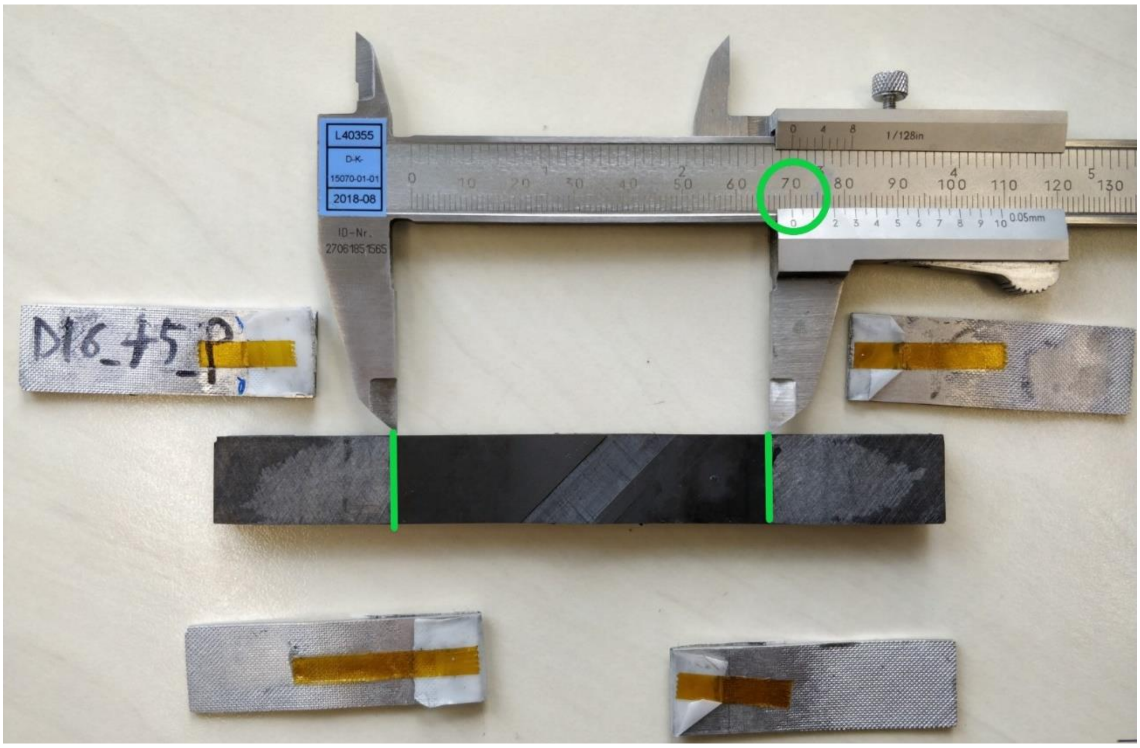

Figure 5.36*: Tabs debonding surface after failure of "D16" specimen*

This is the reason why for the D type, the stiffness degradation is better related with the cracks numbers (analysed before in 5.3.1.2), compared with the B type.

6 CONCLUSIONS

6.1 Conclusions

A **literature study** (Chapter 2) concludes that fatigue failure of unidirectional composite materials is a complex phenomenon. It involves several failure modes and multiple scales on which the damage occurs. Experimental efforts are often limited to T-T loading, and where results are presented, they are mainly based on S-N curve generation. No standards exist for the measurement of the evolution of properties such as stiffness and permanent strain, even though these could be valuable in modeling. DIC was identified as a potentially powerful method for measuring these properties, also under fatigue tests.

The **experimental set-up** is shown in chapter 4. The system uses DIC cameras to capture images during fatigue tests and combines it with the output analog signals from the machine to obtain relevant results. To characterize the fatigue behavior efficiently, the system measures signals and take images for a number of cycles at a high acquisition rate, then wait for a time period and repeat this.

To perform tests involving compression, **specimen design** requires careful consideration. This is discussed in chapter 4 (4.2). Buckling prevention is done through the design of specimens, with a free length short enough to prevent buckling. This induces stress concentrations in proximity of the area of interests, involving several problems of the behaviour of macroscopic properties like the stiffness. These problems encountered by S. Walraet (explained in 3.1) leads to develop a new specimen design, implemented by P. H. Jimenez (explained in 3.2) and also used for this project. In order to analyse the possible benefits of using this new type of sample design, several aspects have been compared to see if this specimen design can be an alternative of the classical anti-buckling guide provided by the normatives.

A test program was performed on unidirectional carbon-epoxy material with a stacking sequence of $[+45/-45]_{6S}$. The results are presented and discussed in chapter 5.

From the **static tests** is possible to conclude:

- From the **stress-strain curves** a highly non-linear behaviour with large deformation is visible. It is not possible to distinguish a clear different trend of the curves for the two different specimen geometries.
- Analysing the **maximum compressive stress**, no difference between the two sample geometries can be observed.
- An investigation of the **strain field** has been performed during a static test, on both sample types, in order to correlate how it can influence some macroscopic properties that will be further analysed.
- The calculation of the **stiffness** from the static tests has brought results not so clear. To improve the reliability and validity of the tests, the results from P. H. Jimenez have been included to the other results. It brings to affirm with a certain assurance that the stiffness of the D type is higher than the B type.

From the **fatigue tests** is possible to conclude:

- The **temperature** was monitored throughout every experiment. For $[+45/-45]_{6S}$ laminates, shearing motion of fibers resulted in heating of the material. To avoid this heating, frequency was adapted for highly loaded tests. Due to the friction between the partially debonded tabs and the composite material, the D type samples reaches higher temperatures, but always within acceptable limits for all the tests.
- Plotting the **S-N curves** for both sample geometries shows how the behaviour of the curves are similar. A unique curve can be plotted for all the tests.
- Plotting the **stress-strain** graphs is possible to observe the stress-strain cycles. It is evident, for the B type, how the slope of the cycles is increasing during the test, especially on the first part. This is not true for the D type behaviour, in which the slope of the cycles is decreasing. This is representative of the stiffness behaviour.

Another parameter that can be focused looking at the stress-strain cycles is the area of the cycles. It is related to the hysteresis of the material and it is representative of the damage level of the material. The larger is the area, the higher is the damage inside the material and the heating generated inside. This is also related to visco-elasticity of the material.

- The **permanent strain** is a macroscopic property caused by a load that overpass the limit of the material. It produces a permanent change in the shape or size of a solid body without fracture, resulting from the application of sustained stress beyond the elastic limit. It is defined in this work as the difference in strain at the smallest compressive load applied in cycle x, compared to the strain at the start of the first fatigue cycle (with a compressive load of 10% σ_{max} already applied). It is possible to affirm that the general trend of the curves is similar for the different stress levels. The first part of the curve has a linear decreasing, in which the slope of the curve is function of the stress applied. Higher is the stress and higher is the slope of the first part of the curve, and vice versa. Close to the failure of the sample, the permanent strain is increasing very fast, until it reaches the breaking.
- The **stiffness evolution** for the B type sample is characterised by an increasing of the stiffness. It is also possible to affirm that the peak of the stiffness is not function of the stress level applied for the B type. However, for the D type, it is possible to confirm that the curves generally remain constant for the most part of the fatigue life and close to the failure, the stiffness decrease to zero. The value of the stiffness in the constant stretch of the curve is function of the load applied at the samples. The lower the load and the higher the stiffness in the constant stretch of the curve.

From the **damage analysis** is possible to conclude:

- The number of cracks and the stiffness behaviour for the B type are related, but not directly. To describe the behaviour of the stiffness for the B type is also necessary to relate the free length (which is increasing during the fatigue life).
- For the D type, the free length is constant during the fatigue life. It means that the stiffness behaviour is directly correlated with the cracks number.

6.2 Recommendations for further work

This research topic has yielded interesting results already. Unfortunately, time is limited when performing a master thesis. The following recommendations can be of interest for future research:

- In order to better evaluate the value of the stiffness from the static tests, more **static tests** could have been done.
- For this test series, two laminates have been tested, at different stress levels and at different frequencies. This large number of variables tested in a limited number of fatigue tests makes drawing conclusions confidently difficult in some cases. If time and resources would allow for it, performing more experiments could **increase the confidence** of the data.
- For the fatigue tests, more than one value of the **frequency** of the sinewaves has been used. The effect of different values of the frequency on the fatigue behaviour are unknown. Further analysis could be done in future works, to better investigate the influence of this parameter.
- To further investigate the stiffness evolution and relate it with the damage accumulation on the material, it can be of interest to microscopically **investigate crack behaviour throughout fatigue life**, but with a higher number of measurement intervals and more detailed analysis of the damage, compared to the analysis done in this project.
- Some tests with **stacking sequence of [0/90]** can be of interest to microscopically investigate the behaviour during the fatigue life and relate it to the behaviour of $[+45/-45]_{6S}$.
- The DIC measurement system was set up with two cameras. However, it can be interesting to use **three cameras**, adding a camera on the side of the sample. Using 3D DIC on outer layers could potentially capture the extent of delaminated areas for a more in-depth analysis of the delaminations and cracks on the side of the sample.

7 APPENDIX

7.1 Macros

In this section, the macros written in Visual Basic for applications, implemented on the Excel© worksheets containing the data from the tests, are collected:

7.1.1 Strain Evolution, Stress-Strain curves, Permanent strain

```
Sub Stiffness_Evolution()
' Stiffness_Evolution Macro

    Range("B10").Activate

    Dim i As Long
    Dim j As Integer
    Dim s As Integer
    Dim t As Integer

    Dim Stiffness() As Variant
    Dim Stif As Double

    Dim Stress(1) As Double
    Dim Strain(1) As Double
    Dim minLoad As Double
    Dim maxLoad As Double
    Dim minStress As Double
    Dim maxStress As Double
    Dim idxmin As Integer
    Dim idxmax As Integer
    Dim minStrain As Double
    Dim maxStrain As Double

    i = ActiveCell.Value
    j = 1
    s = Range("S6").Value
    t = Round(Range("S4").Value, 0)

    For j = 1 To s

        minLoad = WorksheetFunction.Min(ActiveCell.Offset(0, 4).Range("A1:A" & t).Value)
        idxmin = WorksheetFunction.VLookup(minLoad, ActiveCell.Offset(0, 4).Range("A1:B" & t), 2, False)
        maxLoad = WorksheetFunction.Max(ActiveCell.Offset(0, 4).Range("A1:A" & t).Value)
```

```
        idxmax = WorksheetFunction.VLookup(maxLoad, ActiveCell.Offset(0, 4).Range("A1:B" & t), 2, False)

        minStress = ActiveCell.Offset(0, 21).Range("A" & (idxmin - t * (j - 1))).Value
        maxStress = ActiveCell.Offset(0, 21).Range("A" & (idxmax - t * (j - 1))).Value

        minStrain = ActiveCell.Offset(0, 19).Range("A" & (idxmin - t * (j - 1))).Value
        maxStrain = ActiveCell.Offset(0, 19).Range("A" & (idxmax - t * (j - 1))).Value

        Stress(0) = minStress
        Stress(1) = maxStress

        Strain(0) = minStrain
        Strain(1) = maxStrain

        Stiffness = WorksheetFunction.LinEst(Stress, Strain)
        Stif = Round(Stiffness(1), 0)


        ActiveSheet.ChartObjects("Chart 1").Activate
        ActiveChart.SeriesCollection.NewSeries
        ActiveChart.SeriesCollection(j).Name = "Cycle " & Round(ActiveCell.Value, 0)
        ActiveChart.FullSeriesCollection(j).XValues = ActiveCell.Value
        ActiveChart.FullSeriesCollection(j).Values = Stif

        ActiveCell.Offset(0, 23).Range("A1").Activate
        ActiveCell.Value = Stif
        ActiveCell.Offset(t, -23).Range("A1").Activate

        i = ActiveCell.Value

    Next j
    Range("B10").Activate

End Sub
```

7.1.2 Stiffness evolution

```
Sub Stiffness_Evolution()
' Stiffness_Evolution Macro

    Range("B10").Activate

    Dim i As Long
    Dim j As Integer
    Dim s As Integer
    Dim t As Integer

    Dim Stiffness() As Variant
    Dim Stif As Double

    Dim Stress(1) As Double
    Dim Strain(1) As Double
```

```
    Dim minLoad As Double
    Dim maxLoad As Double
    Dim minStress As Double
    Dim maxStress As Double
    Dim idxmin As Integer
    Dim idxmax As Integer
    Dim minStrain As Double
    Dim maxStrain As Double

    i = ActiveCell.Value
    j = 1
    s = Range("S6").Value
    t = Round(Range("S4").Value, 0)

    For j = 1 To s

        minLoad = WorksheetFunction.Min(ActiveCell.Offset(0, 4).Range("A1:A" & t).Value)
        idxmin = WorksheetFunction.VLookup(minLoad, ActiveCell.Offset(0, 4).Range("A1:B" & t), 2, False)
        maxLoad = WorksheetFunction.Max(ActiveCell.Offset(0, 4).Range("A1:A" & t).Value)
        idxmax = WorksheetFunction.VLookup(maxLoad, ActiveCell.Offset(0, 4).Range("A1:B" & t), 2, False)

        minStress = ActiveCell.Offset(0, 21).Range("A" & (idxmin - t * (j - 1))).Value
        maxStress = ActiveCell.Offset(0, 21).Range("A" & (idxmax - t * (j - 1))).Value

        minStrain = ActiveCell.Offset(0, 19).Range("A" & (idxmin - t * (j - 1))).Value
        maxStrain = ActiveCell.Offset(0, 19).Range("A" & (idxmax - t * (j - 1))).Value

        Stress(0) = minStress
        Stress(1) = maxStress

        Strain(0) = minStrain
        Strain(1) = maxStrain

        Stiffness = WorksheetFunction.LinEst(Stress, Strain)
        Stif = Round(Stiffness(1), 0)


        ActiveSheet.ChartObjects("Chart 1").Activate
        ActiveChart.SeriesCollection.NewSeries
        ActiveChart.SeriesCollection(j).Name = "Cycle " & Round(ActiveCell.Value, 0)
        ActiveChart.FullSeriesCollection(j).XValues = ActiveCell.Value
        ActiveChart.FullSeriesCollection(j).Values = Stif

        ActiveCell.Offset(0, 23).Range("A1").Activate
        ActiveCell.Value = Stif
        ActiveCell.Offset(t, -23).Range("A1").Activate

        i = ActiveCell.Value

    Next j
    Range("B10").Activate

End Sub
```

8 BIBLIOGRAPHY

[1] Fleck, N. A. "Compressive failure of fiber composites, "*Advances in applied mechanics*" 33.6 (1997): 7.

[2] Quaresimin M. *Introduzione alla progettazione con materiali compositi,* 2009, Vicenza, Italy

[3] Naik, N. K., and Rajesh S. Kumar. "Compressive strength of unidirectional composites: evaluation and comparison of prediction models, "*Composite structures*" 46.3 (1999): 299-308.

[4] Jumahat, A., et al. "Fracture mechanisms and failure analysis of carbon fibre/toughened epoxy composites subjected to compressive loading "*Composite structures"* 92.2 (2010): 295-305

[5] Davidson, Paul, and Anthony M. Waas. "The effects of defects on the compressive response of thick carbon composites: an experimental and computational study "*Composite Structures"* 176 (2017): 582-596.

[6] Matsuo, Tsuyoshi, and Kazuro Kageyama. "Compressive failure mechanism and strength of unidirectional thermoplastic composites based on modified kink band model, "*Composites Part A: Applied Science and Manufacturing"* 93 (2017): 117-125.

[7] Wei, S. U. N., et al. "Compressive failure analysis of unidirectional carbon/epoxy composite based on micro-mechanical models, "*Chinese Journal of Aeronautics*" 30.6 (2017): 1907-1918.

[8] Hull, Derek, and Trevor W. Clyne, "*An introduction to composite materials*" Cambridge university press, 1996.

[9] Agarwal, Bhagwan D., Lawrence J. Broutman, and K. Chandrashekhara, *"Analysis and performance of fiber composites",* John Wiley & Sons, 2017.

[10] Mallick, Pankar K, *"Fiber-reinforced composites: materials, manufacturing, and design"* CRC press, 2007

[11] Sevenois, R. D. B., and Wim Van Paepegem, "Fatigue damage modeling techniques for textile composites: review and comparison with unidirectional composite modeling techniques, "*Applied mechanics reviews"* 67.2 (2015)

[12] Quaresimin, Marino, Luca Susmel, and Ramesh Talreja. "Fatigue behaviour and life assessment of composite laminates under multiaxial loadings, "*International Journal of Fatigue*" 32.1 (2010): 2-16.

[13] Hsiao, H. M., and I. M. Daniel. "Effect of fiber waviness on stiffness and strength reduction of unidirectional composites under compressive loading "*Composites science and technology*" 56.5 (1996): 581-593.

[14] Ayranci, Cagri, and Jason Carey. "2D braided composites: a review for stiffness critical applications", *Composite Structures* 85.1 (2008): 43-58.

[15] Feraboli, Paolo, and Attilio Masini, "Development of carbon/epoxy structural components for a high performance vehicle", *Composites Part B: Engineering* 35.4 (2004): 323-330.

[16] Degrieck, Joris, and Wim Van Paepegem, "Fatigue damage modeling of fibre-reinforced composite materials, "*Applied mechanics reviews*" 54.4 (2001): 279-300.

[17] Quaresimin, M. "50th anniversary article: multiaxial fatigue testing of composites: from the pioneers to future directions." *Strain* 51.1 (2015): 16-29.

[18] Pinho, Silvestre T., Paul Robinson, and Lorenzo Iannucci. "Fracture toughness of the tensile and compressive fibre failure modes in laminated composites" C*omposites science and technology* 66.13 (2006): 2069-2079.

[19] Jones, Robert M. *Mechanics of composite materials*. CRC press, 2014.

[20] Ladeveze, Pierre, and E. LeDantec. "Damage modelling of the elementary ply for laminated composites" *Composites science and technology* 43.3 (1992): 257-267

[21] Gamstedt, E. K., and B. A. Sjögren. "Micromechanisms in tension-compression fatigue of composite laminates containing transverse plies "*Composites Science and Technology* 59.2 (1999): 167-178.

[22] Schultheisz, Carl R., and Anthony M. Waas. "Compressive failure of composites, part I: testing and micromechanical theories" *Progress in Aerospace Sciences* 32.1 (1996): 1-42.

[23] Budiansky, Bernard, and Norman A. Fleck. "Compressive failure of fibre composites", *Journal of the Mechanics and Physics of Solids* 41.1 (1993): 183-211.

[24] Hull, Derek, and Yi Bing Shi. "Damage mechanism characterization in composite damage tolerance investigations" *Composite Structures* 23.2 (1993): 99-120.

[25] Torquato, S. "Modeling of physical properties of composite materials" *International Journal of Solids and Structures* 37.1-2 (2000): 411-422.

[26] Erkendirci, Ö. Faruk, and Ahmet Avci. "Effect of inclined cracks on the fatigue and fracture behavior of woven steel/reinforced polyethylene composite." *Journal of Reinforced Plastics and Composites* 29.12 (2010): 1775-1792.

[27] Holmes, Mark. "Carbon fibre reinforced plastics market continues growth path" *Reinforced Plastics* 57.6 (2013): 24-29.

[28] Sevenois Ruben, et al. "Influence of tab debonding on measured stiffness evolution in compression-compression fatigue testing of short gauge length cupons" *7th International Conference on Fatigue of Composites,* European Society on Composite Materials, 2018.

[29] Walraet S., "*Compression-Compression and Tension-Compression Fatigue of Woven Carbon-Epoxy Composites",* Delft University of Technology, (2017).

[30] Jimenez P.A.H., "The effect of partially debonded tabs on the compressive stress-strain curve of angle-ply laminates", Ghent University, 2018

[31] Carraro, P. A., and M. Quaresimin. "A damage based model for crack initiation in unidirectional composites under multiaxial cyclic loading" *Composites Science and Technology* 99 (2014): 154-163.

[32] Mao, H., and S. Mahadevan. "Fatigue damage modelling of composite materials." *Composite Structures* 58.4 (2002): 405-410.

[33] Garg, Amar C. "Delamination—a damage mode in composite structures." *Engineering Fracture Mechanics* 29.5 (1988): 557-584.

[34] Wu, Fuqiang, and WeiXing Yao. "A fatigue damage model of composite materials." *International Journal of Fatigue* 32.1 (2010): 134-138.

[35] Ladeveze, Pierre, and E. LeDantec. "Damage modelling of the elementary ply for laminated composites." *Composites science and technology* 43.3 (1992): 257-267.

[36] Sevenois, R. D. B. (2018). *“Models for Intraply Damage and Strength Prediction of Unidirectional and Woven Composites under Static and Fatigue Loading in Tension and Compression.”* Ghent University A. P. Vassilopoulos and T. Keller, Fatigue of Fiber-Reinforced Composites, edited by S. S. Media (Springer-Verlag, 2011).

[37] Hodgkinson, John M., ed. *Mechanical testing of advanced fibre composites*. Elsevier, 2000.

[38] Besseghini, Eurosia. *Caratterizzazione meccanica a compressione di un composito unidirezionale mediante attrezzatura CLC*. Diss. 2011.

[39] Colombo, C., L. Vergani, and M. Burman. "Static and fatigue characterization of new basalt fibre reinforced composites." *Composite structures* 94.3 (2012): 1165-1174

[40] Shah, Darshil U., et al. "Fatigue life evaluation of aligned plant fibre composites through S–N curves and constant-life diagrams." *Composites Science and Technology* 74 (2013): 139-149

[41] Slaughter, William S., Jianqiang Fan, and Norman A. Fleck. "Dynamic compressive failure of fiber composites." *Journal of the Mechanics and Physics of Solids* 44.11 (1996): 1867-1890.

[42] Mandell, John F., and Daniel D. Samborsky. *DOE/MSU composite material fatigue database: test methods, materials, and analysis*. No. SAND-97-3002. Sandia National Labs., Albuquerque, NM (United States), 1997.

[43] Chaterjee, S., D. F. Adams, and Donald W. Oplinger. *Test Methods for Composites: A Status Report. Volume 2. Compression Test Methods*. MATERIALS SCIENCES CORP BLUE BELL PA, 1993.

[44] ASTM D3410 / D3410M-16, Standard Test Method for Compressive Properties of Polymer Matrix Composite Materials with Unsupported Gage Section by Shear Loading, ASTM International, West Conshohocken, PA, 2016

[45] Adams, D. F., and E. Q. Lewis. "Influence of specimen gage length and loading method on the axial compressive strength of a unidirectional composite material." *Experimental Mechanics* 31.1 (1991): 14-20.

[46] ASTM D695-15, Standard Test Method for Compressive Properties of Rigid Plastics, ASTM International, West Conshohocken, PA, 2015

[47] Quaresimin M. “Introduzione alla progettazione con materiali compositi” Course slides, 2018

[48] ASTM D5467 / D5467M-97(2017), Standard Test Method for Compressive Properties of Unidirectional Polymer Matrix Composite Materials Using a Sandwich Beam, ASTM International, West Conshohocken, PA, 2017

[49] ASTM D6641 / D6641M-16e1, Standard Test Method for Compressive Properties of Polymer Matrix Composite Materials Using a Combined Loading Compression (CLC) Test Fixture, ASTM International, West Conshohocken, PA, 2016

[50] Wegner, Peter M., and Donald Frederick Adams. ”Verification of the combined load compression (CLC) test method”. No. DOT/FAA/AR-00/26. 2000.

[51] McCormick, Nick, and Jerry Lord. "Digital image correlation." Materials today 13.12 (2010): 52-54.

[52] ASTM D3039 / D3039M-17, Standard Test Method for Tensile Properties of Polymer Matrix Composite Materials, ASTM International, West Conshohocken, PA, 2017, www.astm.org

[53] Klaas Allaer “Digital image correlation - Strain measurement beyond colors” Course slides

[54] Tekieli, Marcin, et al. "Application of Digital Image Correlation to composite reinforcements testing." Composite Structures 160 (2017): 670-688

[55] Sutton, Michael A., Jean Jose Orteu, and Hubert Schreier. Image correlation for shape, motion and deformation measurements: basic concepts, theory and applications. Springer Science & Business Media, 2009.

[56] Fiedler, B., et al. "Failure behavior of an epoxy matrix under different kinds of static loading." Composites Science and Technology 61.11 (2001): 1615-1624.